



**University Library**

Author/Filing Title ..... STEINKE .....

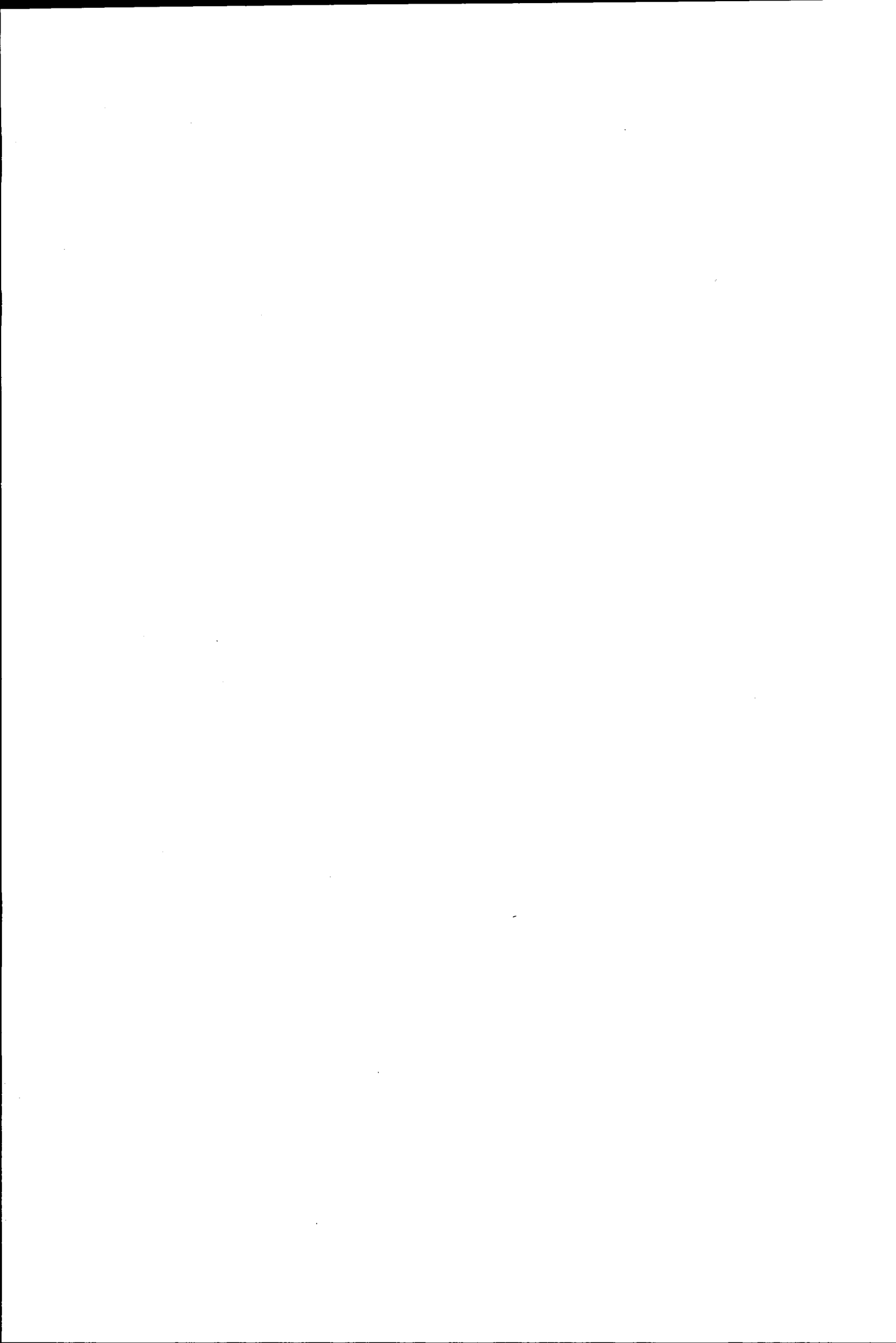
Class Mark ..... T .....

**Please note that fines are charged on ALL  
overdue items.**

--	--	--

040294092X





# Investigation of the structural and magnetic properties of $\text{Fe}_7\text{Pd}_3$

Nina-Juliane Steinke

A Master's thesis submitted in partial fulfilment of  
the requirements for the award of  
**Master of Philosophy of Loughborough University**

October 2004

©Nina-Juliane Steinke

 Loughborough University Bibliographic Unit	
Date	SEP'05
Class	T
Acc no	40294092

## Acknowledgements

I wish to thank my supervisor Klaus Neumann for the support and advice he gave me. Many thanks to Brian Dennis for his great support. Special thanks also to Maureen McKenzie because she is an angel and knows everything about paperwork.

I enjoyed my stay in Grenoble very much and I am grateful to the ILL for the possibilities they offered me. I wish to thank especially P. J. Brown and K. R. A. Ziebeck for their great support with the experiments carried out there and the many fruitful discussions I had with them. They made a lasting impression on me.

I am grateful to the Friedrich-Naumann-Stiftung in Germany who gave me financial and mental support and did whatever they could to make my stay in England possible.

I want to thank especially Jörg Röseler who is a close friend and my tutor in the Friedrich-Naumann-Stiftung. Without him this work would not have been successful and he taught me never to give up. I dedicate this thesis to him and my parents.

I am very grateful to my parents Olaf and Gabriele Steinke, my sisters Franzi and Tina and my brother Nils. Without their neverending support and patience I could not do what I am doing and they are the best family I ever had.

I also want to thank Mrs. Becker very much. She gave me financial support and made it possible that I could spend the last year in England.

I want to thank Toli for everything he did for me.

Many thanks to Kristin Fröhlich, Tamsin Stephens, Ozan Univerdi, Julia Rasch, Stefan Becker, Lutz Heyne and Stefan Hansel for moral support and the good time we had. Special thanks to Tamsin and Julia. I'll never forget the nights in the reactor. Cheers to Gaz and many special thanks to Austin for everything.

Finally I want to thank Klaus Neumann for two beautiful wine glasses.

# Contents

<b>1</b>	<b>Introduction</b>	<b>1</b>
<b>2</b>	<b>Properties of Fe<sub>7</sub>Pd<sub>3</sub></b>	<b>3</b>
2.0.1	Structural Properties . . . . .	3
2.0.2	Magnetic Properties . . . . .	8
<b>3</b>	<b>Sample Preparation</b>	<b>12</b>
3.1	Alloy Preparation Using an Arc Melting Device . . . . .	12
3.2	Heat Treatment . . . . .	15
3.3	X-Ray Diffraction . . . . .	15
3.4	Resistivity . . . . .	16
3.5	Magnetic Measurements . . . . .	16
3.6	Single Crystals . . . . .	17
<b>4</b>	<b>Resistivity Measurements</b>	<b>18</b>
4.1	Introduction . . . . .	18
4.2	Theoretical Background . . . . .	19
4.2.1	Ohms Law and Electrical Resistivity . . . . .	19
4.2.2	Theory of Electrical Resistance of Metals . . . . .	20
4.3	Experimental procedure . . . . .	24
4.3.1	Introduction . . . . .	24
4.3.2	Experimental setup . . . . .	25

<i>CONTENTS</i>	2
4.4 Results and Analysis . . . . .	25
<b>5 Magnetisation Experiments</b>	<b>34</b>
5.1 Introduction . . . . .	34
5.2 Theoretical Background . . . . .	34
5.2.1 Localised Ferromagnetism, Weiss Mean Field Theory . . .	35
5.2.2 Collective Electron Theory . . . . .	37
5.2.3 Applying a Magnetic Field, Anisotropy . . . . .	38
5.2.4 Arrott Plots . . . . .	39
5.3 The SQUID device . . . . .	40
5.4 Results and Analysis . . . . .	42
<b>6 Neutron Diffraction Experiments</b>	<b>53</b>
6.1 Introduction . . . . .	53
6.2 Theoretical Background . . . . .	54
6.2.1 Neutron Cross Section . . . . .	54
6.2.2 Elastic Coherent Scattering . . . . .	56
6.2.3 Coherent Elastic Magnetic Scattering . . . . .	58
6.3 Laue diffraction method . . . . .	62
6.3.1 Introduction and Background . . . . .	62
6.3.2 Experimental Procedure and Results . . . . .	64
6.3.3 Discussion . . . . .	68
6.4 Hot Neutron Four-Circle Diffractometer Measurements . . . . .	69
6.4.1 The Hot Neutron Four-Circle Diffractometer D9 . . . . .	69
6.4.2 Results and Analysis . . . . .	70
6.5 The Spin Polarised Hot Neutron Beam Facility D3 . . . . .	72
6.5.1 Results and Analysis . . . . .	76
<b>7 X-ray Diffraction Measurements</b>	<b>81</b>
7.1 Introduction . . . . .	81

<i>CONTENTS</i>	3
7.2 Theoretical Background . . . . .	82
7.2.1 Laue-equation . . . . .	82
7.2.2 Structure Factors for Bragg-reflections . . . . .	84
7.2.3 Spacing Formula . . . . .	86
7.3 Experimental Procedure . . . . .	87
7.3.1 The Powder Diffractometer . . . . .	87
7.3.2 Indexing the diffraction patterns . . . . .	89
7.4 Results and Analysis . . . . .	89
<b>8 Discussion</b>	<b>95</b>

## Abstract

Investigations of the structural and magnetic properties of  $\text{Fe}_7\text{Pd}_3$  were carried out employing resistivity, powder X-ray diffraction and SQUID magnetometer measurements using a polycrystalline sample. The f.c.c.  $\rightarrow$  f.c.t. transition was observed in the resistivity measurements and its structure was confirmed using powder X-ray diffraction. Heat treatment proved to be necessary to observe the f.c.c.  $\rightarrow$  f.c.t. phase transition. Magnetisation versus temperature measurements were carried out with a low applied field and an unusual temperature dependence was observed. Isothermal measurements of the magnetisation versus applied field at different temperatures were observed and the magnetic moment was determined for temperatures below and above the phase transition. The Curie temperature was determined.

Additionally, neutron diffraction experiments using a single crystalline sample were carried out. Laue diffraction experiments were used to orientate the single crystalline samples and check their quality. Single crystal diffraction was employed to investigate the structural phase transition and polarised neutron diffraction experiments were carried out to investigate the magnetic structure factor of  $\text{Fe}_7\text{Pd}_3$ . However, the single crystal sample did not exhibit a phase transition and the investigations were therefore limited to the high temperature phase.

**Keywords:**  $\text{Fe}_7\text{Pd}_3$ , ferromagnetic shape memory effect, heat treatment, magnetic properties, Laue diffraction, polarised neutron diffraction

# Chapter 1

## Introduction

$\text{Fe}_7\text{Pd}_3$  was found to exhibit a two way shape memory effect at a temperature close to room temperature. An f.c.c.  $\rightarrow$  f.c.t. phase transition was associated with this behaviour. Further investigations during the 1980'ies and early 1990'ies showed that this alloy exhibits some unusual properties such as Invar behaviour over a wide temperature range and a large magnetostriction. Although many investigations were carried out, the results are somewhat confusing and partly contradictory. Especially the relationship between magnetic properties of the ferromagnetic alloy and the observed phase transition are not well understood. Some suggestions to explain the mechanism of the phase transition were made but are not entirely satisfactory. A particular difficulty for investigations of this alloy is the strong concentration dependence of the transition temperature. In addition, the properties of the alloy also depend strongly on the heat treatment.

In recent years the  $\text{Fe}_7\text{Pd}_3$  alloy was found to exhibit a ferromagnetic shape memory effect similar to  $\text{Ni}_2\text{MnGa}$ . In contrast to this alloy,  $\text{Fe}_7\text{Pd}_3$  exhibits a disordered f.c.c. structure while  $\text{Ni}_2\text{MnGa}$  crystallises in the Heusler structure. On the one hand, the ferromagnetic shape memory effect makes these alloys interesting for industrial applications such as small attenuators or solenoids which could react to an applied field. On the other hand, a better knowledge of the

properties of  $\text{Fe}_7\text{Pd}_3$  and their relation to the (ferromagnetic) shape memory effect could help to better understand the mechanism of the phase transition and the ferromagnetic shape memory effect itself. Thus, the aim of this thesis is to investigate some of the structural properties and to determine the magnetic characteristics of the sample in more detail, in particular close to the transition temperature. For this thesis a polycrystalline sample of  $\text{Fe}_7\text{Pd}_3$  was prepared and the influence of heat treatment was evaluated. The f.c.c.  $\rightarrow$  f.c.t. phase transition was studied by means of resistivity measurements and the structural details were confirmed using powder X-ray diffraction. Magnetic properties of the alloy were studied using a SQUID magnetometer. Single crystals were then heat treated in the same manner as the polycrystalline material. These crystals were oriented using Laue diffraction and single crystal neutron diffraction experiments were carried out to examine the phase transition. Additionally, polarised neutron diffraction experiments were made to investigate the magnetic structure factor and its possible variation due to the structural phase transition. However, the single crystalline samples did not transform to the f.c.t. structure. Therefore the investigations made were limited to the high temperature f.c.c. phase.

# Chapter 2

## Properties of $\text{Fe}_7\text{Pd}_3$

### 2.0.1 Structural Properties

F.c.c based alloys exhibiting thermoelastic martensitic transformations have been subject to many investigations over the last 25 years.

Iron-palladium exhibits several martensitic transitions at certain concentration ranges. This thesis focuses on iron-palladium with a concentration range close to 30% palladium atomic concentration, i.e.  $\text{Fe}_7\text{Pd}_3$ . The structure of this alloy depends on its history. In this thesis the high-temperature phase ( $\gamma$ -Fe, Pd) is investigated.  $\gamma$ -Fe has an  $\text{Fm}\bar{3}\text{m}$  structure and lattice parameter  $a=3.6468\text{\AA}$  and palladium has an  $\text{Fm}\bar{3}\text{m}$  structure with lattice parameter  $a=3.8907\text{\AA}$  [1]. To obtain this disordered  $\gamma$  phase the sample has to be heat treated at a sufficient high temperature and then quenched rapidly to avoid separation into the ( $\alpha$ -Fe, Pd) and the ordered FePd phases which are formed at lower temperatures (see phase diagram fig 2.1). The phase diagram fig. 2.1 also shows that the minimum temperature for successful heat treatment is  $>780^\circ\text{C}$ .

The f.c.c. structured Fe-Pd alloy with a palladium concentration of about 30% undergoes several phase transitions, dependent on the exact palladium concentration. Investigations concerning this phase transitions were carried out mainly by two groups Oshima et al. and Matsui et al.. Oshima et al. investigated the

concentration dependence on the phase transition and the  $M_T$  temperature employing X-ray powder diffraction, optical and electron microscopy and published their results in several papers [3] [5] [6] [8] (see table 2.1 and fig. 2.2). It was found that the austenite f.c.c. phase transforms to martensite f.c.t. with a transition temperature just below room temperature for an alloy with a palladium concentration close to 30%. The alloy then transforms further to b.c.t. at lower temperatures. The  $M_s$  temperature of both phase transitions is very strongly dependent on the palladium concentration, the f.c.t.  $M_s$  temperature decreases about 10K if the palladium concentration is increased by 0.1%. The f.c.t. martensite transformation was found in alloys with a palladium concentration range of 29.5% - 33%. Further investigations concerning properties of  $\text{Fe}_7\text{Pd}_3$  and their influence on the martensite transition were carried out by this group and will be mentioned later on.

Additional investigations concerning the phase transition were carried out for instance by Foos et al. [11] using X-ray powder diffraction and electron microscopy, with their results matching with the one's of Oshima et al. . Matsui et al. also did some investigations in [12], however, their results differ from the others as they did not find a transformation from f.c.t. to b.c.t. in the appropriate concentration range, although the samples were cooled down to 4.2K.

However, the results regarding the transition temperature at certain concentrations differ in the various publications which is probably due to the strong concentration dependence of the transition temperature and different methods to determine it.

The relationship between phase transition and palladium concentration is summarised in table 2.1. The relationship between phase transition,  $M_s$  temperature and concentration of palladium is described in fig. 2.2 [6].

Foos, Matsui et al. and Oshima et al. determined also the lattice parameters of the different structures, their results are summarised in table 2.2. All publica-

Table 2.1: Transitions of f.c.c.  $\text{Fe}_7\text{Pd}_3$  over a concentration range from 25% to 32% Pd (atomic percent)

$\text{Fe}_{1-x}\text{Pd}_x$	Transformation type	Reversibility
$x < 0.25$	f.c.c. $\rightarrow$ b.c.c	non-thermoelastic
$0.27 < x < 0.295$	f.c.c. $\rightarrow$ b.c.t.	non-thermoelastic
$0.295 < x < 0.33$	f.c.c. $\rightarrow$ f.c.t.	essentially thermoelastic
$0.295 < x < 0.30$	f.c.t. $\rightarrow$ b.c.t.	non-thermoelastic

The table gives an overview over the different martensite transitions  $\text{Fe}_7\text{Pd}_3$  undergoes in the temperature range from 25%-33% atomic percent palladium and their reversibility. It is noticeable that the f.c.c.  $\rightarrow$  f.c.t. transition differs from the other transitions since it is the only one which is basically thermoelastic. The data were collected by M. Sugiyama, R. Oshima et al. [6] and [5]. The value of 33% was taken from Matsui et al. [12]. Oshima et al. assume that the concentration range of the f.c.c.  $\rightarrow$  f.c.t. transformation ends at 32% atomic percent palladium.

tions agree that the degree of tetragonality in the f.c.t. structure develops with decreasing temperature and the lattice parameter of the f.c.t. structure depends therefore strongly on the temperature. The  $\text{Fe}_7\text{Pd}_3$  alloy exhibits a disordered structure in the f.c.c. phase as well as in the f.c.t. phase. James et al. tried to induce an ordered  $L1_2$  structure as it is observed in  $\text{Fe}_{75}\text{Pt}_{25}$  and  $\text{Fe}_{50}\text{-Pd}_{50}$  by alloying, but they have not been successful so far [24] [25].

The f.c.c.  $\rightarrow$  f.c.t. transition is found to be weakly first order, because both phases exist over a wide temperature range and the f.c.t. phase seemed to appear discontinuously [3][26]. On the other hand it exhibits certain second order like properties such as increasing tetragonality with decreasing temperature, just a small volume change of the unit cell at phase transition and only a very small temperature hysteresis [7]. Thus it is often regarded close to a second order phase transition[6] [8][12].

An important physical property of Fe-Pd alloys with a palladium concentration close to 30% is their invar behaviour. This means that the lattice parameter

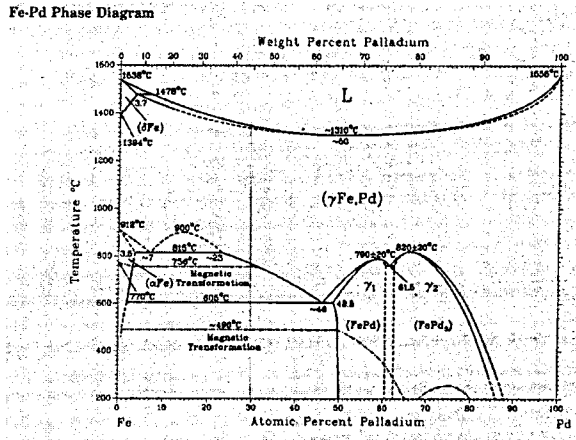


Figure 2.1: Phase diagram of Fe-Pd showing the different phases of Fe-Pd over temperature and palladium concentration in atomic percent. The phase of interest is the high temperature  $(\gamma\text{-Fe, Pd})$  one. The phase diagram was published in [2].

remains constant over a wide range of temperature in contrast to the usual thermal expansion. The invar effect was investigated by Kussman and Jessen [16] and Foos et al. [11] and the lattice parameter of the austenite f.c.c. structure was found to be constant over a temperature range from the Curie temperature ( $\sim 600$  K) down to the martensitic transformation temperature ( $\sim 280$  K). The Invar behaviour manifests itself in a decrease of Young's modulus from the Curie-temperature with a minimum around the transition temperature as found by Nakayama et al. [18] and Oshima et al. [7]. Nakayama et al. did also some investigations of the longitudinal linear magnetostriction of the austenite phase of  $\text{Fe}_7\text{Pd}_3$  [17]. A large magnetostriction was also found by Kubota et al. [19]. In [13] it is stated that the lattice parameter of the austenite f.c.c. phase does not decrease around the invar concentration of 30% Pd as it happens with other Invar alloys such as Fe-Ni and Fe-Pt.

Ohsima et al. [4] [8] and Kato et al. [28] studied extensively the arrangement of variants in the martensite phase and observed that the martensite phase arranges in twinned plates with a common 110 interface at a later stage of the transition. Superstructures were also investigated.

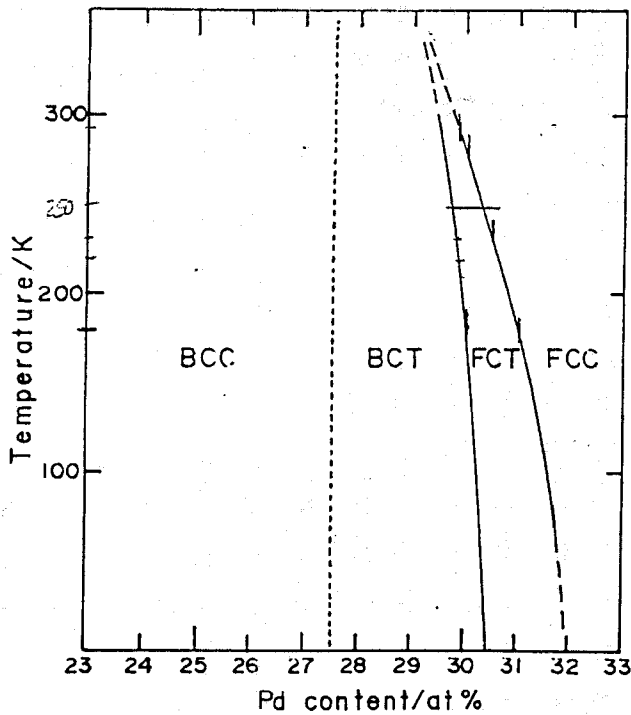


Figure 2.2: This diagram shows the phase transition temperatures versus palladium concentration for the high temperature phase ( $\gamma$ -Fe, Pd) over a range from 23%-33% atomic percent palladium. The Diagram was published in [6] by R. Oshima et al. (1984).

It was found by Oshima et al. [10] that the f.c.c.  $\rightarrow$  f.c.t. phase transition is accompanied by a strong decrease of the  $(C_{11}-C_{12})/2$  elastic constant.

Sato et al. [20] found, that this softening was connected with a phonon softening and broadening of the  $[\zeta\zeta 0]TA_1$  phonon branch and additionally with a broadening of magnons. The softening of the elastic constant has a similar behaviour as the square of the magnetisation  $M^2(T)$  with temperature.

The **shape memory effect** was found in  $\text{Fe}_7\text{Pd}_3$  by Oshima et al. [3]. Vokoun et al. [21] [22] investigated the shape memory behaviour of  $\text{Fe}_7\text{Pd}_3$  and found that a two way shape memory effect can be induced and that a shape memory behaviour is only exhibited when the amount of the b.c.t. phase is kept small.

Table 2.2: Lattice parameters of the different structures of the high temperature phase of  $\text{Fe}_7\text{Pd}_3$ 

Structure	Lattice parameter		$\frac{c}{a}$	Temperature [K]	Pd Conc.	
	a [Å]	c [Å]			%	
f.c.c.	3.750			298	29.7%	[4]
f.c.c.	3.755			273	30.0%	[4]
f.c.t.	3.786	3.690	0.975	273	30.0%	[4]
f.c.t.	3.77	3.69	0.979		30.0%	[12]
f.c.t.	3.860	3.636	0.942	193	29.7%	[4]
b.c.t.	2.96	3.00	1.014	183	29.7%	[4]
b.c.t.	2.942	2.998	1.019			[6]
b.c.t.	2.947	3.021	1.025			[11]

The degree of tetragonality is very small close to the martensitic transition temperature (row 2 and 3  $M_s \sim 273\text{K}$ ). It develops with decreasing temperature (row 5  $M_s \sim 193\text{K}$ ).

## 2.0.2 Magnetic Properties

The first studies on the magnetic properties of  $\text{Fe}_7\text{Pd}_3$  were made by Kussman and Jessen in [16]. They determined that  $\text{Fe}_7\text{Pd}_3$  remains ferromagnetic over the austenite and martensite phase and has a Curie temperature of 570 K. The field necessary to reach saturation magnetisation was found to be 1.6 T.

Matsui et al. [13] measured magnetisation curves of polycrystalline samples at 4.2K. The saturation moment was determined from the magnetisation above the saturation field ( $H > 10\text{kOe}$ ). Thus the magnetic moment per atom  $\bar{\mu}$  at 0K was determined to be  $\bar{\mu} = 2.1\mu_B/\text{atom}$ . The Curie temperature was estimated to be around 600K for a  $\text{Fe}_7\text{Pd}_3$ -alloy. Subsequently, thermomagnetic and inverse susceptibility curves of a  $\text{Fe}_7\text{Pd}_3$ -alloy were measured. The inverse susceptibility increases linearly with increasing temperature and the effective magnetic moment can be estimated from the inverse susceptibility curve to be  $4.54\mu_B/\text{atom}$ .

Oshima et al. [9] investigated the domain wall structure of an  $\text{Fe}_{70.6}\text{-Pd}_{29.4}\%$  alloy. Their results showed that domain walls separating  $90^\circ$  rotated magnetisation occurred between different f.c.t. variants and walls separating  $180^\circ$  rotation across a single f.c.t. variant. Further, they found the easy axis of magnetisation to be the [001] direction. This direction coincides with the axis along which the unit cell contracts. The easy magnetisation direction for the austenite f.c.c. phase was found to be along the  $\langle 111 \rangle$  directions. They mentioned also that their results match those of Matsui [14] who also found that the value of the uniaxial magnetic constant  $K_{u_1}$  abruptly decreased to zero during the austenite-martensite transition and that further the cubic anisotropy constant,  $K_1$ , was negative. This implies that an easy axis of magnetisation is oriented parallel to  $\langle 111 \rangle$ . Oshima stated also that the  $M_T$  temperature was not influenced by the magnetic field within the experimental error. No phase transition could be induced by applying a magnetic field to the austenite sample.

In 1998 James established that  $\text{Fe}_7\text{Pd}_3$  exhibits a ferromagnetic shape memory effect. In case of ferromagnetic shape memory alloys an applied field can rearrange the martensitic variants. Variants with the spontaneous magnetisation in field direction will grow on cost of the others. However, this requires a large magnetic anisotropy and a high mobility of the interface between crystallographic variants so that the spontaneous magnetisation axis coincides with the easy magnetisation axis. Rearranging the variants is more favourable than changing the magnetisation direction within a variant. It was also found by James et al. [24] that a large applied field could shift the martensitic transition temperature and thus induce a structural phase transition. However, the applied field has to be very large, James et al. reported a temperature shift of 20 K for an applied field of 10 T [24].

James, Cui et al. [23] [26] did extensive studies of the magnetic anisotropy in the austenite and martensitic phases by means of vibrating sample magnetometry studies on single crystals under applied stress. They identified the easy

Table 2.3: Magnetic anisotropy constants for the austenite and martensite phase of  $\text{Fe}_7\text{Pd}_3$ 

	$K_0$ [ $\cdot 10^5 \text{erg/cm}^3$ ]	$K_1$ [ $\cdot 10^3 \text{erg/cm}^3$ ]	$K_2$ [ $\cdot 10^4 \text{erg/cm}^3$ ]	T
cubic	3.94	-46	-4.7	295K
	$K_0$ [ $\cdot 10^5 \text{erg/cm}^3$ ]	$K_1 + K_2$ [ $\cdot 10^5 \text{erg/cm}^3$ ]	$K_3/4$ $\cdot 10^5 \text{erg/cm}^3$	
tetragonal	9.10	-0.14	1.82	293K

Anisotropy constant for cubic and tetragonal phase of  $\text{Fe}_7\text{Pd}_3$  as investigated by Cui et al. in [26]. The  $K_1$  constant for the austenite is negative indicating that the easy magnetisation axis is a  $[111]$  direction. The austenite is found to be only weakly anisotropic.  $K_1$  and  $K_2$  are not separable by the employed measurement in the tetragonal phase, and the magnetic energy of a cubic lattice is not dependent of an anisotropy constant  $K_3$ .

magnetisation axes of the tetragonal structure to be the  $[100]$  and  $[010]$ . They contradict here the results of Oshima et al. in [9] and of Matsui et al. [14] [15] who both found that the easy magnetisation axis coincides with the contraction axis in the tetragonal phase. However they agree on the easy magnetisation direction for the austenite phase being the  $\langle 111 \rangle$  directions. The cubic phase exhibits only little magnetic anisotropy. James et al. did further some structural calculations using a Korringa-Kohn-Rostoker approach and showed that these calculations predict the contraction axis to be the magnetic easy axis in the tetragonal phase [24].

Cui et al. [26] also investigated the anisotropy constants of the cubic and tetragonal phase by means of measuring the area under an M-H curve  $W_{hkl}$ . The difference in  $W_{hkl}$  for different crystallographic directions is equal to the difference of the magnetic energy stored in the magnetic material dependent on the magnetisation direction. This energy can be expressed in terms of the anisotropy constants. Their results are summarised in table 2.3. The Curie temperature was determined to be 720K which is about 120K higher than the

one estimated by Matsui [13] as mentioned above.

The saturation magnetisation was found to be  $\sim 145\text{J}/(\text{T kg})$  at room temperature by Nakayama et al. in [17] and  $\sim 160\text{J}/(\text{T kg})$  by Vokoun et al. [21].

Studies on the rearrangement of the martensite variants in an applied magnetic field were carried out by Sakamoto et al. in [27]. They came to the conclusion, that rearrangement occurs if the magnetic anisotropy energy is smaller than the energy required for rearrangement of variants and that the a-axes are the magnetic easy axis in the martensite phase.

# Chapter 3

## Sample Preparation

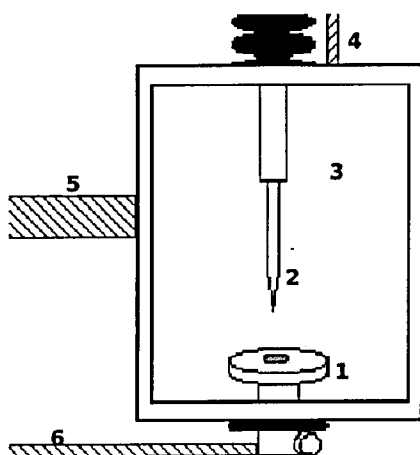
### 3.1 Alloy Preparation Using an Arc Melting Device

The Fe<sub>7</sub>Pd<sub>3</sub>-sample was prepared using electrolytic iron wire of 99.99% purity and palladium wire with a purity of 99.95%. The required amount of metallic ingot to get the chemical composition of Fe<sub>7</sub>Pd<sub>3</sub> could be estimated via the atomic weight of the metals.

$$m_{sample} = x(7M_{Fe} + 3M_{Pd}) = m_{Fe} + m_{Pd} \quad (3.1)$$

where  $m$  is the weight of the specified substance,  $M$  is the molecular mass of the specified substance and  $x$  is a scaling factor.

The ingot wires were cut and weighed. Then the wire pieces were placed on a copper holder. During the process the copper holder was kept cool with a pipe water cooling system which is fixed on the sample holder. In the next step the copper holder was placed in the airtight melting chamber. The chamber was then evacuated and flushed with argon for ten times. Finally argon was led into the chamber to produce an argon atmosphere. It was necessary to remove the air from the chamber because the hot sample ingot would easily react with the oxygen in the air.



1. copper sample holder,  
water cooled
2. Arc
3. vacuum furnace cham-  
ber, argon atmosphere
4. cooling tubes
5. evacuation tubes
6. cooling tubes

Figure 3.1: Schematic drawing of the arc melting chamber

It was possible to see the inside of the melting chamber through a window over which a blackened plate could be fixed in order to protect the eyes while melting. The water cooling system was then switched on. It protects the arc from over heating and the sample holder from heating and melting into the sample. A safety switch permits to switch on the arc melting device only when the cooling system is running.

To check the purity of the atmosphere in the chamber a titanium ball was placed on the sample holder in a separate indent and melted first. If the titanium reacts with some impurities in the chamber the ball will go dark and dull. So the melting of the titanium ball shows if the atmosphere in the chamber is sufficiently clean for preparing the sample.

This being the case, the ingot then got melted using the arc which can be moved up and down and in a small radius by moving the tube coming out on top of the chamber. The arc was placed with some distance over the sample and then switched on with a relatively low starting current of 12A. It was then

moved towards the sample until a light bow bursted out. The ingot then got melted moving the arc over them and increasing the current slowly to 120A. It is absolutely necessary to keep the blackened plate closed over the window during this procedure since the light coming from arc and glowing sample can seriously damage the eyes. The bulk sample was left for cooling until it was solid again and stopped glowing. Employing the arc the sample bulk was then turned over and melted again. The whole procedure was repeated several times to ensure an even distribution of both metals. Finally the metal bulk was left for cooling for several hours in the chamber. The weight loss was then determined comparing the weight of the metallic ingot with the weight of the prepared sample. The weight loss was estimated to be 0.09% for the prepared  $\text{Fe}_7\text{Pd}_3$  sample.

Disadvantages of the arc melt method for preparing an alloy are mainly the danger of getting reactions with unwanted molecules in the atmosphere and heavy weight loss due to metal molecules evaporating into the atmosphere. The first difficulty can be overcome by carefully cleaning and evacuating the chamber and the sample holder. The later problem especially occurs when the metals used have very different and/or low melting points. However, this is not the case for iron and palladium having melting points of  $1535^\circ\text{C}$  and  $1554^\circ\text{C}$  respectively. On the whole, arc melting has been proved a fast and successful method to prepare alloys for scientific investigation and has been therefore widely used for sample preparation [5] [11] [27].

The bulk sample was then cut into appropriate pieces for the different experiments using a spark plug cutter. Hereby the fixed sample got placed into an dielectricum, paraffin in this case. The cutting is done employing a thin wire. A potential of 250V is applied between the sample and the wire. As the wire gets lowered close to the sample, sparks start to jump from the wire to the metal bulk. These sparks are responsible for the cutting process. Due to corrosion the wire has to be replaced by rotating of the wire coil constantly. An advantage of the spark plug method is that minimum stress is applied to the surface and the

structure of the surface is not changed.

## 3.2 Heat Treatment

A part of the cut samples were heat treated. The samples got packed in a metal foil which prevented that quartz of the tube got absorbed into the sample. Then the packet got placed into a quartz tube which was then evacuated and flushed with argon several times. Finally argon with a pressure of 100mbar was let into the quartz tube and the tube was sealed. The pressure was chosen as a compromise between getting the pressure in the tube a close to ambient pressure as possible at the treatment temperature and getting the quartz tube sealed which requires low pressure. The sealed tube then was placed into an heat furnace and left there at 1100°C for 6 days. Afterwards the tube was directly quenched into cold water.

## 3.3 X-Ray Diffraction

For the X-ray measurements a powder specimen was required. An attempt was made to powder the alloy employing a powder box where strong force is applied onto the sample by smashing it with a steel rod. However, the alloy proved to be too ductile and could not be broken by this procedure. In contrast, just a few dents appeared. The same was tried after the metal bulk got heat treated. Powdering was again not possible by means of the above mentioned method.

As no other possibility could be found, the alloy was then finally powdered with a file, which was never used before to avoid contaminating the sample with other elements. The alloy was ductile enough and rather got stuck to the file then breaking pieces out of it. A short X-ray picture showed that the treatment had destroyed the alloy structure so the powder got heat treated again for 5 days at 1100°C as described in section 3.2. Because of the high temperature

sample	length	width	height
Stick 1 – heat treated	18.610 mm	2.090 mm	1.930 mm
Stick 2 – untreated	18.500 mm	2.10 mm	1.760 mm
Stick 3 – heat treated	18.800 mm	2.680 mm	1.760 mm

error of all dimensions  $\Delta s = \pm 0.010$  mm

Table 3.1: Resistivity sample dimensions

required to ensure that the high temperature ( $\gamma$ Fe,Pd) phase is obtained, the material softened during the heat treatment. For this reason the powder grains got stuck together and one piece was obtained after the heat treatment. In order to separate the powder grains again, they were carefully scraped of the bulk material using a metal needle. A powder could be obtained but the grain size was big and a considerable amount of grains were still stuck together. It should be also mentioned that a considerable amount of stress had to be applied to separate the grains after heat treatment.

### 3.4 Resistivity

The samples were sticks with a length of approximately 2cm and a width and height of roughly 1mm (see table 3.1). They were cut out of the sample bulk employing a spark plug cutter. Then two sticks were heat treated while one remained untreated. All sticks were polished afterwards with emery paper to provide better connection with the contact needles and the heating surface of the resistivity measuring device.

### 3.5 Magnetic Measurements

For the magnetic measurements at the SQUID-device a small amount of the heat treated samples was used. The sample was weighed, then placed in a gelatine

sample	weight
single crystal	9.75 mg
polycrystal - powder	2.73 mg

with an error of  $\pm 0.02$ mg

Table 3.2: weight of the SQUID-samples

capsule and fixed to the bottom with cotton wool. The prepared capsule could be easily placed in the measuring device. Gelatine and cotton were chosen as materials for the sample holder because they give no magnetic signal during the measurements. Two specimens were prepared, a single crystal to check the crystal properties after the second heat treatment, and a polycrystal one using some powder (powder preparation see section 3.3).

### 3.6 Single Crystals

For measurements at the four circle neutron diffractometer D9 and the polarised neutron diffractometer D3 both situated at the ILL in Grenoble, France, single crystals were required. A selection of single crystals with the required composition of  $\text{Fe}_7\text{Pd}_3$  was provided for the experiments. The crystal orientation and whether they were really single or not was investigated employing Laue neutron diffraction (see section 6.3). In the next step appropriate crystals were cut out of the crystal bulks and heat treated for 4 days at  $1100^\circ\text{C}$  as described in section 3.2 Heat treatment. After the first set of measurements at the D9 at the ILL the crystals were heat treated again for 11 days at  $1100^\circ\text{C}$  as described in section 3.2.

# Chapter 4

## Resistivity Measurements

### 4.1 Introduction

The ability to conduct electricity is one of the most important characteristics of metals and alloys. This ability is caused by the presence of relatively large numbers of quasi-free electrons which are able to move through a metallic lattice when an electric field is applied. However the resulting conductivity is not infinite but finite<sup>1</sup> due to the presence of diverse, disturbing influences i.e. phonons or spin waves for magnetic components.

These influences disturb the free electron flow, give rise to scattering of electrons and cause a resistance, the electric resistance  $R$  [ $\Omega$ ]. If the sample dimensions are known one can calculate the electrical resistivity  $\rho$  [ $\Omega\text{m}$ ].

The electrical resistivity is the electrical resistance of a conductor normalised to the sample dimensions respectively. It is characteristic for a material and depends on temperature and pressure as well as on the chemical and physical state of that material.

Because of the high sensitivity to the mentioned parameters resistivity measurements can be used to investigate various other properties of a sample and

---

<sup>1</sup>ignoring the low temperature phenomenon of superconductivity

many gauges rely on resistivity measurements (for example electrical-resistance strain gauges, resistance pressure gauges). Another reason for their wide use is the relative ease of the measurements. [30]

In this thesis electrical resistivity measurements will be used to investigate the phase transitions in  $\text{Fe}_7\text{Pd}_3$  samples which differ in heat treatment.

## 4.2 Theoretical Background

### 4.2.1 Ohms Law and Electrical Resistivity

In this section isotropic materials are considered. Ohms law describes the empirical observation that in a given conductor the current density  $\mathbf{J}$  is proportional to an applied electric field  $\mathbf{E}$  for a constant temperature. This can be written as

$$\mathbf{J} = \sigma \cdot \mathbf{E} \quad \text{or} \quad \frac{\mathbf{J}}{\mathbf{E}} = \frac{1}{\rho} \quad (4.1)$$

where  $\rho$  and  $\sigma$  are defined as electrical resistivity and conductivity respectively.

Assuming a conductor of uniform cross-sectional area  $A$  and length  $l$  in which an applied Voltage  $V$  produces a current  $I$ , the electric field and the current density may be expressed by

$$\mathbf{E} = \frac{V}{l} \quad \mathbf{J} = \frac{I}{A} \quad (4.2)$$

Substituting in equation 4.1 leads to the following expression which is equivalent to Ohms law

$$V = I \cdot \frac{\rho \cdot l}{A} = I \cdot R \quad \text{and therefore} \quad \rho = \frac{R \cdot A}{l} \quad (4.3)$$

Equation 4.3 states that current and voltage are proportional in a conductor at a constant temperature, the proportional constant is known as the resistance  $R$  of a sample.[30]

These are the vital equations to measure the electrical resistivity as it is possible to estimate the resistance of a sample by measuring the current for a

well-known voltage (and vice versa) and the resistivity can be easily calculated if the sample dimensions are known.

In case of an anisotropic material the electric field and the current density are not necessarily pointing in the same direction and the resistivity is not necessarily the same for different directions in the sample. Under this circumstances one has to take into account the vector nature of electric field and current density and the electrical resistivity will become a matrix. [30][31]

## 4.2.2 Theory of Electrical Resistance of Metals

### Bloch Theory

Although the principle causes of electrical resistance are well understood, a quantitative approach has been very difficult due to the big amount of involved factors and their varying contributions. However, a fairly good understanding of the principles involved can be gained by making simplifying assumptions:

Conduction electrons do not interact with each other but show coulomb interaction with the ions of the lattice. The ions of the lattice are represented by a periodic potential with the period of the lattice.

It has been found that only electrons in partial filled electron bands contribute to conduction and only one electron can occupy a certain electron state.

To obtain the wave functions for the electron states one has to solve the Schrödinger equation for a periodic potential. It was showed by Bloch that the solutions are plane waves modulated with the lattice periodicity.

$$\Psi_{\mathbf{k}} = u_{\mathbf{k}}(\mathbf{r}) \cdot e^{i\mathbf{k} \cdot \mathbf{r}} \quad u(\mathbf{r}) = u(\mathbf{r} + \mathbf{g}) \quad \mathbf{g} \text{ lattice vector} \quad (4.4)$$

In case of a perfect crystal at zero temperature, i.e. a perfect periodical lattice, the waves would travel through the crystal without any energy loss and no resistance would occur. Two primary sources are responsible for resistance. The first one is temperature dependent phonon-electron interaction, the second is deviations

from periodicity due to chemical or physical imperfections. This second term is independent from temperature. The idea that the resistivity can be written as a sum of a temperature dependent  $\rho_i(T)$  and a temperature independent term  $\rho_0$  is widely known as *Matthiessens rule*

$$\rho_{\text{total}} = \rho_i(T) + \rho_0 \quad (4.5)$$

$\rho_i(T)$  is known as the intrinsic or phonon resistivity,  $\rho_0$  is known as residual resistivity describing the deviations from a perfect crystal.

In case of a ferromagnetic alloy a third term  $\rho_m(T)$  has to be added which describes the scattering effects resulting from spin-disorder. In general it can be said that Matthiessens rule is valid, although strong deviations should be expected for more complicated alloys [31]

If an electric field is applied the conduction electrons will accelerate, yet an equilibrium state is quickly reached due to interactions with the lattice as mentioned above. The steady-state condition may be expressed using the Boltzmann-transport equation

$$\begin{aligned} \left. \frac{\partial f}{\partial t} \right|_{\text{scatt}} &= \frac{df}{dt} \\ \left. \frac{\partial f}{\partial t} \right|_{\text{scatt}} &= \frac{d\mathbf{k}}{dt} \nabla_{\mathbf{k}} f + \frac{d\mathbf{r}}{dt} \nabla_{\mathbf{r}} f \end{aligned} \quad (4.6)$$

where  $f$  is the distribution function of the electrons,  $\left. \frac{\partial f}{\partial t} \right|_{\text{scatt}}$  is the rate at which the distribution changes due to scattering processes and  $\mathbf{k}$  and  $\mathbf{r}$  are the wave and position vectors of the electrons respectively.

Assuming the scattering is essentially elastic a relaxation time  $\tau$  can be introduced as following:

$$\left. \frac{\partial f}{\partial t} \right|_{\text{scatt}} = \frac{f - f_0}{\tau} \quad (4.7)$$

with  $f_0$  and  $f$  as undisturbed and disturbed distribution function respectively. Taking into account the assumptions made concerning the electronic behaviour it becomes clear that  $f_0$  is the Fermi-distribution function. The relaxation time is

inversely related to the collision probability per unit time, so the remaining task is to determine the collision probability. One possibility to do so is to employ the Debye-model which assumes a spherical Fermi-surface in  $\mathbf{k}$ -space. [30]

### Phonon-interactions

Considering conservation of momentum it is found that the difference between initial electron wave vector  $\mathbf{k}$  and scattered wave vector  $\mathbf{k}'$  has to fulfil the following condition:

$$\mathbf{k}' - \mathbf{k} = \pm \mathbf{q} + \mathbf{g} \quad (4.8)$$

where  $\mathbf{g}$  is a reciprocal lattice vector and  $\pm \mathbf{q}$  represents the creation (-) or annihilation (+) of a phonon. If  $\mathbf{g} = 0$  the process simply corresponds to the creation or annihilation of a phonon, if  $\mathbf{q} = 0$  the electrons suffer Bragg-reflection. In case of an Umklapp-process the electrons suffer Bragg-reflection while simultaneously a phonon is destroyed or created ( $\mathbf{g} \neq 0, \mathbf{q} \neq 0$ ) [31]. Phonon scattering is temperature dependent. For instance, the phonon variation is found to be with  $T^3$  at low temperatures. On the other hand the effectiveness of the scattering on the resistivity is dependent on the square of the scattering angle  $T^2/\theta_D^2$  (assuming low angle scattering at low temperatures). So the transition probability for electron-phonon interactions varies with  $T^5$  which gives rise to a phonon contribution to the resistivity  $\sim T^5$  at low temperatures. [30][32]

An approximate approach to describe the phonon contribution to the resistivity was made by Bloch and is today known as the Grüneisen-Bloch equation

$$\rho_i = \frac{C}{\theta_D} \left( \frac{T}{\theta_D} \right)^5 \int_0^{\theta_D/T} \frac{x^5 dx}{(e^x - 1)(1 - e^{-x})} \quad (4.9)$$

with  $\theta_D$  being the Debye temperature and  $C$  a constant. This relation matches the observed data for a wide range of metals very well, although many assumptions like spherical Fermi-surfaces are made and other forms of scattering are completely neglected. These influences do not seem to have a great influence

in many metals. The variation described is by the Grüneisen-Bloch equation is  $\sim T^5$  at low temperatures and  $\sim T$  at high temperatures. [30]

### Impurity Scattering

Impurity scattering arises due to deviations from the perfect crystal. There are physical impurities like point defects, domain boundaries or disorder effects and chemical impurities such as impurity atoms or different isotopes. Resistivity caused by impurity scattering is also called residual resistivity  $\rho_0$ . It is often treated as being temperature independent (see Matthiessens rule), although in more complex cases a temperature dependence can not be neglected. [30] [31]

### Magnetic and Electron-Electron Scattering

The most important type of magnetic scattering is interactions of the spins of the conduction electrons with unpaired spins of the lattice atoms. Below the Curie-temperature the localised or itinerant spins will form an ordered lattice of ferromagnetic or antiferromagnetic order. Like in case of the atomic lattice derivation from the perfect lattice will cause scattering. Electrons possess a spin of  $1/2$  which can exist in just two states 'up' and 'down'. The electrons can therefore interact with the spins of the system, the exchange energy being:

$$E_{exchange} = -J(\mathbf{r})\sigma \cdot \mathbf{S} \quad (4.10)$$

Where  $\sigma$  is the spin of the electron interacting with the spin  $\mathbf{S}$ . The exchange parameter  $J(\mathbf{r})$  is falling off rapidly with  $r$ .

There is elastic and inelastic scattering possible with elastic corresponding to non spin-flip and inelastic to spin-flip scattering respectively. However, the cross section and therefore the scattering probability is dependent on the spin state of the conduction electrons which has to be taken into account. With rising temperature the disorder scattering will increase until the Curie-temperature is reached. Above the Curie temperature the system is in a paramagnetic state

and all spins are statistically distributed. The contribution of spin-interactions to the resistivity therefore remains constant above the Curie temperature if the magnitude of the spins of the sample is temperature independent.

Electron-electron scattering is another possible source for a rise in resistivity. In this case the scattering is due to Coulomb interaction of the electrons.

However, the temperature dependence of these scattering sources is difficult to determine. Various attempts have been made to estimate the temperature dependence of these scattering sources. Electron-electron scattering was found to vary with  $T^2$  according to theoretical considerations, but magnetic scattering varies with a similar temperature dependence. An approach gives a  $T^{1.5} + T^2$  for instance. It should be pointed out, that these calculations were made using low temperature approximations. [30]

## 4.3 Experimental procedure

### 4.3.1 Introduction

The employed four-point method of measuring the electrical resistivity is based on Ohms law (section 4.2.1). The four-point method is widely used for measuring small electrical resistance for instance in commercial resistometers. The basic idea is to send a current through a sample and then to measure the potential difference over the sample. Four contacts with the sample are used: two for the current circuit and two for measuring the difference in potential over the sample.

An important advantage of the four-point method over the two point-method (where current and voltage contacts are the same) is that the error due to contact resistances is minimised. The voltage contacts do normally not transport electrical charges and therefore their resistance contact resistance has no influence on the measurement. The current contacts have a significant electrical resistance but the voltage is not measured over the current contacts so they do not influence

the measurement.

### 4.3.2 Experimental setup

The sample stick was placed into a cryostat on a silicon heating surface which was connected with the temperature controlling device Oxford ITC 503. The cooling of the sample was done by a Displex employing Helium gas and then the temperature was controlled by continuous cooling and regulating the heater. The temperature setting as well as the data recording were carried out by a computer. Contacts between the sample and the circuit were made using needle pins which were pressed on the sample surface by springs to assure a good contact. To measure the resistivity a small, alternating excitation current was sent through the sample. The excitation current needs to be small to ensure that the heat production in the resistor i.e. the sample is very small and the sample temperature remains constant at the set temperature even at low temperature measurements.

To measure the resistivity at a certain temperature first a new set-point for the temperature was set. It was made sure that thermal equilibrium was reached by monitoring the temperature deviations over 5 minutes. Then 40 resistance measurements were carried out and the average value was recorded. The data recording was completely computer controlled.

## 4.4 Results and Analysis

An example of a resistivity versus temperature curve for a heat treated sample is given in fig 4.1. The resistivity rises smoothly until about 278K when a sudden change in the slope of the curve takes place. From about 284K onwards the curve continues to rise smoothly. The change takes place in a relatively small temperature range of 6 K. The whole curve is continuous just the slope has

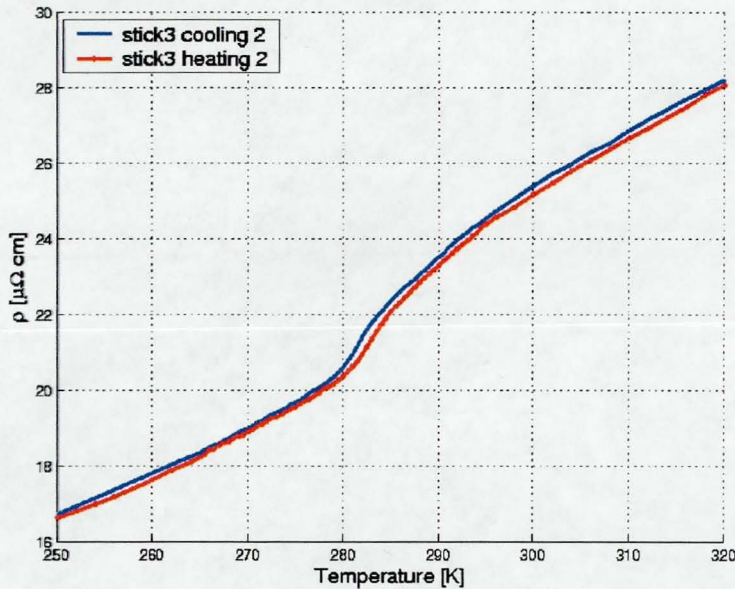


Figure 4.1: Resistivity versus temperature for a cooling measurement and the directly following heating measurement.

a sharp change. This behaviour is clearly different from an untreated sample (fig. 4.5), which shows a smooth curve with no sudden changes in slope. X-ray diffraction measurements (see chapter 7) confirmed, that these change can be ascribed to the f.c.c.  $\rightarrow$  f.c.t. martensitic phase transition.

In fig. 4.1 the blue curve refers to a cooling measurement and the red curve to the following heating measurement. Both curves are very close to each other and have identical shape. Although the heating curve is a bit decreased in order of magnitude compared with the cooling curve. Fig. 4.1 therefore shows that the curves exhibit only a very small temperature hysteresis.

The experiments carried out were very well reproducible, as shown in fig. 4.2. In this figure several cooling cycles are printed. It can be seen that the different curves are very close to each other and are of identical shape. However, the magnitude of the resistivity decreases slightly with each cooling.

The decrease in resistivity from cooling to heating cycle must have at least partly different reasons because the resistivity measured in a cooling cycle was

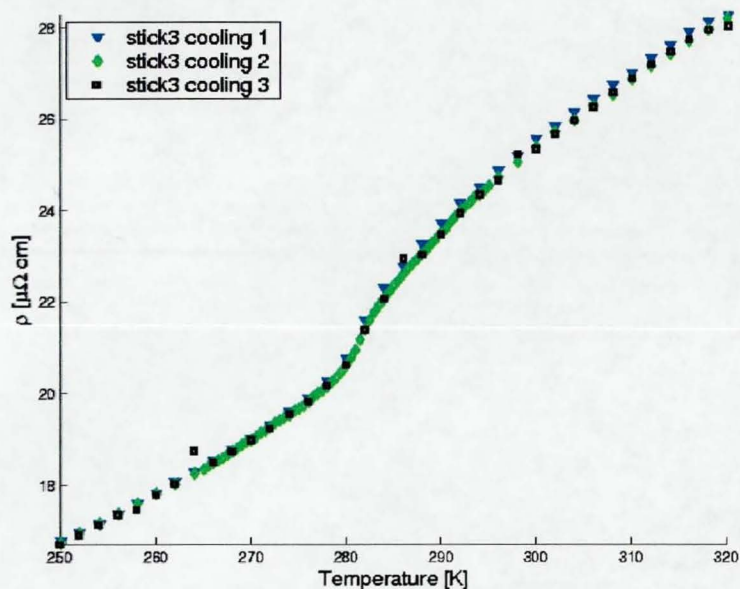


Figure 4.2: Several cooling cycles of the same sample

always larger than in the heating cycle before, although slightly smaller than in the previous cooling cycle. If the decrease in resistivity between heating and cooling and several cooling (or several heating) cycles would have the same reason, it would be expected that the magnitude of the resistivity would change as following: cooling(1) > heating(1) > cooling(2), because the data were recorded in this order. In contrast to this behaviour, the observed order was cooling(1) > cooling (2) > heating(1). The change in magnitude between cooling and heating will therefore be ascribed to hysteresis and the changes between cooling cycles to small, irreversible changes within the sample.

The point of maximum change in the curves was determined as the transition temperature of the phase transition. To determine the associated temperature the derivatives of the curves were examined, which were calculated using  $\frac{d\rho}{dT} = \frac{\rho_j - \rho_i}{T_j - T_i}$ .  $j$  denoting a data point  $(\rho_j, T_j)$  and  $i$  denoting the previous data point. The transition temperature  $M_T$  was therefore determined to be  $(283 \pm 1)K$ , with the results for each measurement summarised in table 4.1. The uncertainty of 1 K

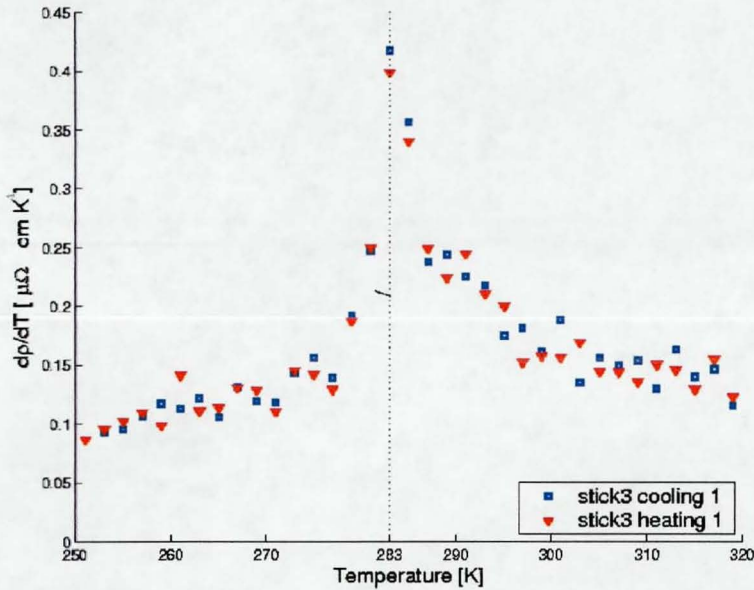


Figure 4.3:  $d\rho/dT$  versus temperature. The derivative was calculated using  $d\rho/dT = (\rho_j - \rho_i)/(T_j - T_i)$ .

results of the resolution of the experiment (the temperature steps were usually 2 K) and the way the derivative was determined. In fact 283K represents the temperature range from 282K to 284K a more precise estimation is not possible with the given resolution. However, all experiments give the same temperature range as result, so it can be assumed that all further errors in the determination of the transition temperature are well below the resolution range and do not need to be considered. Fig. 4.3 shows the derivative curve for a cooling and a heating cycle. A sharp peak around 283 K can clearly be seen. The other derivative curves resemble this behaviour and are not shown for this reason.

If the sample was cooled to lower temperatures, that is below 250K down to 50K, the expected change could not be observed any more. This can be seen in fig. 4.4, which shows a cooling curve down to 50K and the following heating curve. It can be seen that the change takes place in the cooling cycle but not in the following heating cycle. The sample was never cooled down before. All following measurements with this sample did not exhibit the sudden change in

Table 4.1: Transition temperature for each measured cycle

Transition temperature	
c1	$(283 \pm 1)$ K
c2	$(283 \pm 1)$ K
h2	$(283 \pm 1)$ K
c3	$(282.5 \pm 0.5)$ K
h3	$(282.5 \pm 0.5)$ K
c4	$(283 \pm 1)$ K
h4	$(283 \pm 1)$ K

'ci' and 'hi' denote the different heating and cooling cycles respectively. The curve c1 was obtained from a different sample stick than the other curves, but both sticks were obtained from the same bulk and heat treated together (see sample preparation 3.4). For cycle four the temperature step size was changed from 2 K to 0.5 K in the range of the transition, resulting in a different uncertainty of the values. The results indicate very strongly a transition temperature of  $(283 \pm 1)$ K.

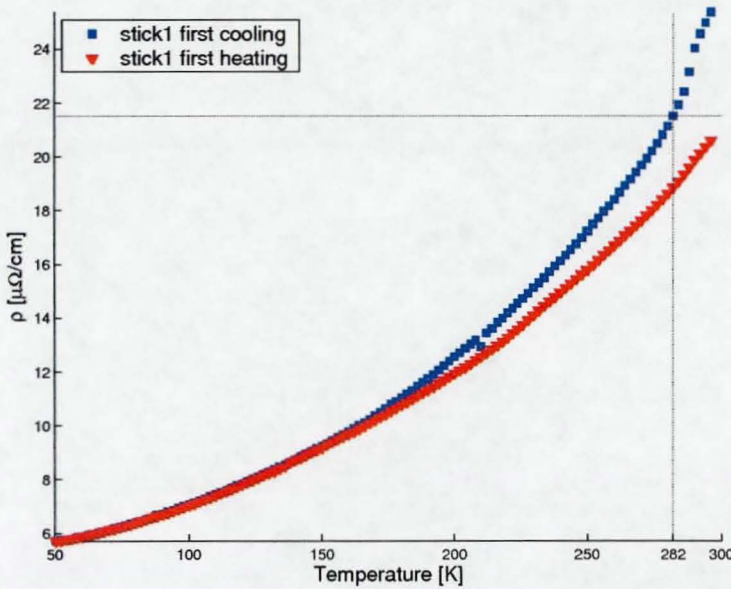


Figure 4.4: The graph shows the first cooling for a sample down to 50K and the following heating curve. The cooling curve exhibit a slope change above 280K, but the heating cycle recorded afterwards does not show this behaviour.

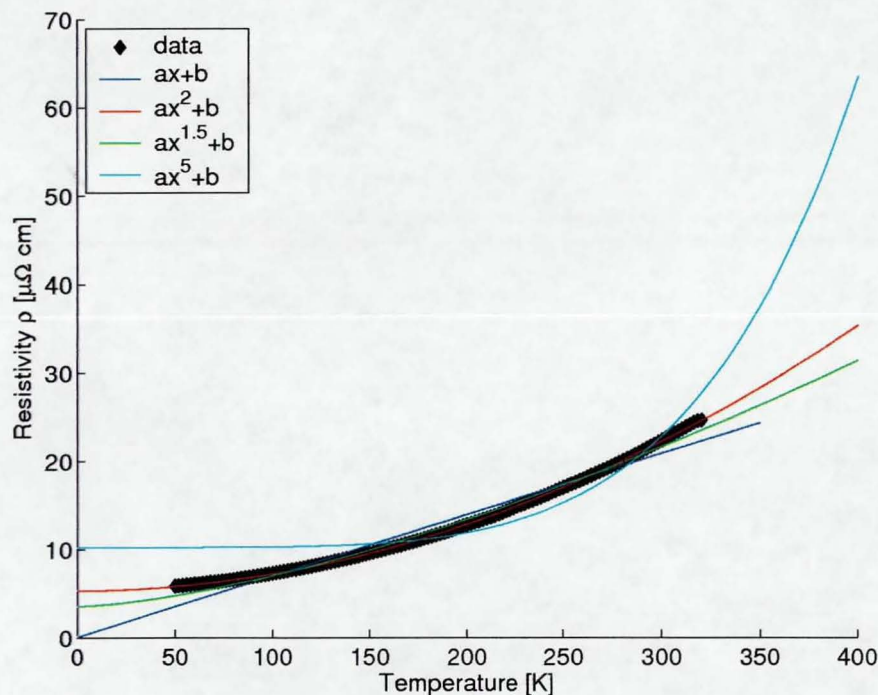


Figure 4.5: Resistivity versus temperature of the untreated sample with various resistivity contributions fitted to the data. The parameters can be found in tab. 4.2

slope. This indicates that at lower temperatures a change takes place in the sample which is not observable in resistivity measurements. This change can be associated with a f.c.t.  $\rightarrow$  b.c.t. transition, which is known to appear at lower temperatures in  $\text{Fe}_7\text{Pd}_3$  (see section 2.0.1). The transformation of the sample is irreversible since the f.c.c.  $\rightarrow$  f.c.t. transition around 283K could not be observed when the sample was heated up again. Instead, the resistivity curve shows a smooth behaviour, similar, but not equal to the one of an untreated sample (fig. 4.5).

Fig. 4.5 shows the resistivity curve of an  $\text{Fe}_7\text{Pd}_3$  sample which was not heat treated. Various attempts were made to fit the curve to a polynomial with respect to the temperature dependence of the different contributions to resistivity, as described in 4.2.2, in order to determine their contribution to the total resistiv-

fit	parameter a	parameter b	$\Delta U$
<b>untreated sample</b>			
$ax + b$	0.06955 (3.4%)	0.06702 (500%)	1.1064
$ax^{1.5} + b$	0.003494 (1.7%)	3.534 (5.3)%	0.5622
$ax^2 + b$	1.883e-4 (0.2%)	5.326 (0.5)%	0.0831
$ax^5 + b$	5.22e-012 (7.8%)	10.21 (4.4)%	2.1301
$ax + bx^2 + cx + d$	a=2.804e-3(0.1%)	b=1.709e-4(0.02%)	
	c=3.6e-013(33%)	d=5.272(0.8%)	0.0279
<b>heat treated sample, with transition, lower temperatures</b>			
$ax + b$	0.1171 (3.5%)	-12.78 (8%)	0.0625
<b>heat treated sample, with transition, higher temperatures</b>			
$ax + b$	0.1452 (1.5%)	-18.43 (4%)	0.0228

Table 4.2: Fit data

Different resistivity contributions fitted to the resistivity data of the untreated sample and the heat treated sample transformed to b.c.t..  $\Delta U$  denotes the standard deviation for the fits and shows the quality of the obtained fits. The percentages next to the fit parameters give 95% confidence bounds. A linear fit was also made to the low and high temperature regions of a curve with a phase transition. The fits match well showing a linear behaviour of these regions, but the values obtained are only valid for the limited temperature regions (260K - 280K and 300 K - 320K respectively) and the curve will clearly show a different behaviour in other temperature ranges.

ity. The fit results are summarised in table 4.2. To fit the data the following assumptions were made in agreement with the considerations in 4.2.2. Phonon contribution will give either a  $\sim T^5$  (for low temperatures) or an  $\sim T$  (for high temperatures) contribution. A  $\sim T$  term can be expected, considering that the temperatures investigated do not belong to a low temperature range. The magnetic contribution was assumed to be  $\sim T^{1.5} + T^2$ . An electron-electron interaction term was taken into account, giving rise to a curve  $\sim T^2$ . Residual or impurity resistivity was assumed to be constant. With these assumptions various polynomial fits were made and the following results were found. Of all single contributions

fitted to the data, the  $\sim T^2$  matches the data best. A quadratic fit alone gives a very good fit to the data obtained, see fig. 4.5. Several polynomial fits were also made to the data and in these fits contributions  $\sim T^2$  had a significance which was about an order of magnitude higher for the observed temperature range. The domination of a  $T^2$  term indicates that magnetic and/or electron-electron scattering give a strong contribution to the observed resistivity (see sec. 4.2.2). The residual resistivity would be around 5, as can be seen from the quadratic fit. All polynomial fits where several terms contributed showed a similar constant. Still an exact estimation of the residual resistivity needs to estimate the resistivity at very low temperatures.

Additionally, an attempt was made to fit the high and low temperature regions of a resistivity curve which exhibited a transition. A linear fit was found to match the data very well, quadratic and higher terms were found to be of little significance. However, these fits are only of limited significance because they include only a very limited temperature range. The constants obtained in these fits do not have a direct physical meaning. The residual resistivity, for instance, will not be negative for the obtained data. Nevertheless this might indicate, that high temperature phonon scattering is dominating the resistivity in these regions.

The measurements showed clearly a difference in the resistivity of untreated and heat treated samples, with the latter exhibiting a phase transition at 283 K. As the chemical composition of both samples is identical, the difference in behaviour can be regarded as a structural difference caused by the heat treatment. The observed phase transition was almost reversible and well reproducible. The transition observed showed only very little temperature hysteresis and took place over a range of about 6 K. Further, the experiments have shown indirectly that a second transition takes place at lower temperatures, which can be associated with an f.c.t.  $\rightarrow$  b.c.t. transition by comparing with the literature (sec. 2.0.1). This transition could not be seen in the resistivity curve, but after cooling to low temperatures the sample did not exhibit the transition around 283 K any

more. This shows further that the b.c.t. transition at low temperatures must be irreversible. Several fits were made to the untreated sample, in order to separate different contributions to the resistivity. It was found that the curve is dominated by a quadratic term. Which leads to the assumption electron-electron or magnetic interactions contribute mainly to the resistivity in the observed range. The high and low temperature region of a curve showing the f.c.c.  $\rightarrow$  f.c.t. transition were found to be essentially linear, which indicates domination of high temperature phonon scattering, but these fits were carried out only over a very limited temperature range.

# Chapter 5

## Magnetisation Experiments

### 5.1 Introduction

$\text{Fe}_7\text{Pd}_3$  is a strongly ferromagnetic sample and its magnetic properties are of high interest. Recently it has been found that  $\text{Fe}_7\text{Pd}_3$  exhibits a ferromagnetic shape memory effect. This behaviour is also known from  $\text{Ni}_2\text{MnGa}$  [29]. In order to get a closer understanding of the magnetic properties of the sample measurements were carried out using a SQUID (Superconducting QUantum Interference Device) magnetometer.

### 5.2 Theoretical Background

It has been found that most atoms possess a permanent magnetic moment which is caused by unpaired spins in the electron shell of the atom and/or by an overall orbital momentum of the electrons in the atomic shells. In a crystal the atomic magnetic moments will interact with each other and form an overall magnetic moment specific for this substance. A ferromagnetic substance will show the following behaviour. If no magnetic field is applied the bulk magnetisation of a ferromagnetic material will be zero. In contrast to paramagnetic substances, this

is not explained by randomly orientated magnetic moments, but by randomly orientated magnetic domains within the material. Within each domain the magnetic moments are aligned. The alignment of the magnetic moments within a domain is not perfect at finite temperatures, yet the magnetic moments will rotate around the overall magnetisation direction in that domain. This effect is due to thermal energy, which increases the entropy and works against the ordering effect of the magnetic moments. If the temperature is raised this thermal effect will increase and the magnetisation within a domain therefore decreases. At a certain temperature the magnetisation within the domain will then reach zero and all magnetic moments are randomly orientated. This temperature is known as the Curie-temperature.

$\text{Fe}_7\text{Pd}_3$  is a ferromagnetic substance consisting of iron and palladium atoms which are both transition elements. In these elements the magnetic moment is associated with the electronic d-shells. [35] [33]

### 5.2.1 Localised Ferromagnetism, Weiss Mean Field Theory

Weiss suggested that in a material with permanent magnetic moments an aligning interaction between these moments takes place. This interaction is described in terms of a molecular field. The resultant field in such a material would then add up to be

$$\mathbf{H}_{\text{tot}} = \mathbf{H}_{\text{ext}} + N_{\text{W}}\mathbf{M}_{\text{T}} \quad (5.1)$$

where  $\mathbf{H}_{\text{tot}}$  is the resulting field in the material,  $\mathbf{H}_{\text{ext}}$  an externally applied field,  $\mathbf{M}_{\text{T}}$  the magnetisation at temperature  $T$  and  $N_{\text{W}}$  is known as the molecular field (or Weiss field) constant. Ferromagnetism can now be explained, if the assumption is made that in a ferromagnet the molecular field introduced by Weiss is much stronger than in a paramagnetic material. This strong molecular field forces the magnetic moments within the material to align themselves even if no external field is present. This can be understood as follows, if a small magnetic field is

field is present. This can be understood as follows, if a small magnetic field is by chance applied to the material the magnetisation will rise to a certain value, according to the theory of paramagnetism. This magnetisation will now induce a Weiss field of a certain value  $N_W M$ , but this Weiss field will in turn rise the magnetisation of the material to a higher value and so forth. The magnetisation of the material will increase to a stable value  $M_s$  which is of course temperature dependent.

It can be concluded that if in a material a sufficiently strong molecular field exists, the material becomes spontaneously magnetised and therefore ferromagnetic, otherwise it would be paramagnetic. The saturation magnetisation measured for a certain temperature, if a high magnetic field is applied, is just the above described stable magnetisation  $M_s$ , however, if no external field is applied the bulk magnetisation of the sample will be zero and the spontaneous magnetisation is rather less obvious. To explain this, Weiss suggested that any ferromagnetic material consisted of different subsections, domains, which are magnetised to the saturation magnetisation  $M_s$ , but the orientation of all these domains is entirely random, so that the resultant bulk magnetisation is zero. A high external field would then rearrange the orientation of the domains so that there is a resulting magnetisation in direction of the external magnetic field.

This process would require a smaller field strength compared to the one needed to introduce a comparable resultant magnetisation in a paramagnetic material, which matches with experimental observations. The domain theory is well established by numerous experiments. Domains are in fact observable under a microscope, such measurements were also carried out for  $\text{Fe}_7\text{Pd}_3$  [9].

The origin of the Weiss field can be explained as follows. It has been shown that a purely magnetic interaction of magnetic dipoles can not explain the Weiss field because the interaction energy is several orders of magnitude too small. Heisenberg first suggested that the Weiss field could be explained in terms of electron exchange interactions. In a hydrogen molecule for instance these forces

lead to a strong coupling of the electron spins which forces them to align themselves antiparallel. The exchange energy of two electrons can be written as:

$$E_{ex} = -2J_{ex}\mathbf{S}_i \cdot \mathbf{S}_j \quad (5.2)$$

with  $J_{ex}$  being the exchange integral. If the exchange integral is negative the energy of the system is minimised if the spins align antiparallel (as in the case of a hydrogen molecule). However, if the exchange integral is positive, a parallel alignment gives the minimum energy, thus giving a quantum mechanical description of the aligning interactions.

A positive exchange integral can indeed be calculated for ferromagnetic metals such as iron, cobalt and nickel. The condition for its occurrence is, that the distance between the nuclei in a material is large compared to the effective mean diameter of the electronic sub shells which carry the magnetic moment. For iron this is the 3d sub shell. [33] [34] [35]

### 5.2.2 Collective Electron Theory

It is found that the magnetic moment per atom in a crystalline substance is in general not equal to a whole number (in units of Bohr magnetons  $\mu_B$ ) as it would be expected, if it is assumed that each atom within the material is a separate entity. The collective electron theory of metals imagines a metal structure consisting of diamagnetic atomic cores and the valence orbitals of the atoms overlapping and forming broad energy bands. A valence electron now does not occupy a narrow energy level on an atomic shell, but it occupies a level in a much broader energy band that belongs to the crystal as a whole. Each energy band can be divided into to sub-bands containing electrons with either spin up or spin down. If no magnetic field is applied these bands are degenerate, which means they have the same energy. When a magnetic field is now applied the degeneracy is removed and the two bands will have different energies. The Weiss

field is a strong magnetic field and will therefore shift the energies of the two sub bands. If the bands are now not completely full but filled to a certain energy level, the number of electrons with positive and negative spin will be different. This difference is responsible for the magnetic moment. In general the magnetic moment will not be an multiple of the Bohr-magneton  $\mu_B$  per atom as it would be expected for free atoms. This can be explained considering that, the 3d and the 4s bands overlap over a wide energy range. Only the 3d bands contribute to the magnetic moment, the density of states in the 4s band is too low to give significant contribution. Due to the overlap of the energy bands electrons with certain energies will occupy levels in the 3d as well as in the 4s bands. The number of electrons per atom in the 3d band will then in general not be a whole number any more. [33] [34]

### 5.2.3 Applying a Magnetic Field, Anisotropy

In a crystal the magnetic moments will be more easily aligned in certain directions compared to any other ones. This behaviour is called magnetic anisotropy and is described by anisotropy constants  $K$ . If no field is applied the magnetic moments of the domain will prefer to align themselves along the easy magnetisation axis. If now a magnetic field is applied the domains with magnetic moments, which are closer aligned to the magnetic field direction, will minimise their energy, compared to those domains with magnetic moments with a larger angle to the field direction. The domains with a favourable alignment of their magnetic moments will grow at the expense of the other domains and a resulting bulk magnetisation can be measured. This process will continue until the whole sample consists of one domain with favourable energy and then the saturation magnetisation of the specimen for a specific temperature is reached.

The energy of a domain is determined by the anisotropy energy favouring the magnetic easy direction for an alignment of magnetic moments and the external

field energy which is minimised if the magnetic moments are aligned parallel to the field direction.

$$E_{tot} = E_{aniso} - MH \quad (5.3)$$

If very strong fields are applied the field energy will be stronger than the anisotropy energy and the magnetic moments will rotate within the domain and align themselves parallel to the field direction.

### 5.2.4 Arrott Plots

Arrott plots give the possibility to obtain the magnetic moment per formula unit and the Curie temperature using magnetisation versus magnetic field measurements. Arrott used the Landau theory of phase transitions to obtain the following description. In the Landau theory the free energy  $F_0$  is described as a power series of the order parameter which is chosen to be the magnetic moment  $M$ . The free energy, normalised to one magnetic atom, can then be written as:

$$\frac{F_0}{N} = \frac{\hat{F}_0}{N} + \frac{1}{2}AM^2 + \frac{1}{4}CM^4 - MB_{ext} \quad (5.4)$$

Minimising the free energy yields to the magnetic moment

$$\frac{\partial \left( \frac{F_0}{N} \right)}{\partial M} = 0 \quad \rightarrow \quad AM + CM^3 - B_{ext} = 0 \quad (5.5)$$

This equation can be rewritten in the following form

$$M^2 = \frac{1}{C} \frac{B_{ext}}{M} - \frac{A}{C} \quad (5.6)$$

The equation represents a linear equation  $y=ax+b$  with  $y = M^2$ ,  $x = \frac{B_{ext}}{M}$  and  $a$  and  $b$   $\frac{1}{C}$  and  $-\frac{A}{C}$  respectively. The intersection with the Y-axis is given by  $-A/C = M^2$  and gives the value of the spontaneous saturation magnetisation at zero field as described above. The Landau theory of phase transition shows that the parameter  $A$  describes the inverse susceptibility and the parameter  $C$

is due to higher order corrections. The parameter  $A$  is taken to be temperature dependent  $A = A(T - T_C)$  and  $< 0$  for the ferromagnetic state.

As the magnetisation of a sample and its magnetic moment per formula unit are related by normalisation factors, the magnetic moment per formula unit and for paramagnetic phases the susceptibility can be determined by means of Arrott plots. For  $T=T_C$  the coefficient  $A$  will become zero and therefore the Arrott plot will pass through the origin, thus also the Curie temperature can be determined. It should be noted that these equations are of approximate character, since the free energy expansion is not exact and high temperature approximations were made. Another assumption made in the analysis was, that the sample may be homogeneous, deviations from this assumption like magnetic domain structures, composition fluctuations or impurities will result in a curvature of the Arrott plots at low fields. To obtain the intersection with the y-axis in this case an interpolation of the linear part of the Arrott curves has to be made. [36]

### 5.3 The SQUID device

The magnetisation measurements were carried out using a SQUID magnetometer built by Quantum Design<sup>TM</sup>. Magnetisation measurements were made as a function of temperature and in fields up to 5.5. T.

A SQUID magnetometer gives the possibility to measure the magnetisation of a sample with the highest possible accuracy. The device is based on a superconducting coil with a small Josephson junction. This is a small gap made of an insulating material in the superconducting ring. The gap has to be small enough to allow the supercurrent to tunnel through the gap. The magnetic flux trapped within a superconducting ring can only change by discrete amounts of a flux quantum. Because of the Josephson junction an external magnetic flux can penetrate the coil and change the flux in there. Thus the flux in the ring is not necessarily a integer multiple of a flux quantum any more. The relationship

between internal and external flux in such a coil can be written as

$$\phi = \phi_{\text{ext}} - LI_c \sin(2\pi\phi/\Delta\phi) \quad (5.7)$$

with  $L$  being the induction coefficient of the superconducting ring and  $I_c$  the critical current determined by the Josephson junction. The sine term occurs because of the phase shift an electron wave functions suffers, when tunnelling through the Josephson junction. This phase shift is related to the flux within the ring. Whenever the flux within the ring becomes equal to a flux quantum  $\Delta\phi = 2.607 \cdot 10^{-15} \text{Wb}$  the flux within the ring will be equal to the external flux and a discontinuity in a  $\phi_{\text{ext}}$  versus  $\phi$  curve occurs. The coil allows to count the magnetic flux in units of the magnetic flux quantum. If a pick-up coil is placed in the vicinity of the detector coil, a voltage pulse will be induced in the pick-up coil each time the flux in the detector coil changes by a flux quantum. The voltage signal can be amplified and detected. To measure the magnetic properties of a sample, a magnetic field is applied to a sample which is placed in the detector coil. The sample is then moved up and down to known positions with a known speed. The movement of the sample will induce an external magnetic flux depending on the sample properties. this flux can be detected by the superconducting detector coil. To get accurate results the sample position must be precisely known and therefore the sample position has to be adjusted carefully before the measurements can be carried out.

The employed SQUID was built by Quantum Design<sup>TM</sup>. It measures in a temperature range from liquid helium temperature up to 355 K. A magnetic field of up to 5.5 T can be applied (direction reversible). The SQUID device is highly automatically controlled using a PC. The control program also contains a validation function which allows to see the sample position relative to the detector coil. An adjustment of the correct zero position can be carried out manually and checked again with the validation function.

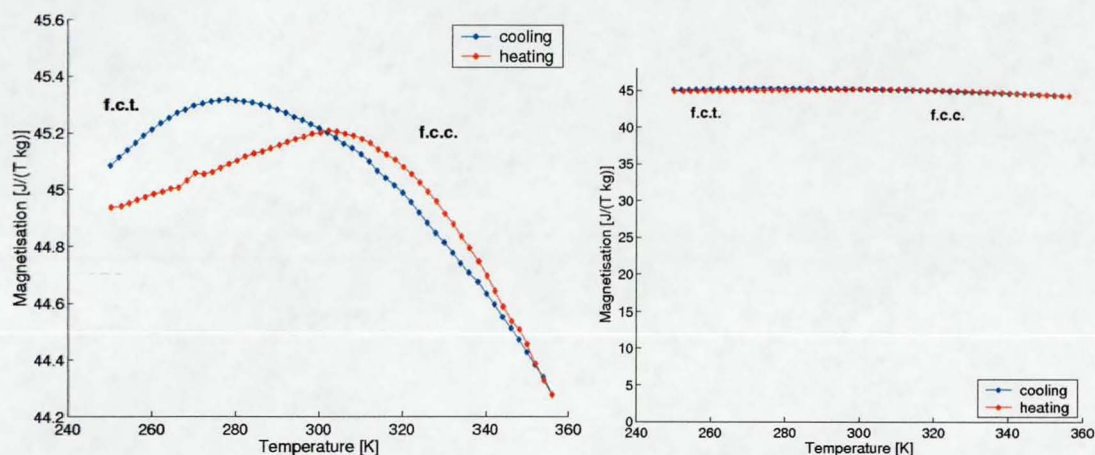


Figure 5.1: Magnetisation versus temperature curve for a polycrystalline  $\text{Fe}_7\text{Pd}_3$  sample. The sample was first heated up from 250 K to 356 K and cooled down afterwards to 250 K again. The step size for the recorded measurements was  $\Delta T = 2$  K. A magnetic field of  $B = 0.1$  T was applied during the measurements.

## 5.4 Results and Analysis

With a polycrystalline sample (in powder form) magnetisation versus temperature measurements were carried out at a low magnetic field of 0.1 T, to see, if the f.c.c.  $\rightarrow$  f.c.t. phase can be detected by a magnetisation measurement. Furthermore, magnetisation versus applied field curves were measured at various temperatures (260 K, 280 K, 290 K, 300 K, 310 K, 340 K, 355 K) to determine the magnetic moment per formula unit at these temperatures. Lower temperatures were not measured because of the irreversible phase transition, which was detected in resistivity measurements and is expected to occur at about 220 K (see fig. 2.2). However, after these measurements were carried out, the sample was cooled down to low temperatures to see, whether a phase change could be detected. Magnetisation versus temperature measurements were also carried out using a single crystalline sample.

Fig. 5.1 shows the magnetisation versus temperature curve for a polycrystalline  $\text{Fe}_7\text{Pd}_3$  sample between 250K and 355K. It can be seen from the curves that the overall change of the magnetisation over the measured temperature range

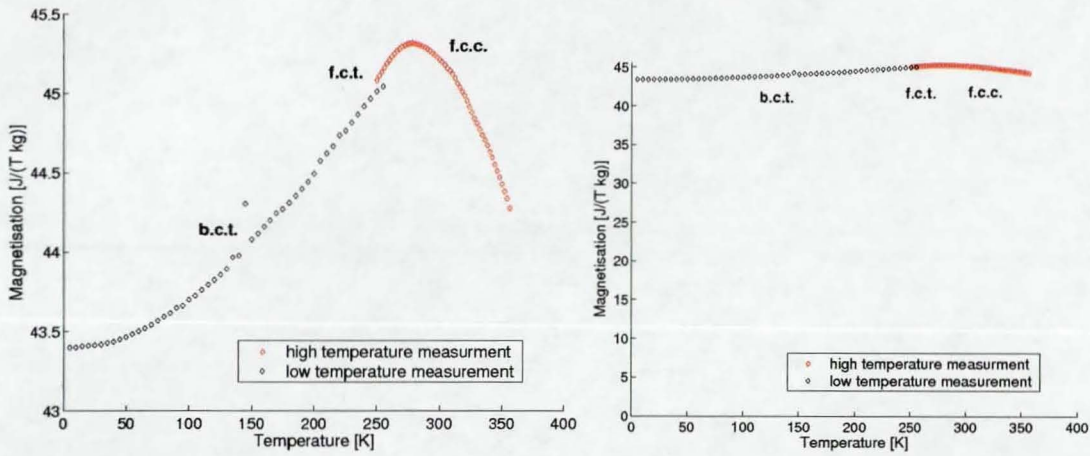


Figure 5.2: Magnetisation versus temperature curve, obtained when the sample was cooled down to low temperatures (5 K), combined with the cooling measurement made at higher temperatures earlier on, to give a view on the magnetisation over a wide temperature range.

is small with  $\Delta M_{max} = 1.041 \text{ J}/(\text{kg T})$ . With increasing temperature the curves rise to a maximum value and then decrease smoothly when the temperature is further increased. This behaviour can indicate a phase transition, since a continuously decreasing magnetisation is expected with increasing temperature. However, the maximum magnetisation occurs at different temperatures, 302 K for heating and 278 K for cooling respectively. The order of magnitude is also different, the heating curve shows a lower magnetisation than the cooling curve (heating:  $M_{max} = 45.209 \text{ J}/(\text{kg T})$ ; cooling:  $M_{max} = 45.319 \text{ J}/(\text{kg T})$ ). This difference amounts to  $\sim 10\%$  of the overall change in the temperature range. In short, the cooling curve is shifted to the left compared to the heating curve and is increased in magnitude. Therefore the curves show a large temperature hysteresis (24 K for the maximum magnetisation).

Fig 5.2 shows the magnetisation versus temperature curve over a temperature range from 5 K to 356K obtained with two cooling measurements. The overall change in magnetisation is still very small, with a difference between the maximum and minimum magnetisation of about  $2 \text{ J}/(\text{T kg})$ . However, the curve is quite unusual as the minimum magnetisation is measured at 5 K. Above 5

K the magnetisation increases slowly up to a temperature of 30 K and then increases more rapidly towards the maximum magnetisation at 278 K. Beyond 280 K the magnetisation decreases rapidly. The curve seems to form a very broad peak around 278 K. It is possible that the observed behaviour is due to the f.c.c.  $\rightarrow$  f.c.t. phase transition as the peak maximum is found at 278 K which is approximately the transition temperature observed in the resistivity measurements. The increase in magnetisation over such a wide temperature range could be due to the developing tetragonality of the f.c.t. phase. No change in the magnetisation versus temperature curve indicating a f.c.t. to b.c.t. transition could be observed. The fact, that the decrease in the magnetisation curve continues over a temperature range where the sample is transformed to b.c.t., could be explained with the observations by Foos et al. [11]. They found, that the b.c.t. transition is not complete, yet that both phases coexist over a wide temperature range. However, the observed change is small, with a change of 2% between maximum and minimum magnetisation in the temperature range 250 K - 355 K and a difference of 4% between maximum and minimum magnetisation in the temperature range 5 K - 355 K.

The observed change in magnetisation might be connected with the f.c.c.  $\rightarrow$  f.c.t. phase transition found in the sample, but no definite proof can be given.

In fig. 5.3 the magnetisation versus temperature for different applied fields is shown, the data were obtained from isotherm measurements. It can be seen that the magnetisation over temperature for low fields exhibits the same behaviour as described above. However, if the fields are higher,  $\geq 0.5$  T, the magnetisation decreases monotonously with rising temperature. A applied strong magnetic field suppresses the increase in magnetisation with rising temperature. It should be pointed out again that the overall change in the curves of the low field measurements is very small.

In fig. 5.4 the magnetisation versus temperature curve for a single crystalline sample is shown. The temperature variation of the obtained magnetisation curve

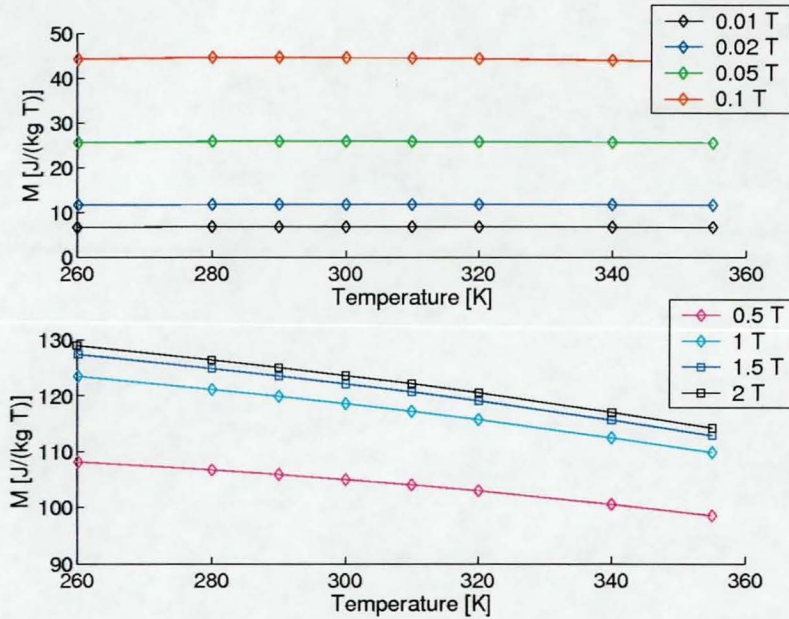


Figure 5.3: Magnetisation versus temperature obtained from the isotherms.

is very large compared to the results obtained in the polycrystal measurements. The magnetisation obtained in the single crystal measurements is also significantly smaller than the bulk magnetisation obtained in the measurements with a polycrystalline sample. The peak like behaviour which could be observed in the bulk measurements was not observed any more. A Hysteresis can be seen between the heating and the cooling curve. The crystal used for this experiment did not show a f.c.c.  $\rightarrow$  f.c.t. phase transition. The sample was aligned with a  $[110]$  axis parallel to the applied magnetic field.

Magnetisation  $M$  versus magnetic induction  $B$  measurements were carried out for the temperature range from 260 K to 355 K with the polycrystalline sample. The curves rise sharply at low fields and remain almost constant at fields larger than 2 T, see fig. 5.5. The area enclosed between the magnetisation curve and the y-axis in a magnetisation versus magnetic field measurement is proportional to the anisotropy energy of the material in the measured crystalline direction. Because a polycrystalline sample was measured, the enclosed area is proportional

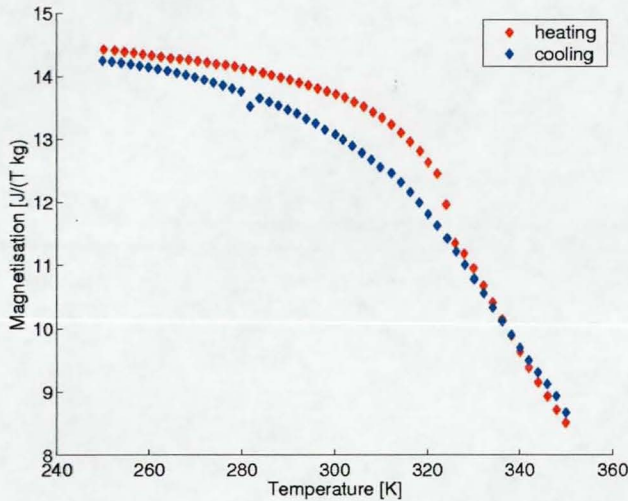


Figure 5.4: Magnetisation versus temperature in a single crystalline sample. The temperature step size was 2 K and during the measurements a field of 0.1 T was applied.

to the magnetic anisotropy energy averaged over all crystalline directions. As this area is small for the measurements carried out, the anisotropy energy of the crystal will be small.

The maximum magnetisation which is close to the saturation magnetisation decreases from  $131 \text{ J}/(\text{T kg})$  to  $117 \text{ J}/(\text{T kg})$  with rising temperature. The saturation magnetisation was found to be  $\sim 145 \text{ J}/(\text{T kg})$  at room temperature in [17] and  $\sim 160 \text{ J}/(\text{T kg})$  in [21]. This is slightly higher than the values reported here. Kussmann and Jessen [16] state that the saturation induction for an  $\text{Fe}_7\text{Pd}_3$  alloy is around 1.6 T, which matches the observation of the experiments carried out here. These show that the saturation induction lies between 1.5 T and 2 T.

To estimate the spontaneous magnetic moment per formula unit at different temperatures, Arrott plots were drawn from the magnetisation versus magnetic field measurements. The plots show a curved behaviour at low fields and are linear at high fields. A linear fit was made to the high temperature region, in order to estimate the intersection with the y-axis. Figure 5.6 shows the Arrott plots for the recorded temperatures and the linear interpolation of the high temperature

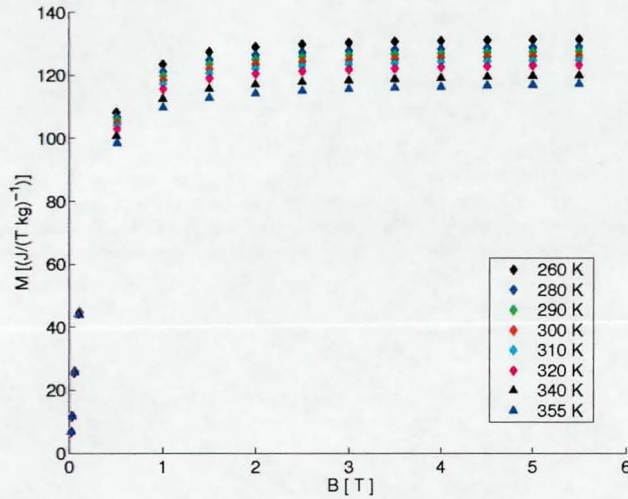


Figure 5.5: Magnetisation  $M$  versus Magnetic Induction  $B$

region.

The intersection of the linear interpolation of the Arrott plots gives the spontaneous magnetisation squared  $M^2 \left[ \frac{J^2}{kg^2 T^2} \right]$ , the magnetic moment per formula unit was then determined using the following equation

$$\mu(T) \frac{\mu_B}{10N} = M(T) \frac{J}{kgT} \cdot m_{rel} \frac{kg}{10mol} \cdot \frac{1}{N_A \mu_B} \frac{Tmol}{JN} \quad (5.8)$$

with  $m_{rel} = m_{mol_{Fe}} \cdot 7 + m_{mol_{Pd}} \cdot 3$  being the molar mass of  $Fe_7Pd_3$  per mol of a formula unit,  $N_A = 6.022 \cdot 10^{23}$  Avogadro's number,  $N$  stands for the number of atoms to which is normalised, so that  $10N$  means 10 atoms,  $\mu(T)$  the magnetic moment per formula unit and  $\mu_B = 9.274 \cdot 10^{-24} J/T$  the Bohr magneton. The magnetic moment per formula unit for the different temperatures is shown in the table in 5.7. It can be seen that the magnetic moment per formula unit decreases with increasing temperature as expected.

Some measurements were carried out twice once coming from a lower temperature and once coming from a higher temperature, indicated with a (c) in the table in fig. 5.7. The second set of measurements shows a slightly smaller magnetic moment, the biggest difference is observed for 320 K, where the difference

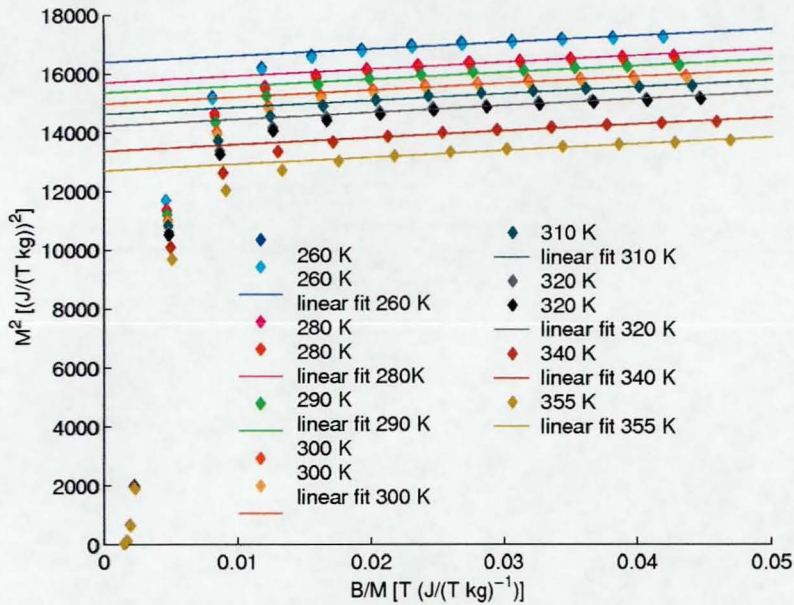
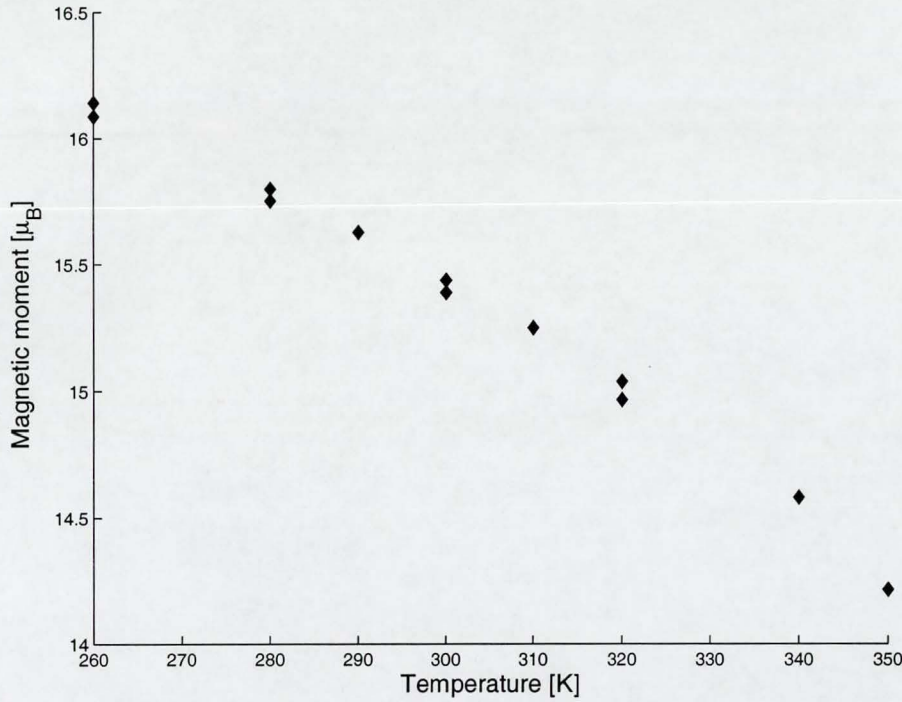


Figure 5.6: Arrott plots for the isotherm measurements combined with linear interpolations for the high temperature regions. At some temperatures measurements were carried out twice, the first set of temperatures was measured from low temperatures heating, after the measurement at the highest temperature the sample was cooled down again and some temperatures were measured a second time.

between the magnetic moments per formula unit is  $\Delta\mu_{320} = 0.0723\mu_B$ . This difference is probably due to hysteresis effects. For a measurement the sample was already exposed to a high field in the measurement before, this could have left the sample with a bulk magnetisation, when the next measurement was started. The Arrott plots might have been affected by this in the lower field region, resulting in a slightly smaller slope for the linear fit and therefore in a slightly higher  $M^2$  value. If the temperature in the measurement before was higher than in the following one, the remaining bulk magnetisation is expected to be smaller and would therefore have less influence on the next measurement. This explanation is supported by the fact that the biggest difference in magnetic moment occurs at 320 K, the temperature difference to the last measurement is 10 K coming from lower temperatures but 30 K coming from higher temperatures. This is the largest temperature difference between any two following isotherm measure-

Figure 5.7: Magnetic Moment per Formula Unit versus Temperature



T [K]	$\mu_{\text{formula unit}}$	$\mu_{\text{Fe-atoms/unit cell}}$	$\mu_{\text{Fe-atom}}$
260	16.141	4.519	2.306
260 (c)	16.086	4.504	2.299
280	15.797	4.423	2.257
280 (c)	15.750	4.410	2.250
290	15.624	4.375	2.232
300	15.434	4.322	2.205
300 (c)	15.386	4.308	2.198
310	15.247	4.269	2.178
320	15.035	4.210	2.148
320 (c)	14.963	4.190	2.138
340	14.579	4.082	2.083
355	14.214	3.980	2.031

( $\mu \pm 0.7\%$ ) [ $\mu_B$ ]

The magnetic moment per iron atom is calculated assuming that the palladium atoms do not have a contribution to the magnetisation.

ments. Further, the difference between the two Arrott plots shows indeed a larger difference at lower fields compared to high fields. However, the difference is small and the exact origin and magnitude is difficult to obtain.

The molar mass, used to calculate the magnetic moment per formula unit has been corrected for the weight loss (0.09%) the sample suffered during preparation. Another error which has to be taken into account is the error due to the mass of the sample, this error is determined by the standard deviation of the balance (0.02mg) with which the sample weight was measured. This uncertainty in the sample mass leads to a relative error of  $\Delta\mu_{mass} = 0.7\%$ . The error due to the mass uncertainty determines the overall error of the magnetic moment, which is shown in the table in fig. 5.7. The errors due to the resolution of the SQUID magnetometer and the linear fit were neglected because they are small.

Fig. 5.7 shows the estimated magnetic moment versus temperature. No sudden changes in this curve were observed. The structural phase transition does not seem to influence the overall magnetic moment. This can also be seen in fig. 5.3. It shows that the magnetisation versus temperature curve show a decrease in temperature for higher fields out of which the magnetic moment is determined.

The magnetic moment of  $\text{Fe}_7\text{Pd}_3$  was estimated to be  $2.1 \mu_B/\text{atom}$  at 0 K by Matsui et al. [13]. The magnetic moment per atom at 260 K was found to be  $1.614\mu_B/\text{atom}$  in the experiments carried out here.

Iron with an f.c.c. structure has a magnetic moment of  $\sim 2.8\mu_B/\text{atom}$  [37]. Brown et al. [37] investigated the magnetic moment in the Invar alloy  $\text{Fe}_{65}\text{Ni}_{35}$  using polarised neutrons. Their data show the average magnetic moment per iron atom with temperature. It is plausible to compare  $\text{Fe}_{65}\text{Ni}_{35}$  with  $\text{Fe}_7\text{Pd}_3$  because they are both Invar alloys with a similar iron content. Moreover, palladium is placed directly below Ni in the periodic table, which shows that the electronic configuration differs only in so far as an atomic shell is added (the magnetic moment is caused by the 4d shell in palladium and by the 3d shell in nickel). Elemental nickel is weakly ferromagnetic, whereas palladium is param-

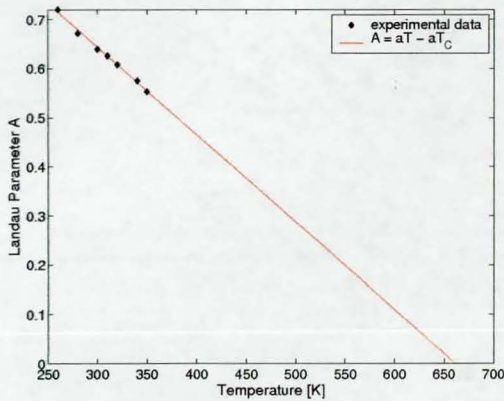


Figure 5.8: Linear fit to the Landau parameter  $A$  determined out of the Arrott plots. The fit gives  $a = -0.0018$  and  $-aT_C = 1.1759$ . The intersection with the x-axis shows the estimated Curie-temperature.

agnetic. The average magnetic moment per iron atom is  $2.01\mu_B$  for  $T = 0.6T_C$  and  $2.43\mu_B$  for  $T = 0.4T_C$  in  $\text{Fe}_{65}\text{Ni}_{35}$  according to Brown et al. [37]. The measurements for  $\text{Fe}_7\text{Pd}_3$  carried out here show  $2.031\mu_B$  for  $T = 0.54T_C$  and  $2.306\mu_B$  for  $T = 0.39T_C$ , assuming a Curie temperature of 660 K (see below) ( $2.25\mu_B$  for  $T = 0.51T_C$ ,  $2.083\mu_B$  for  $T = 0.60T_C$ , with  $T_C = 570$  K). The magnetic moment per Fe-atom, assuming that only iron contributes to the magnetic moment in  $\text{Fe}_7\text{Pd}_3$ , is therefore close to the average magnetic moment per iron atom in  $\text{Fe}_{65}\text{Ni}_{35}$ . A more detailed comparison is not possible because of the uncertainty in the knowledge of the Curie temperature (see below). At  $0.1T_C$  the average magnetic moment for an iron atom in  $\text{Fe}_{65}\text{Ni}_{35}$  is about  $2.86\mu_B$  which is similar to the magnetic moment determined by Matsui et al. [13] at low temperatures. Their data give a magnetic moment of  $3\mu_B/\text{Fe-atom}$ , if it is assumed that only iron contributes to the magnetisation in the sample. The comparison indicates that the magnetic moment on iron atoms is similar in  $\text{Fe}_{65}\text{Ni}_{35}$  and  $\text{Fe}_7\text{Pd}_3$  and that the assumption that the magnetic moment is caused by iron atoms only gives a good first approximation.

No measurements were carried out above the Curie temperature because the SQUID magnetometer can not be used above 355 K. However an attempt was

made to give an estimation of the Curie temperature. The coefficient  $A$  in the description of the Arrott plots has a linear temperature dependence  $A(T - T_C)$ , whereas the coefficient  $C$  is taken to be constant. The  $A$  values for the measured temperatures were determined and a linear fit was made (see fig. 5.8). The Curie temperature could be determined to be 662 K. It should be pointed out that the Curie temperature could not be determined accurately as the distance  $\Delta T$  between the estimated temperature and the measured data is about 3 times larger than the temperature range of the measured data. Nevertheless, the estimated Curie temperature matches fairly well with the literature, Matsui et al. found in [13] a Curie temperature of about 600 K and Cui et al. determined the Curie temperature to be 720 K [26]. Kussman and Jessen found a Curie temperature of 570 K [16].

# Chapter 6

## Neutron Diffraction Experiments

### 6.1 Introduction

Neutron diffraction experiments are a most powerful source for investigating the structures of materials. The great advantage of using neutrons compared to other sources, for instance electrons or X-rays, is that neutrons do not interact with the electrostatic potential caused by the electron distribution within a sample. This is the case because neutrons do not possess an electrical charge. However, they interact with nuclei within a sample, giving rise to nuclear scattering. Magnetic scattering is possible because neutrons are fermions with spin  $\frac{1}{2}$ . Magnetic scattering is caused by interaction of the neutron with unpaired spins and angular momenta (as far as they are not quenched) of electrons within a sample. The cross sections of these types of interaction are much smaller than the one for electrostatic interactions of X-ray and electron scattering and therefore neutrons can penetrate a sample much easier than electrons and X-rays can. Therefore neutrons provide information from deep within the sample. To investigate the structure of  $\text{Fe}_7\text{Pd}_3$  three types of neutron diffraction experiments were carried out at the ILL, Grenoble<sup>1</sup> using single crystals, all of them employing

---

<sup>1</sup>Institute Laue-Langevin (ILL), 6 rue Jules Horowitz, BP 156 - 38042 Grenoble, France

elastic Bragg scattering. Firstly, Laue back reflection experiments were carried out at the instrument S42B to determine the orientation and quality of the crystalline samples for later experiments. Secondly, single crystal diffraction with a monochromatic beam was performed on the four-axis diffractometer D9. And most importantly polarised neutron diffraction was carried out on the polarised neutron diffractometer D3. An attempt was made to determine phase transition temperatures and lattice parameters on the single crystal diffractometer D9 and then investigate magnetic structure factors of the low and high temperature phases using the polarised neutron diffractometer D3. However, despite repeated heat treatments the crystals did not undergo a phase transition at the expected temperature, although the high temperature phase exhibited the expected f.c.c. structure. Therefore the low temperature phase could not be investigated.

## 6.2 Theoretical Background

### 6.2.1 Neutron Cross Section

The basic quantity determining neutron scattering experiments is the partial differential cross section  $\frac{d^2\sigma}{d\Omega dE'}$ , which gives the fraction of neutrons of incident energy  $E$  scattered into a space element of solid angle  $d\Omega$  with a final energy between  $E'$  and  $E'+dE'$ . Assuming elastic scattering the energy is held fixed and therefore the scattering is described by the differential cross section  $\frac{d\sigma}{d\Omega}$ . If the incident neutron flux is  $N$  then the number of scattered neutrons per unit time into the element of  $d\Omega$  is #neutrons =  $N(\frac{d\sigma}{d\Omega})d\Omega$ . A neutron is described by its wave function with wave vector  $\mathbf{k}$ . To obtain the differential cross section the transition probability from a neutron state with wave vector  $\mathbf{k}$  to the neutron state with wave vector  $\mathbf{k}'$  must be known. This probability is given by Fermi's golden rule, which states:

$$w_{\mathbf{k}\rightarrow\mathbf{k}'} = \frac{2\pi}{\hbar} \left| \int d\mathbf{r} \psi_{\mathbf{k}'}^* \hat{V} \psi_{\mathbf{k}} \right|^2 \rho_{\mathbf{k}'}(E) \quad (6.1)$$

with the interaction potential  $V$ , the neutron wave functions  $\psi$ ,  $\mathbf{k}$  and  $\mathbf{k}'$  denoting the wave vectors for the initial and final state respectively, and  $\rho_{\mathbf{k}'}$  the density of final scattering states. Here the  $|\dots|^2$  term gives the transition probability from wave vector  $\mathbf{k}$  to wave vector  $\mathbf{k}'$  and  $\rho_{\mathbf{k}'}(E)$  represents the probability that this state gets occupied.

Assuming that the neutron wave functions are plane waves, which are normalised to a large box with volume  $L^3$ , the density of final states can be written as

$$\rho_{\mathbf{k}'}(E) = \left(\frac{L}{2\pi}\right)^3 \frac{d\mathbf{k}'}{dE} \quad (6.2)$$

Recalling that  $d\mathbf{k}' = k'^2 d\Omega dk' = k^2 d\Omega dk = dk$  and  $dE = \frac{\hbar^2 k}{m} dk$  the density can be expressed in terms of  $d\Omega$

$$\rho_{\mathbf{k}'}(E) = \left(\frac{L}{2\pi}\right)^3 \frac{mk'}{\hbar^2} d\Omega \quad (6.3)$$

The incident neutron flux can be described as the velocity of incident neutrons over volume, that is  $N = \frac{\hbar k}{mL^3}$ .

Considering the differential cross section with the equations above, one obtains:

$$\begin{aligned} d\sigma &= \frac{W_{\mathbf{k} \rightarrow \mathbf{k}'}}{N} \\ &= L^6 \left(\frac{m}{2\pi\hbar^2}\right)^2 \frac{k'}{k} \left| \int d\mathbf{r} \psi_{\mathbf{k}'}^* \hat{V} \psi_{\mathbf{k}} \right|^2 d\Omega \end{aligned} \quad (6.4)$$

For the case of elastic scattering  $k=k'$  and the ratio  $k'/k$  is one. This gives for the differential cross section

$$\frac{d\sigma}{d\Omega} = \left| \langle \mathbf{k}' | \hat{V} | \mathbf{k} \rangle \right|^2 \quad (6.5)$$

with the matrix element being

$$\langle \mathbf{k}' | \hat{V} | \mathbf{k} \rangle = \left(\frac{m}{2\pi\hbar^2}\right) \int d\mathbf{r} e^{(-i\mathbf{k}'\mathbf{r})} \hat{V} e^{(i\mathbf{k}\mathbf{r})} \quad (6.6)$$

Finally the spin states of the neutrons must be taken into account. The spin states are denoted as  $|\sigma\rangle$  so that the target-neutron system can be characterised by product states  $|\mathbf{k}\sigma\rangle = |\mathbf{k}\rangle |\sigma\rangle$ . The probability distribution is expressed by the weighted sum over  $\sigma$  and  $\sigma'$  with probabilities  $p_\sigma$  that this state is occupied. The following equation for the partial cross section is then obtained:

$$\frac{d\sigma}{d\Omega} = \sum_{\sigma} p_{\sigma} \sum_{\sigma'} | \langle \mathbf{k}'\sigma' | \hat{V} | \mathbf{k}\sigma \rangle |^2 \quad (6.7)$$

It should be noted that this expression has only approximate character since the transition probability expressed by Fermi's golden rule 6.1 is derived from perturbation theory and is not exact. If the possibility of an energy change of the neutrons is taken into account, the target system can change its state and therefore its states have to be taken into account as well as the energy conservation law. Equation 6.7 becomes the first Born approximation if the possibility of inelastic scattering is considered as well. [40] [42]

## 6.2.2 Elastic Coherent Scattering

To evaluate equation 6.7 an expression for the interaction potential  $\hat{V}$  must be found. A first approximation is to evaluate scattering of rigidly bound nuclei.

Because of the short range interaction potential of nuclei the neutron-nucleus interaction can only contain s-wave components and is therefore essentially isotropic.

The isotropic scattering can be characterised by a single complex parameter the scattering length  $b$ , where the imaginary part is representing absorptions and is, in general, small.

Using equation 6.7 only an interaction potential  $\hat{V}(\mathbf{r})$  depending on a delta function gives the required isotropic scattering. Considering a rigid array of  $N$  nuclei the interaction potential can be expressed by the Fermi pseudo-potential:

$$\hat{V}(\mathbf{r}) = \frac{2\pi\hbar^2}{m} \sum_i b_i \delta(\mathbf{r} - \mathbf{R}_i) \quad (6.8)$$

with  $b_l$  being the scattering length and  $\mathbf{R}_l$  the position of the  $l^{\text{th}}$  nuclei. Thus the matrix element becomes

$$\begin{aligned} \langle \mathbf{k}' | \hat{V} | \mathbf{k} \rangle &= \frac{2\pi\hbar^2}{m} \sum_l b_l \int d\mathbf{r} e^{-i\mathbf{k}'\cdot\mathbf{r}} \delta(\mathbf{r} - \mathbf{R}_l) e^{i\mathbf{k}\cdot\mathbf{r}} \\ &= \frac{2\pi\hbar^2}{m} \sum_l b_l e^{i\Delta\mathbf{k}\cdot\mathbf{R}_l} \end{aligned} \quad (6.9)$$

$\Delta\mathbf{k}$  represents the scattering vector  $\Delta\mathbf{k} = \mathbf{k} - \mathbf{k}'$ . Substituting 6.9 into equation 6.7 the partial cross section becomes

$$\frac{d\sigma}{d\Omega} = \sum_{\sigma} p_{\sigma} \sum_{\sigma'} \left| \left\langle \sigma' \left| \sum_l b_l e^{i\Delta\mathbf{k}\cdot\mathbf{R}_l} \right| \sigma \right\rangle \right|^2 \quad (6.10)$$

With the assumed potential the nuclei are rigidly bound at their positions. It is further assumed that the energy of the crystal is independent of the nuclear spin orientations. Then the cross section does not depend on the spin states and the sum over sigma can be done by closure. Thus the differential cross section (elastic scattering) becomes

$$\frac{d\sigma}{d\Omega} = \sum_{l,l'} e^{i\Delta\mathbf{k}\cdot(\mathbf{R}_l - \mathbf{R}_{l'})} \overline{b_{l'}^* b_l} \quad (6.11)$$

Considering that correlations between  $b_l$  and  $b_{l'}$  are only present if  $l=l'$ , the general expression  $\overline{b_{l'}^* b_l} = |\bar{b}|^2 + \delta_{ll'} [|\bar{b}|^2 - |\bar{b}|^2]$  is found. Using this relation, the differential cross section can be split into

$$\frac{d\sigma}{d\Omega} = \left( \frac{d\sigma}{d\Omega} \right)_{\text{coh}} + \left( \frac{d\sigma}{d\Omega} \right)_{\text{incoh}} \quad (6.12)$$

with the coherent cross section being

$$\left( \frac{d\sigma}{d\Omega} \right)_{\text{coh}} = |\bar{b}|^2 \sum_l e^{i\Delta\mathbf{k}\cdot\mathbf{R}_l} \quad (6.13)$$

In the following only the coherent cross section will be of interest. Considering a crystal, the atomic positions are usually described as a combination of a lattice vector  $\mathbf{g}$  and a position vector  $\mathbf{r}_N$ , which describes the atom positions with respect to the lattice points. The coherent cross section can then be written as:

$$\left(\frac{d\sigma}{d\Omega}\right)_{\text{coh}} = \sum_{\mathbf{g}} e^{i\Delta\mathbf{k}\mathbf{g}} |F_N(\Delta\mathbf{k})|^2 \quad (6.14)$$

with

$$F_N(\Delta\mathbf{k}) = \sum_{\mathbf{r}_N} e^{i\Delta\mathbf{k}\mathbf{r}_N} \bar{b}_{\mathbf{r}_N} e^{-W(\Delta\mathbf{k})} \quad (6.15)$$

$e^{-W(\Delta\mathbf{k})}$  is the Debye-Waller factor and takes the temperature dependence of the scattering into account. If the scattering vector is zero or equal to a reciprocal lattice vector then the cross section becomes very large because all the terms in the sum over  $\mathbf{g}$  will add up in phase. In contrast, if  $\Delta\mathbf{k}$  is not a reciprocal lattice vector the sum will drop to zero quickly. Therefore the cross section can be rewritten as

$$\left(\frac{d\sigma}{d\Omega}\right)_{\text{coh}} = \frac{N(2\pi)^3}{V_0} \sum_{\mathbf{K}} \delta(\Delta\mathbf{k} - \mathbf{K}) |F_N(\Delta\mathbf{k})|^2 \quad (6.16)$$

Equation 6.16 shows that coherent elastic scattering only occurs when the scattering vector  $\Delta\mathbf{k}$  equals a reciprocal lattice vector  $\mathbf{K}$ . This is the Laue-equation which is discussed in more detail in 7.2.

### 6.2.3 Coherent Elastic Magnetic Scattering

The differential cross section for magnetic scattering can be expressed in terms of the magnetisation density  $\mathbf{m}(\mathbf{r})$  in a ferromagnetic crystal.

$$\frac{d\sigma}{d\Omega} = \left(\frac{\gamma e^2}{m_e c^2}\right)^2 \left| \int d\mathbf{r} e^{i\Delta\mathbf{k}\mathbf{r}} (\widetilde{\Delta\mathbf{k}} \times \mathbf{m}(\mathbf{r}) \times \widetilde{\Delta\mathbf{k}}) \right|^2 \quad (6.17)$$

$\gamma$  denotes the gyromagnetic factor of the neutron, which is  $\gamma = -1.91$  and  $\widetilde{\Delta\mathbf{k}}$  is a unit vector in the direction of the scattering vector  $\Delta\mathbf{k}$ . Because  $\mathbf{m}(\mathbf{r})$  is a periodic function the following equation can be defined:

$$\int_V d\mathbf{r} e^{i(\Delta\mathbf{k}\mathbf{r})} \mathbf{m}(\mathbf{r}) = \frac{(2\pi)^3}{V_0} \sum_{\mathbf{K}} \delta(\Delta\mathbf{k} - \mathbf{K}) \mathbf{F}_M(\mathbf{K}) \quad (6.18)$$

$F_M$  is defined as the magnetic unit-cell vector structure factor. Inverting the last equation the following is obtained for the magnetisation density distribution.

$$\mathbf{m}(\mathbf{r}) = \frac{1}{V_0} \sum_{\mathbf{K}} e^{-i\mathbf{K}\mathbf{r}} \mathbf{F}_M(\mathbf{K}) \quad (6.19)$$

If this equation is multiplied by  $e^{i\mathbf{K}'\mathbf{r}}$  and integrated over a unit cell volume  $V_0$

$$\int_{V_0} d\mathbf{r} e^{i\mathbf{K}'\mathbf{r}} \mathbf{m}(\mathbf{r}) = \frac{1}{V_0} \sum_{\mathbf{K}} \mathbf{F}_M(\mathbf{K}) \int_{V_0} d\mathbf{r} e^{i(\mathbf{K}'-\mathbf{K})\mathbf{r}} \quad (6.20)$$

the magnetic unit-cell vector structure factor can be obtained. The integral on the right hand side equals zero unless  $\mathbf{K}$  and  $\mathbf{K}'$  coincide and for this case it is equal to the unit cell volume  $V_0$ . Thus the magnetic structure factor becomes

$$F(\mathbf{K}) = \int_{V_0} d\mathbf{r} e^{i\mathbf{K}\mathbf{r}} \mathbf{m}(\mathbf{r}) \quad (6.21)$$

It can be seen from this equation that the magnetisation density is determined completely by the knowledge of the magnetic structure factor  $F_M(\mathbf{K})$  at the lattice points of the reciprocal lattice only. Therefore it can be estimated employing Bragg-scattering, which can determine  $F_M(\mathbf{K})$ . It should be also noted that the magnetisation density  $\mathbf{m}(\mathbf{r})$  can be determined by the knowledge of the measured structure factors only. No model is required to determine  $\mathbf{m}(\mathbf{r})$ . In practice, it is of course not possible to measure the magnetic structure factor at all Bragg-reflections, and the information gained about the magnetisation density is limited. Then a model fit may give a better interpretation of the data than a direct reconstruction using Fourier-transformation.

The partial cross section for coherent magnetic scattering can be rewritten in terms of the magnetic structure factor using the equations above. It has the same periodicity as the partial cross section for nuclear scattering.

### Coherent Elastic Magnetic Scattering with Polarised Neutrons

In general, magnetic scattering is much smaller than nuclear scattering. In a ferromagnetic crystal the magnetisation density  $\mathbf{m}(\mathbf{r})$  will have the same periodicity as the lattice. Therefore Bragg peaks of nuclear and magnetic scattering

will appear at the same position. So accurate measurements of the magnetic scattering intensity seem to be very difficult. However, for polarised neutrons the cross section for elastic scattering contains a magnetic-nuclear interference term, which is linear in the magnetic scattering. That makes it possible to measure small magnetic cross sections with very high accuracy.

For unpolarised neutrons and a ferromagnetic sample the scattered intensity of neutrons at the Bragg peaks will be proportional to the square of nuclear  $F_N$  and magnetic  $F_M$  structure factors respectively.

$$I \sim |F_N|^2 + |F_M|^2 \quad (6.22)$$

In an experimental arrangement where the neutron beam is polarised either parallel or antiparallel to the oriented spins in the sample and the magnetic moments of the sample are oriented perpendicular to the scattering plane, the intensity of the scattered neutrons will depend on the nuclear and magnetic structure factor squared in the following manner:

$$I^\pm \sim |F_N \pm F_M|^2 \quad (6.23)$$

+ describes the parallel and - the antiparallel polarisation of the neutron beam with respect to the spin orientation. To obtain the magnetic structure factor with an experimental arrangement as described above, the flipping ratios at the Bragg reflections are measured. Here the flipping ratio is defined as the ratio of the intensities of scattering with the two polarisation directions ( $\pm$ ) for the incident neutron beam.

$$R(\Delta\mathbf{k}) = \frac{I^+(\Delta\mathbf{k})}{I^-(\Delta\mathbf{k})} = \frac{|F_N(\Delta\mathbf{K}) + F_M(\Delta\mathbf{k})|^2}{|F_N(\Delta\mathbf{K}) - F_M(\Delta\mathbf{k})|^2} \quad (6.24)$$

If the nuclear scattering factors are known the magnetic scattering factors can be determined using the above equation. The magnetisation density distribution  $\mathbf{m}(\mathbf{r})$  can now be determined from a knowledge of the magnetic structure factors at the Bragg positions. As shown in section 6.2.3 the magnetic structure

factor is defined such that the magnetic density is described as the sum of the Fourier transforms of the magnetic structure factors at reciprocal lattice points. A possibility to obtain the magnetic density distribution is to perform a Fourier-transformation over all measured reflections. However, these method has some serious disadvantages as only a small number of reflections can practically be measured. [41]

Another possibility to evaluate the magnetisation distribution is, to compare a model with the obtained experimental data. A simple model is obtained by a multipolar expansion around a nucleus at rest, the magnetic scattering on each lattice site is associated with a form factor.

$$F_i(\Delta\mathbf{k}) = \langle J_0(\Delta\mathbf{k}) \rangle + a_1 + a_2 A(\Delta\mathbf{k}) \langle J_4(\Delta\mathbf{k}) \rangle \quad (6.25)$$

with

$$\langle J_i(\Delta\mathbf{k}) \rangle = \int_0^{\text{inf}} J_i(\Delta kr) U^2(r) dr^3 \quad (6.26)$$

where  $J_i(\Delta\mathbf{k})$  is a spherical Bessel-function of  $i^{\text{th}}$  order,  $U^2(r)$  is the radial distribution function of the magnetic electrons,  $a_1$  describes an expansion of the form factor and  $a_2$  shows the degree of asphericity of the moment distribution.  $A(\Delta\mathbf{k})$  is a geometrical factor depending on the reflection hkl at which the form factor is evaluated. In more sophisticated models other form factor contributions such as  $\langle J_2 \rangle$  have to be considered.  $\langle J_2 \rangle$  describes a derivation from a spherical electron distribution of the electrons in the d-band.

An f.c.c. structure has four lattice sites. For the case of a disordered structure all lattice sites will be equivalent, so that the magnetic structure factor becomes:

$$F_M(\Delta\mathbf{k}) = 4 \cdot F_i(\Delta\mathbf{k}) \quad (6.27)$$

For forward scattering  $\Delta\mathbf{k} = 0$   $F_M$  is equal to the total magnetic moment per unit cell

$$F_M(0) = 4\mu_{\text{atom}} \quad (6.28)$$

[38][39]

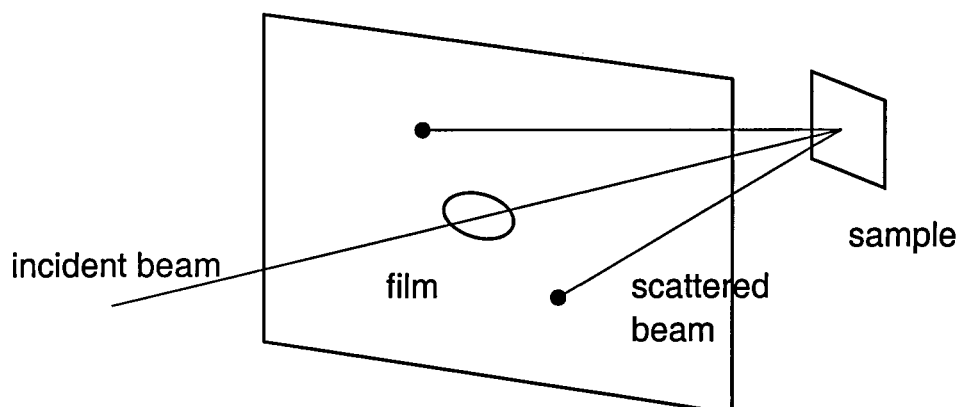


Figure 6.1: Schematical drawing of the Laue back reflection arrangement

The incident polychromatic beam hits the single crystalline target. Bragg reflection will occur for each set of lattice planes at a suitable wavelength  $\lambda$ . For each non equivalent set of planes the scattering angle  $\theta$  is different. Therefore the scattered beam for each plane set will be reflected to a different position of the film. The film will show a point pattern, with each point coming from a set of lattice spacings and their multiples and the beam associated with each point will have a different wavelength  $\lambda$  (and their harmonics  $\lambda/n$ ). The symmetry of the pattern will reflect the symmetry of the crystal.

## 6.3 Laue diffraction method

### 6.3.1 Introduction and Background

The method of Laue back reflection uses a non-monochromatic incident beam hitting a single crystalline target and the back reflections are recorded on a photographic film, see the schematic drawing in fig. 6.1. Since the crystal is held fixed during the experiment the scattering angle  $\theta$  is held fixed for each set of lattice planes. As lattice spacing and scattering angle are held fixed for each set of planes, only the wave length  $\lambda$  is free to vary to fulfil the Bragg law (7.1). A set of planes will therefore 'select' a suitable wavelength which fulfils the Bragg equation and reflect it. A pattern of spots will be recorded on the film, each spot corresponding to a set of lattice planes. However, a multiple set of planes, such as (220) to (110), will give rise to scattering under the same angle  $\theta$  but with a wavelength of  $\lambda/n$ . The set of multiple planes will have a lattice spacing of  $d/n$ ,

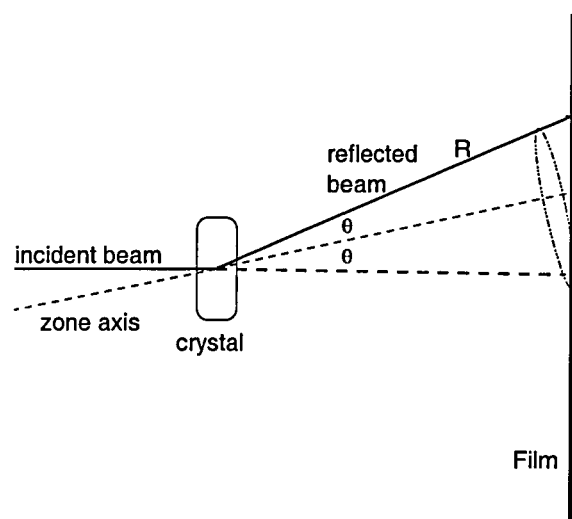


Figure 6.2: Schematical drawing to demonstrate the nature of the lines in Laue photographs. In this sketch the arrangement is that for transition photographs, not for the back reflection experiments employed in the measurements. However, the principal nature of the lines in the Laue photograph remains the same, but for back reflection experiments hyperbolas instead of ellipses will be observed.

This drawing was made after [43] fig. 4.14

if  $n$  is the multiplicity factor, therefore the Bragg-equation can be fulfilled with a wavelength  $\lambda/n$  and the same scattering angle. The possibility of reflections to occur is of course restricted by the employed wave length range of the incident beam.

The observed spots on a Laue photograph will all lie on cone intersections, which are hyperbolas for a back reflection arrangement. All spots lying on one curve arise through reflections of lattice planes which lie in one zone. This behaviour is described in sketch 6.2. The effect of the zone of the reflection pattern can be imagined by rotating the crystal around the corresponding zone axis and the reflection beam will wander forming a cone. The Laue film will then show a plane intersection with this cone. On a Laue photograph discrete spots rather than a continuous line will appear because the number of lattice planes lying in one zone will be finite.

In general a Laue photograph will exhibit no symmetry, however, if the incident beam is along a high symmetry axis of the crystalline sample the recorded pattern will show the symmetry of the crystal projected onto the plane in which the film lies. An important feature of Laue photographs is, that the elliptical curves become straight lines for those zones which lie perpendicular to the axis of the incident beam.

Although it is possible to gain structural information out of Laue photographs it is comparatively difficult to obtain the required data with good accuracy. Other methods such as powder diffraction are often more appropriate. Still Laue diffraction is an easy and widely used method to orientate single crystals and proof their quality. It was used for this purpose in the experiments carried out. [43][44]

### 6.3.2 Experimental Procedure and Results

The Laue diffraction experiments were carried out at the S42B experiment at the ILL in Grenoble. The experimental arrangement was as following. A polychromatic beam was lead along an optical bench. The film was fixed perpendicular to the beam on the bench. The film was placed in a metallic box with a hole in the middle of the box and the film in order to let the beam pass through. The metallic box protected the film from light and provided a shield for diffuse scattering on the side of the incident beam, where it was made of Cadmium, which strongly absorbs neutrons. The beam passes through the film and hits the sample which is placed on a goniometer by means of wax. The goniometer can be moved along the bench so that the sample film distance can be varied. In the experiments carried out, the film sample distance was held as small as possible in order to record as many spots as possible. The goniometer allowed the sample to be rotated around three perpendicular axes. It was important to make sure that the beam would not hit the wax because this gives rise to diffuse scattering which disturbs the Laue pattern on the film. During the experiment the whole

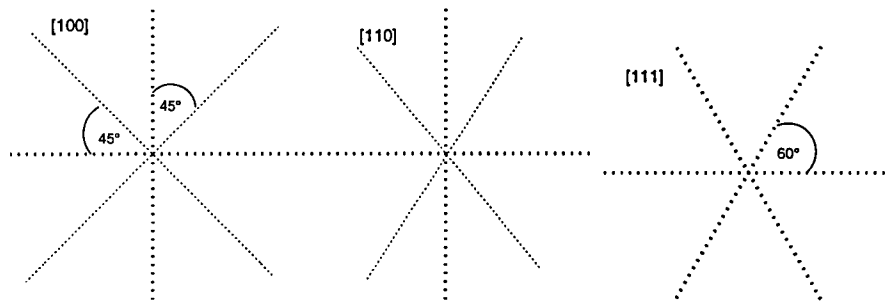


Figure 6.3: Schematic drawing of the symmetry appearance of the observed high symmetry pictures with the incident beam along the denoted axes

arrangement was covered with a lead-cadmium shield to protect the environment from radiation. The optimal exposure time varied depending on the crystal size, the smaller the crystal the longer the exposure time has to be to obtain a clear picture. This is understood considering that for a smaller crystal a set of lattice planes contains less planes than in a larger crystal, so there are less possibilities of scattering and the scattered intensity will be smaller. The average exposure time was about 45 min which resulted in good photographs for the given samples.

The  $\text{Fe}_7\text{Pd}_3$  crystals examined were of cubic symmetry. To orientate a crystal pictures which show a high symmetry pattern must be examined. The first aim is therefore to obtain such a high symmetry picture. To achieve this, 'promising' spots will be moved to the centre of the photograph so that the corresponding axis is parallel to the incident beam. 'Promising spots' are usually of a high intensity and normally several lines of spots will intersect at this spot. The angle of rotation necessary to move a spot into the centre of the photograph can be obtained easily, if the distance between the spot and the centre of the photograph and the distance between the film and the sample is known, by using  $\tan(2\theta) = R/\Delta(\text{crystal-film})$  (see 6.2). Three types of high symmetry pictures were observed, those along an 100 axis, those along an 110 axis and those along an 111 axis.

If the incident beam is oriented parallel to an  $[100]$  axis a pattern of two sets of two perpendicular lines which are rotated by  $45^\circ$  will appear, see fig. 6.3 and 6.4. Each of these crosses contains two identical lines. The picture therefore exhibits a four-fold rotational symmetry, that is the pattern repeats itself after rotation by  $90^\circ$ , and shows four mirror planes along the spot lines. The lines observed in the picture correspond to two  $[100]$  and two  $[110]$  axes in the crystal respectively, all lying in a plane perpendicular to the axis of the incident beam.

In case of the incident beam being parallel to an  $[110]$  axis a similar pattern of two crosses consisting of perpendicular lines will appear, but in one cross the lines will not be perfectly perpendicular and the angle between the crosses will differ slightly from  $45^\circ$ . The picture has therefore a two-fold symmetry, so that rotation around  $180^\circ$  reproduces the pattern. Further the pattern possesses two mirror planes along perpendicular spot lines on the film. (See fig. 6.3 and fig. 6.4)

If the incident beam hits the crystal parallel to an  $[111]$  axis the resulting picture will be of different symmetry. Three equivalent straight lines will appear each being rotated to the previous by  $60^\circ$ . The pattern therefore possesses 3 mirror planes and a six-fold rotational symmetry as the pattern can be reproduced after rotation by  $60^\circ$ . (See fig. 6.3 and 6.4)

To prepare the  $\text{Fe}_7\text{Pd}_3$  crystals for the polarised neutron experiments at the D3 neutron diffractometer they were checked for their quality and oriented so that a  $[110]$  axis would point upright. Neutron diffraction has a particular advantage for checking the quality of crystalline samples. As stated earlier, neutrons are able to penetrate a sample deeply due to their small interaction potential. That means that the scattered beam will show information from the whole sample and not only from the surface. If the crystal is entirely single, a clear picture with single spots will appear. If now the crystal has a second domain which has a slightly different orientation then the main one the spots on the pattern will effectively double, that is two spots will appear at slightly different positions instead of one.

The more domains are in the sample the more spots will appear and if their orientations are very different the resulting picture will contain several different layers of Laue patterns, one for each domain.

Several samples of  $\text{Fe}_7\text{Pd}_3$  were checked and suitable sections of a bulk were cut out in order to get single crystalline samples (see section 3.6). After gaining suitable single crystals, the samples were oriented.

To obtain an orientation with a  $[110]$  axis upright, the following considerations were applied. The angle between to crystallographic directions can be calculated considering their vector nature.

Considering a high symmetry picture with an  $[100]$  axis being parallel to the incident beam, it can be estimated that two other  $[100]$  axis will lie perpendicular to the incident axis as well as being perpendicular to each other. Then in the Laue photograph two straight lines crossing each other at an angle of  $90^\circ$  can be expected. Further, the incident axis is perpendicular to two  $[110]$  axes which are also perpendicular to each other and are rotated by  $45^\circ$  degrees to the  $[100]$  axes in the film plane. One of the observed crosses in a symmetry picture along a  $[100]$  axis will therefore contain two  $[110]$  lines and the other one two  $[100]$  lines. If the picture is oriented properly one of the lines will point straight upright already. The remaining task is to determine whether the upright axis is an  $[110]$  or an  $[100]$  axis. To determine this the crystal is rotated by  $90^\circ$  around the vertical axis in order to get the incident beam parallel to the axis which is represented by the horizontal line in the first  $[100]$  high symmetry picture. After rotating the crystal by  $90^\circ$  either a  $[100]$  or a  $[110]$  high symmetry picture can be expected. If the resulting picture shows a  $[110]$  symmetry the vertical line will represent an  $[110]$  axis and the crystal is oriented as required. If the resulting pattern shows a  $[100]$  symmetry the crystal can be rotated by  $90^\circ$  around the axis of the incident beam to get a  $[110]$  axis upright, if this is possible regarding the experimental arrangement. If not the procedure should be repeated with another high symmetry picture. In case a  $[111]$  high symmetry pattern is found

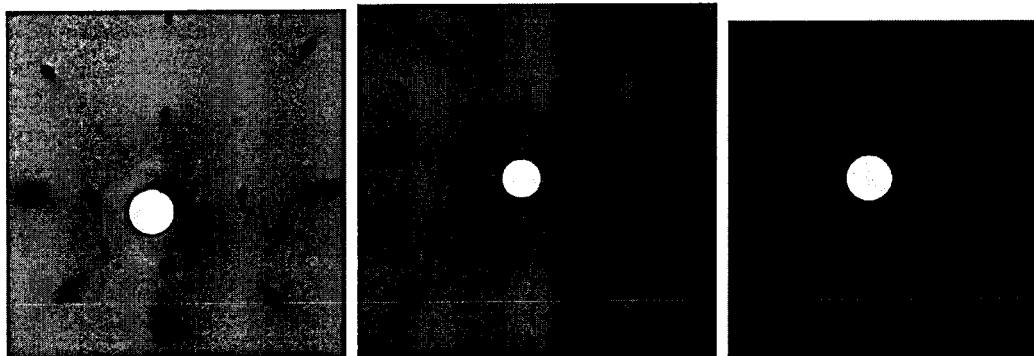


Figure 6.4: Left: Laue photograph showing a oriented crystal with an  $[110]$  axis upright. The incident beam is along an  $[100]$  axis. Middle: Laue photograph showing the crystal rotated by  $90^\circ$  around the vertical axis. The incident beam is along an  $[110]$  axis. Right: Laue photograph with an incident beam along an  $[111]$  axis.

a rotation by either  $54.7^\circ$  or  $35.3^\circ$  can be carried out to obtain a  $[100]$  picture because the angle between an  $[111]$  and a  $[100]$  axis will be one of these. The rotation will be around the vertical axis if the crystal is oriented so that one of the lines lies horizontally in the picture. Following this considerations several crystalline samples were oriented in order to carry out experiments at the neutron diffractometers D3 and D9 at the ILL in Grenoble.

### 6.3.3 Discussion

The samples used for further experiments could be proved to be entirely single crystalline. It was shown that the bulk crystals obtained were not single crystalline but contained several larger single crystals. Suitable regions could be determined and single crystals could be cut out of the bulk material. These samples could be oriented by considering that they should exhibit cubic symmetry and following the described procedure. The considerations of the angles between the different axes proved to be applicable with good accuracy when the crystals was rotated. Overall Laue diffraction method gives a direct impression regarding the symmetry of a crystal along certain directions and proved to be a useful method for orientating and examining single crystals.

## 6.4 Hot Neutron Four-Circle Diffractometer Measurements

### 6.4.1 The Hot Neutron Four-Circle Diffractometer D9

Measurements were carried out with the hot neutron four-circle diffractometer D9 at the ILL in Grenoble, France. The diffractometer can measure Bragg-reflections of single crystalline samples by rotating the single crystalline sample while the monochromatic beam is held in a fixed position. For different orientations of the sample different Bragg-peaks can be observed with an area detector. The diffractometer gives a continuous choice of wavelength between  $0.35\text{\AA}$  and  $0.84\text{\AA}$ . A Cu crystal is employed as a monochromator using the (220) plane, the whole experimental arrangement is placed on a Tanzboden floor and can be rotated to give a range of scattering angles at the monochromator, resulting in the choice of wavelength. The hot neutron source and the high angular range make it possible to observe high order reflections of the sample. This can be seen from the Bragg-equation, a big angular range will result in more observable reflections corresponding to different lattice spacings  $d$ . A shorter wavelength will give a smaller scattering angle  $\theta$  for a particular reflection, the distribution different scattering angles will be observable closer together and at lower angles, more reflections can be observed in a given range of the scattering angle  $\theta$ .

The intensities are detected with a small area detector covering  $8^\circ \times 8^\circ$  with a  $32 \times 32$  pixel detector. Fig. 6.5 shows the D9 diffractometer and vital elements are labelled.

The sample was glued to a metallic pin and placed into the beam. To make sure that the sample will remain in the beam throughout the measurement (under different rotations), the sample was rotated to several positions and then centred again.

For measurements at low temperatures the sample was placed into several

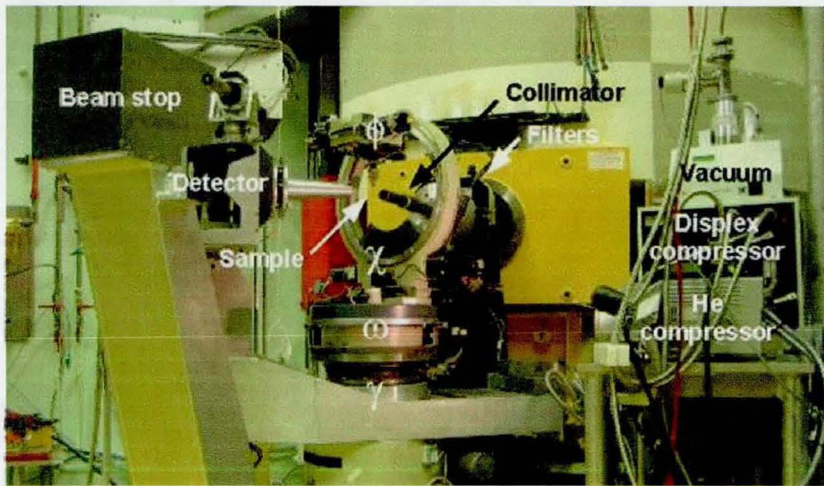


Figure 6.5: Hot Neutron Four-Circle Diffractometer D9. The picture was taken from [45]

aluminium flasks which were evacuated, the cooling was then done in the inner flask by Helium gas using a Displex, a heating device was placed within the sample mount, so that the temperature could be held constant using an intelligent temperature control device.

### 6.4.2 Results and Analysis

Two sets of measurements were carried out in Grenoble. In the first set reflections of three crystals were studied at room temperatures and lower temperatures. The crystals were oriented before by means of Laue diffraction and mounted on the diffractometer with a  $[110]$  direction approximately upright. First the position of some reflections were calculated and then the peaks were measured at their real position. The peaks were indexed and a matrix  $u_B$  was calculated by a computer program, which gives the relationship between the crystalline plane orientations and the laboratory system, so that for further measurements the reflections can be found by the computer program. The employed wavelength was  $0.84\text{\AA}$ . Several reflections for different sets of lattice planes were measured over different temperatures, the reflections were of non equal  $hkl$  values to be able to

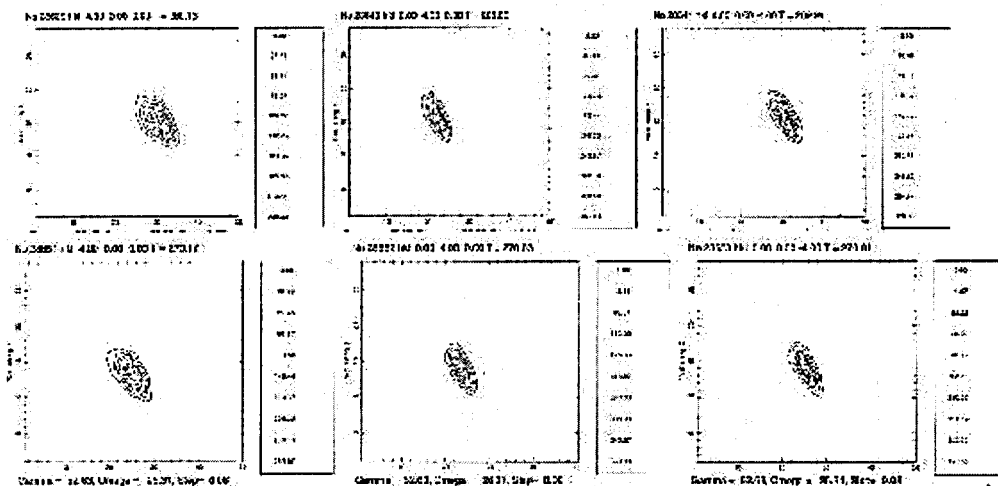


Figure 6.6: Bragg peaks for the  $(400)$ ,  $(040)$  and  $(00\bar{4})$  reflections (from left to right) at 290 K (first row) and 270 K (second row).

find a split in the peaks. This could be detected if a second peak appears on the area detector or the peak position changes significantly on the area detector. Temperatures between 300 K and 220 K were investigated for the first crystal and between 295 K and 260 K for the second one, measurements were made in steps of 10 K. The reflections at high temperatures showed the expected f.c.c. structure and the lattice parameter was determined to be  $3.71(5)\text{\AA}$  at room temperature. However, as the crystals were cooled down to lower temperatures no changes in the peaks were found and the samples exhibited no signs of transformation. At 220 K the peaks broadened extremely but no change in position or split could be seen, neither new peaks appeared at different positions. This change was proven to be irreversible even when the sample was heated up to room temperature again. Some of the results are shown for the reflections at different temperatures in fig. 6.6. Fig. 6.7 shows the broadened peaks at 220 K. The crystals were then heat treated again and a similar set of measurements was carried out with another crystal. However, no signs of a transformation were observed. The reason for this behaviour remains unclear, the heat treatment applied was the same as for the prepared polycrystalline samples, just the heating time was

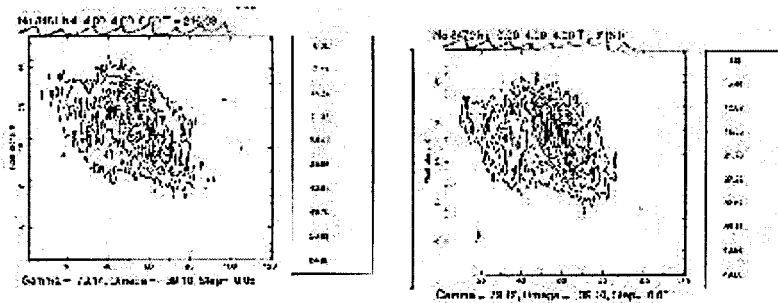


Figure 6.7: From left to right: (440) and (044) reflection at 216 K. The peaks broaden significantly and the maximum intensity is decreased compared to higher temperature measurements where the peak broadening was not observed. (The maximum intensity drops from  $\sim 120$  counts at 270 K to  $\sim 50$  counts at 220 K.)

extended in the second heat treatment. A possible explanation would be that the palladium concentration was not in the concentration range from 29.5% to 33% which exhibits the f.c.c.  $\rightarrow$  f.c.t. transformation. This would explain why the crystal did not transform, although the crystal exhibited the expected high temperature ( $\gamma$ Fe,Pd) f.c.c. structure. This structure is exhibited for a wide palladium concentration range, whereas the f.c.c.  $\rightarrow$  f.c.t. structure can only be observed over a very narrow concentration range.

## 6.5 The Spin Polarised Hot Neutron Beam Facility D3

The Spin Polarised Hot Neutron Diffractometer D3 gives the possibility to investigate single crystalline samples with hot, polarised neutrons. The principal diffraction arrangement is similar to the one of the diffractometer D9 discussed above. The single crystalline sample is hit by the beam and Bragg-peaks are observed under a certain orientation in a certain direction. In general, the crystal will be placed in a large cryomagnet which allows cooling to low temperatures and an applied field of up to 10 T. For this reason it is possible to lift the detec-

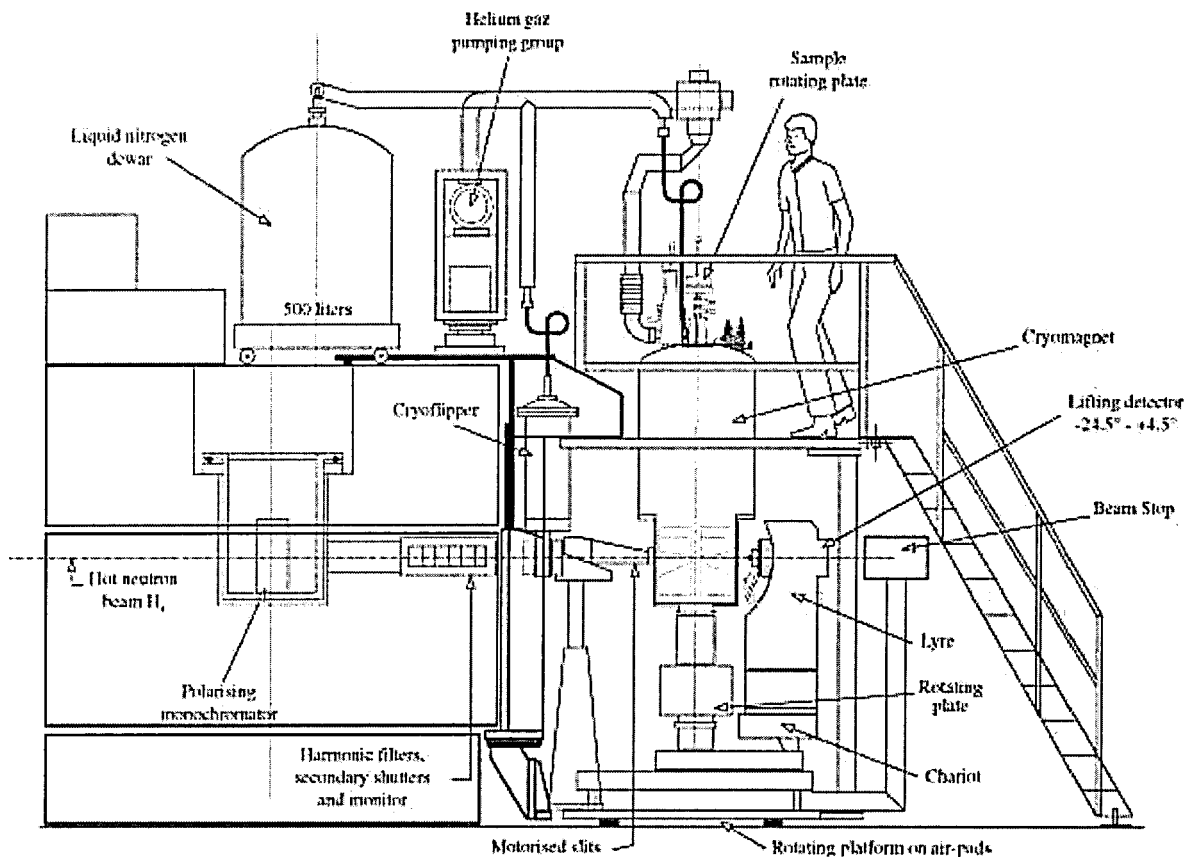


Figure 6.8: The Spin Polarised Hot Neutron Facility D3. The picture was taken from [46]

tor in a certain range and to rotate the sample just around its upright axis. A schematical drawing of the experimental arrangement is shown in fig. 6.8. Different wavelengths can be chosen by using different monochromator crystals. In the experiments carried out a wavelength of  $\lambda = 0.84\text{\AA}$  is used. The monochromator sends out neutrons with a certain wavelength and spin polarisation (upright), the beam passes through a cryoflipper to allow to flip the spin polarisation and hits the target in the cryomagnet. The Bragg intensities are measured for spin flip and non-spin-flip scattering and thus the flipping ratio can be determined. The D3 experiment is highly automated with the computer program Igor Pro controlling the arrangement. The intensity is recorded using a single  $^3\text{He}$  detector. To allow a precise sample orientation, four half shutters can be opened or closed in

front of the detector, Igor Pro possesses a refinement routine which will adjust the sample so that the maximum intensity is scattered in the middle of the detector and the sample orientation is very accurate. For the measurements carried out a field of 9.5 T is applied to prevent the neutron beam from depolarisation and to ensure saturation magnetisation in the direction perpendicular to the plane of the incident beam.

In order to obtain the magnetic structure factor, equation 6.24 is expressed in terms of the ratio between magnetic and nuclear structure factor  $\gamma = \frac{F_M(\mathbf{K})}{F_N(\mathbf{K})}$ :

$$R = \left( \frac{1 + \gamma}{1 - \gamma} \right)^2 \quad \Rightarrow \quad \gamma = \frac{R + 1 \pm 2\sqrt{R}}{R - 1} \quad (6.29)$$

The different signs  $\pm 2\sqrt{R}$  refer to  $|\gamma| \gtrless 1$ . In general  $\gamma < 1$  for 3d systems.

Thus equation 6.29 allows to determine the ratio between magnetic and nuclear structure factor using the measured flipping ratios.

Next, the nuclear structure factor was calculated considering the disordered f.c.c. structure of the sample. The required scattering lengths for iron and palladium can be obtained using tables such as [47]. Therefore the magnetic structure factor at the investigated reciprocal lattice points can be determined. The obtained magnetic structure factor can now be fitted to the model described in section 6.2.3. As stated there, the magnetic structure factor is proportional to the magnetic form factor on each lattice site. In the fits made it was assumed that the magnetic moment is caused by the iron atoms only and therefore the magnetic structure factor was normalised to the number of iron atoms per unit cell.

In the analysis described it was assumed that the measured Bragg intensities are determined by the nuclear and magnetic structure factors only. However, in general the measured intensities have to be corrected for some other influences. A possible influence on the measured intensities is absorption. This means that part of the neutron beam is absorbed by the nuclei rather than scattered. The

absorption coefficient depends on the types of elements involved and is negligible for  $\text{Fe}_7\text{Pd}_3$ .

Another influence on the Bragg intensities is given by the phenomenon of extinction. If a crystal is almost perfect, the beam will be reflected strongly from the first lattice plane and the incident beam is weaker for lattice planes deeper in the crystal. Thus the scattered intensity from lattice planes deep in the crystal will be weaker. This effect is only significant for strong reflections at low angles and their intensity will be weakened. An extinction factor can be calculated and the dependence on the scattering angle as well as a wave length dependence give the possibility to determine it using the experimental data. However, the measurements were only carried out at strong reflections and one wavelength, so that the extinction factor can not be determined. It can be assumed that extinction will not have a significant influence on the measurements because the crystal size was small and the crystal has a disordered structure.

Finally, because of the experimental arrangement, the vector nature of the magnetic structure factor has to be taken into account. The magnetic structure factor depends on the angle between the scattering vector and the direction of the magnetic moment. In section 6.2.3 this could be neglected because it was assumed that the scattering vector is perpendicular to the magnetic moment. In terms of the experimental arrangement at the D3 experiment this means that the beam and detector are positioned in the plane perpendicular to the magnetic field applied. At the D3 experiment it is possible to lift the detector out of the plane perpendicular to the applied field because this allows to measure more reflections for a sample. In this case the magnetic structure factor is modified by a factor of  $\sin(\alpha)$ , with  $\alpha$  being the angle measuring the deviation of the magnetic moment direction from the normal of the scattering plane. The obtained data were corrected for this influence.

### 6.5.1 Results and Analysis

The experiments were carried out on a small single crystalline sample, which was investigated using Laue-diffraction and the single crystal diffractometer D9 (see sections 6.3 and 6.4). It was shown by single crystal diffraction on D9, that the crystal does not undergo a martensitic f.c.c.  $\rightarrow$  f.c.t. phase transition at lower temperatures. Measurements of the flipping ratio have been carried out for different temperatures (260 K, 320 K) over a range of reflections. Furthermore, measurements of the flipping ratio for the (111) reflection were carried out over a range of temperatures between 260 K and 320 K. The magnetic structure factor at the reciprocal lattice points was determined as described above. The magnetic structure factor is proportional to the magnetic form factor at each lattice site as stated in section 6.2.3. Because of the disordered nature of the sample, the magnetic form factor at each lattice site will represent an average unit cell with 0.7 Fe + 0.3 Pd at each atomic position. It is therefore not possible to gain information about the difference in the magnetic moment distribution for the different atom types. However, in the fits made to the data it was assumed that only one atom type, iron, contributes to the magnetic moment distribution. Fig 6.9 and fig. 6.10 show the magnetic structure factor in units of  $\mu_B/\text{Fe-atoms}$ , fig. 6.11 shows the temperature dependence of the magnetic structure factor at the (111) reciprocal lattice point.

To compare the data to the model described in section 6.2.3, different form factor contributions, namely  $\langle j_0 \rangle$ ,  $\langle j_4 \rangle$  and in addition  $\langle j_2 \rangle$ , were fitted to the reflection data measured at 260 K and 320 K, the resulting curves are shown in fig. 6.9 and fig. 6.10. It can be seen that the spherical form factor  $\langle j_0 \rangle$  alone gives a very good fit to the data, while the other form factors are not significant. This shows that the magnetic density distribution is essentially isotropic at each lattice site.

No significant change in the curves can be found, when the temperature is

## FePd Magnetic scattering at 260 K

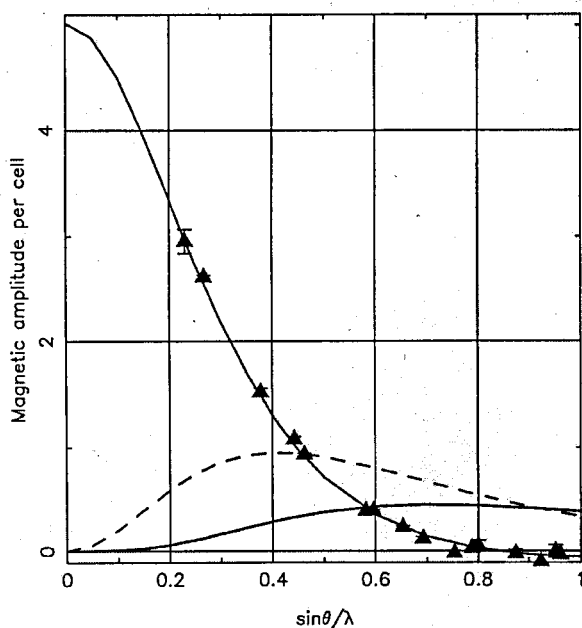


Figure 6.9: Magnetic structure factor over scattering angle at 260 K. A field of 9.5 T was applied, the wavelength employed was 0.84Å. The data are normalised to the number of iron atoms within a unit cell.

changed from 260 K to 320 K. Only a decrease in magnitude is observed, which is the expected temperature behaviour. Since the forward scattering gives the total magnetic moment per cell, the magnetic moment for forward scattering was determined from a model fit to the data and the obtained results are given in tab. 6.1.

The total magnetic moment per number of iron atoms per unit cell obtained with the polarised neutron scattering measurements is larger by  $0.501 \mu_B$  at 260 K compared with the moment determined using the SQUID magnetometer, while the value obtained in both measurements coincides for 320 K.

Fig. 6.11 shows the magnetic structure factor at the (111) reflection compared with the obtained SQUID data. For better comparison, the magnetic structure factor at the (111) reciprocal lattice point was scaled to match the total magnetic moment. This scale factor was slightly larger at 320 K than at 260 K. To scale the data the following equation was used  $\mu_{tot} = \mu_{(111)} \cdot x$ , with a scale factor  $x$ . The

## FePd Magnetic scattering

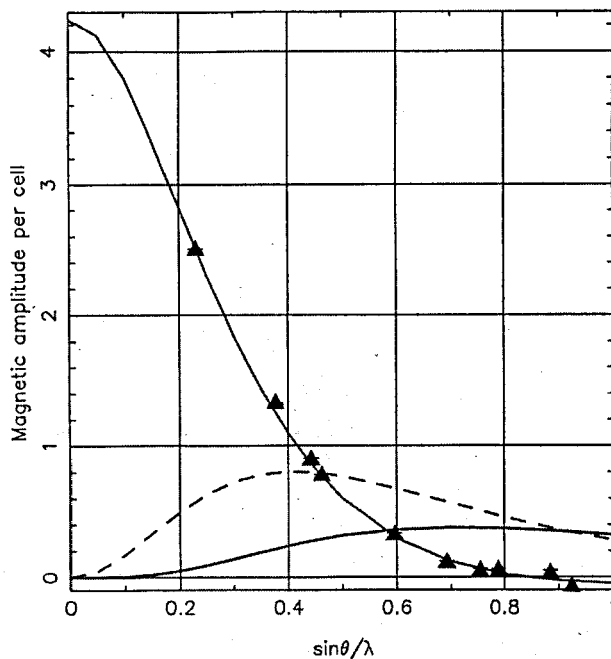


Figure 6.10: Magnetic structure factor over scattering angle at 320 K. A field of 9.5 T was applied, the wavelength employed was 0.84Å. The data are normalised to the number of iron atoms within a unit cell.

scale factor between the structure factor measured at the (111) reflection and the total magnetic moment was obtained using the reflection measurements at 260 K and 320 K to be  $x_{260K} = 1.602298$  and  $x_{320K} = 1.71255$  respectively. The values of the structure factor at the (111) reciprocal lattice point were then multiplied by these factors to obtain a total moment versus temperature curve. Both curves are shown in fig. 6.11. As the scale factor varies with temperature the true curve will lie in between the curves obtained, being closer to the lower curve for lower temperatures and closer to the upper curve for higher temperatures.

It should be pointed out that the sample used to obtain the total magnetic moment in the SQUID measurements was proven to undergo a martensitic transformation while the sample used in the neutron diffraction measurements did not. The curves show that the magnetic moment obtained using the single crystalline sample decreases more rapidly with temperature than the moment obtained in

T	$\mu_{\text{neut}}$	$[\mu_B/\text{Fe atom}]$	$\mu_{\text{SQUID}}$	$[\mu_B/\text{Fe atom}]$
260 K	5.02		4.519	
320 K	4.23		4.190	

Table 6.1: Total magnetic moment obtained of the magnetic scattering in forward direction

The magnetic moment obtained using the SQUID measurements are given for comparison. The values are normalised to the number of Fe-atoms per unit cell.

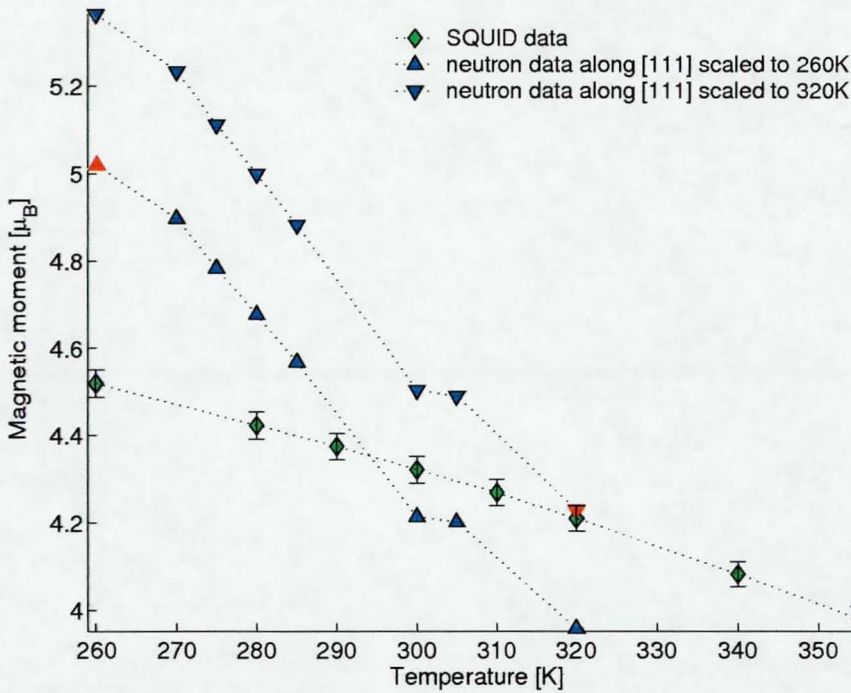


Figure 6.11: Magnetic moment in at the (111) reciprocal lattice point, compared with the data for the total moment determined in the SQUID measurements (sec. 5). The magnetic moment for the (111) reflection was scaled to the total magnetic moment using the reflection data for 260 K and 320 K respectively, thus the two curves shown in this picture. The data points at 260 K (for the lower curve) and 320 K (for the upper curve) match the total moment obtained in the reflection measurements. The red points denote the experimental data gained out of the reflection measurements at a fixed temperature.

SQUID measurements. Possible explanations for this behaviour will be discussed in chapter 8, but it is not possible to assign this difference to a particular influence.

# Chapter 7

## X-ray Diffraction Measurements

### 7.1 Introduction

Powder X-ray diffraction measurements are a powerful method to investigate the structure of a crystalline sample. The method is based on the Bragg-principle which states that elastic reflection occurs when the wavelength of the incident beam is proportional to the spacing between the lattice planes  $d$  times  $\sin(\theta)$ .

**Bragg equation in real space**

$$n \cdot \lambda = 2d \cdot \sin(\theta)$$

where

(7.1)

$n$  an integer,  $\lambda$  the wavelength of the incident beam,  $\theta$  the scattering angle and  $d$  the spacing between a set of parallel lattice planes. For the powder diffraction method a monochromatic beam is employed, so that the wavelength in the Bragg equation is kept constant. The sample is a powder and the grains are randomly oriented. The incident beam and the detector are rotated to obtain the intensities for a spectrum of scattering angles  $\theta$ . An intensity spectrum is obtained which shows peaks for sets of lattice planes at certain scattering angles. The next step is to index the peaks in the patterns. The position and intensity of the peaks gives valuable information about the structure of a sample.

In this thesis X-ray powder diffraction has been employed to investigate the structure of  $\text{Fe}_7\text{Pd}_3$  samples at different temperatures.

## 7.2 Theoretical Background

### 7.2.1 Laue-equation

The Bragg condition can be expressed in reciprocal lattice space ("k-space") and is then known as the Laue-condition:

$$\mathbf{k}' = \mathbf{k} + \mathbf{K} \quad (7.2)$$

where  $\mathbf{k}$  is the wave vector of the incident beam,  $\mathbf{k}'$  the wave vector of the scattered beam and  $\mathbf{K} = h\mathbf{b}_1 + k\mathbf{b}_2 + l\mathbf{b}_3$  is a reciprocal lattice vector. The reciprocal lattice is defined over the lattice vectors  $\mathbf{b}_i$  with  $\mathbf{b}_i \cdot \mathbf{a}_i = 2\pi$  and a volume per unit cell  $\frac{(2\pi)^3}{V_0}$  ( $V_0$  is the Volume of the unit cell in real space).

To determine the intensity of a small single crystal the Fresnel-theory can be employed. Scattering is assumed to occur in the following manner. The incident beam is absorbed by the scattering atom which then emits the scattered beam as a spherical wave. Diffraction then occurs because the spherical waves of each atom interfere with each other. It is further assumed that the distance between source S, observed point P and the crystal atoms  $\mathbf{r}_j$ ,  $\mathbf{r}'_j$  respectively is large compared to the dimensions of the crystal. The resulting wave function at P can then be written as

$$\Psi = Ae^{-i\omega t} \sum_{j=1}^N e^{ik(\mathbf{r}_j + \mathbf{r}'_j)} \quad (7.3)$$

Using the position coordinates of the atomic scatters approximate expressions for  $r_j$  and  $r'_j$  can be found.

$$\begin{aligned} r_j &= r'_0 + \mathbf{R}_j \cdot \mathbf{e}_k \\ r'_j &= r'_0 + \mathbf{R}_j \cdot \mathbf{e}_{k'} \end{aligned} \quad (7.4)$$

Equation 7.3 can then be rewritten as

$$\Psi = Ae^{i(k(r_0+r'_0)-\omega t)} \sum_j e^{ik\Delta(R_j)} = \Psi_0 \sum_j e^{ik\Delta(R_j)} \quad (7.5)$$

$\Delta(R_j)$  expresses the path difference which depends on atomic lattice coordinates only.

$$\Delta(R_j) = -\mathbf{R}_j \cdot \mathbf{e}_k + \mathbf{R}_j \cdot \mathbf{e}_{k'} = \mathbf{R}_j(\mathbf{e}_{k'} - \mathbf{e}_k) \quad (7.6)$$

Considering 7.6 the phase shift  $k\Delta(R_j)$  can be transformed to

$$k\Delta(R_j) = \mathbf{R}_j(\mathbf{k}' - \mathbf{k}) = \mathbf{R}_j\Delta\mathbf{k} \quad (7.7)$$

where the difference  $\Delta\mathbf{k}$  is usually called the scattering vector.  $\mathbf{R}_j$  represents the atomic positions in lattice coordinates and is therefore of the following form

$$\mathbf{R}_j = p_j\mathbf{a}_1 + q_j\mathbf{a}_2 + s_j\mathbf{a}_3 \quad (7.8)$$

where  $p_j$ ,  $q_j$  and  $r_j$  are integers. If  $R_j$  is substituted in the diffraction equation and the sum over  $j$  is replaced by the sums over  $p_j$ ,  $q_j$  and  $s_j$ , 7.3 becomes

$$\Psi = \Psi_0 \sum_{p_j, q_j, s_j} e^{i(p_j\mathbf{a}_1 + q_j\mathbf{a}_2 + s_j\mathbf{a}_3)\Delta\mathbf{k}} \quad (7.9)$$

with  $\psi_0 = Ae^{-i\omega t}$ . The sums on the right hand site can be transformed to

$$\sum_{p_j=0}^{P-1} \left( e^{ia_1\Delta\mathbf{k}} \right)^{p_j} = \frac{1 - e^{iPa_1\Delta\mathbf{k}}}{1 - e^{ia_1\Delta\mathbf{k}}} = \frac{e^{iPa_1\Delta\mathbf{k}/2} \sin(P\mathbf{a}_1\Delta\mathbf{k})}{e^{ia_1\Delta\mathbf{k}/2} \sin(\mathbf{a}_1\Delta\mathbf{k})} \quad (7.10)$$

Then the intensity distribution of the diffraction pattern can be written as

$$I = |\Psi|^2 = I_0 \frac{\sin(P\mathbf{a}_1\Delta\mathbf{k}/2)}{\sin^2(\mathbf{a}_1\Delta\mathbf{k})} \frac{\sin(Q\mathbf{a}_2\Delta\mathbf{k}/2)}{\sin^2(\mathbf{a}_2\Delta\mathbf{k})} \frac{\sin(S\mathbf{a}_3\Delta\mathbf{k}/2)}{\sin^2(\mathbf{a}_3\Delta\mathbf{k})} \quad (7.11)$$

Maxima can be found where the numerators and denominators tend towards zero, that is

$$a_1 \Delta k = 2\pi h \quad a_2 \Delta k = 2\pi k \quad a_3 \Delta k = 2\pi l \quad (7.12)$$

Each of these conditions can be multiplied by an arbitrary integer. The following equation can then be obtained for maximum intensity

$$(ra_1 + qa_2 + sa_3) \Delta k = \mathbf{R} \cdot \Delta \mathbf{k} = 2\pi(ph + qk + sl) \quad (7.13)$$

This conditions shows that diffraction maxima can only occur if the scattering vector is a reciprocal lattice vector:

$$\Delta \mathbf{k} = \mathbf{K}_{hkl} = hb_1 + kb_2 + lb_3 \quad (7.14)$$

which is the well known Laue-equation. Assuming that the scattering angle between the incident and the diffracted beam is  $2\theta$  it can be rewritten in real space:

$$|\Delta \mathbf{k}| = 2k \sin \theta = |\mathbf{K}_{hkl}| = \frac{2\pi}{d_{hkl}} \quad (7.15)$$

A Geometric approach to equation 7.14 is given by the Ewald sphere.  $\mathbf{k}$  is drawn for the reciprocal lattice terminating at the origin. A sphere with radius  $|\mathbf{k}|$  is then drawn with the centre at the starting point of the incident wave vector. If the sphere now intersects with any other point of the reciprocal lattice, constructive interference will be observed.

## 7.2.2 Structure Factors for Bragg-reflections

The scattering of X-rays by electrons can be expressed using a form factor, which modifies the intensity of the scattered wave. The form factor of a single electron can be written as

$$f_e = \int_V e^{2\pi i \Delta \mathbf{k} \cdot \mathbf{r}} \rho dV \quad (7.16)$$

It is basically the Fourier transform of the electron distribution  $\rho$ . A system of several electrons is then represented by the sum of the different electron contributions:

$$f = \sum_N f_N \quad (7.17)$$

However, the evaluation of the integral can become complicated for real atoms with a non-spherical electron distribution.

Additionally, for a crystal the diffraction pattern is of course strongly dependent on the actual structure of the crystal, namely the atomic positions. Their influence on the diffracted intensity is represented by the structure factor. The structure factor is not only a function of the elements involved, but also depends on the actual structure:

$$F = \sum_n f_n e^{2\pi i \Delta k r_n} \quad (7.18)$$

where  $F$  is the structure factor,  $f_n$  the atomic form factors of the elements involved and  $r_n$  the atomic position in lattice coordinates within the unit cell. The diffracted intensity will then be proportional to the square of the structure factor  $I \sim F^2$ . Therefore, if the structure factor is zero for a certain reflection the intensity for this reflection will also be zero. Because of that, missing reflections give important information about the structure of a sample, an example for this is the face centred cubic f.c.c. structure.

### Structure Factor for an f.c.c. Lattice

In a f.c.c. structured lattice for each atom with coordinates  $\mathbf{a}_1, \mathbf{a}_2, \mathbf{a}_3$  there must be identical atoms with coordinates  $\mathbf{a}_1 + \frac{1}{2}, \mathbf{a}_2 + \frac{1}{2}, \mathbf{a}_3$ ;  $\mathbf{a}_1 + \frac{1}{2}, \mathbf{a}_2, \mathbf{a}_3 + \frac{1}{2}$  and  $\mathbf{a}_1, \mathbf{a}_2 + \frac{1}{2}, \mathbf{a}_3 + \frac{1}{2}$  with identical form factors. If the unit cell contains  $N$  atoms, the atoms can be divided into  $N/4$  groups of 4 identical atoms and structure factor then becomes:

$$F = \sum_{N/4} f_n [ e^{2\pi i(hp_n+kq_n+ls_n)} + e^{2\pi i(h(p_n+1/2)+k(q_n+1/2)+ls_n)} +$$

$$\begin{aligned}
& e^{2\pi i(h(p_n+1/2)+kq_n+l(s_n+1/2))} + e^{2\pi i(hp_n+k(q_n+1/2)+l(s_n+1/2))} ] \\
= & \left[ 1 + e^{\pi i(h+k)} + e^{\pi i(h+l)} + e^{\pi i(k+l)} \right] \sum_{N/4} f_n e^{2\pi i(hp_n+kq_n+ls_n)} \quad (7.19)
\end{aligned}$$

Since  $e^{i\pi m} = (-1)^m$  and  $hkl$  are all integer numbers, it can be seen that the structure factor becomes

$$F_{hkl} = 4 \sum_{N/4} f_n e^{2\pi i(hp_n+kq_n+ls_n)} \quad hkl \text{ all odd or all even} \quad (7.20)$$

$$F_{hkl} = 0 \quad hkl \text{ mixed} \quad (7.21)$$

Which means that a f.c.c. sample will give a diffraction pattern where the indices  $hkl$  of the planes corresponding to the diffraction peaks will be either all odd or all even but never mixed.

### 7.2.3 Spacing Formula

It remains to evaluate the relationship between the spacing between parallel lattice planes  $d$  and the corresponding  $hkl$ -planes.

$$\frac{1}{d_{hkl}^2} = |\mathbf{H}_{hkl}|^2 = (h\mathbf{b}_1 + k\mathbf{b}_2 + l\mathbf{b}_3)(h\mathbf{b}_1 + k\mathbf{b}_2 + l\mathbf{b}_3) \quad (7.22)$$

using that  $\mathbf{b}_i = \frac{\mathbf{a}_j \times \mathbf{a}_k}{\mathbf{a}_1 \cdot \mathbf{a}_2 \times \mathbf{a}_3}$  and relations provided by vector analysis, the spacing formula can be written in terms of the lattice vectors and the angles between them, providing the spacing formula for a triclinic crystal. The equation gets considerably less complicated for a crystal with a higher symmetry. For example the spacing formula for a cubic crystal with  $a = b = c$ ,  $\alpha = \beta = \gamma = 90^\circ$  becomes

**cubic structure**

$$\frac{1}{d_{hkl}^2} = \frac{h^2 + k^2 + l^2}{a^2} \quad (7.23)$$

and for a tetragonal crystal structure with  $a = b$ ,  $\alpha = \beta = \gamma = 90^\circ$  the spacing formula reads

tetragonal structure

$$\frac{1}{d_{hkl}^2} = \frac{h^2 + k^2}{a^2} + \frac{l^2}{c^2} \quad (7.24)$$

Substituting the spacing formulae into the Bragg-equation it is possible to index a diffraction pattern, assigning hkl-values to the observed peaks at certain angles. It can be seen for cubic crystals, that for equivalent sets of hkl-values, like {200}, {020} and {002}, the angle  $\theta$  is the same in the Bragg-equation, which means that they will appear in the same position in a diffraction pattern.

However, for a tetragonal structure this will not be the case. h and k values will still be equivalent but l values will not, therefore indices like {200} and {020} will result in peaks at the same position but the peak with index {002} will appear at a different  $2\theta$  value. So peaks which coincide in a cubic structure will split into two in a tetragonal structure. In general it can be said that when a structure exhibits less symmetry more peaks will appear in the diffraction pattern and the structure becomes considerably more complicated.

## 7.3 Experimental Procedure

### 7.3.1 The Powder Diffractometer

For the X-ray investigation X-rays of a single wavelength hit the target powder at a certain incident angle  $\theta$  and the scattered X-ray intensity gets analysed at the same angle  $\theta$ . The scattering angle between incident and diffracted beam is therefore  $2\theta$ . The sample as well as the detector is then rotated during the measurement to scan through a range of scattering angles  $2\theta$ .

The device employed generated X-rays using a copper cathode. Fast electrons hit a copper target and, interacting with the electromagnetic potential of the copper atoms, decelerate quickly emitting continuous Bremsstrahlung in the X-ray spectrum. If the electron energy is high enough, the accelerated electrons

can hit electrons from the inner shells out of copper atoms. The remaining electron will fill the whole with electrons of the outer shells of the atoms. As they undergo a transition to a state of lower energy, radiation of a sharp characteristic wavelength dependent on the energy difference between the two states is emitted. This radiation can be seen as sharp, intense lines superimposed on the cathode spectrum. For the diffractometer used, the wavelength employed was the copper  $K_{\alpha}$ -line. This is related to an electron of the L-shell (with quantum number  $n=2$ ) which fills hole of the K-shell (with quantum number  $n=1$ ). However, considering the influence of other quantum numbers there will be two  $K_{\alpha}$  lines. The  $K_{\alpha_1}$  with  $\lambda = 1.541\text{\AA}$  line is used for the experiments.

The X-rays generated in a copper cathode hit the target powder, which is placed on an open metal sample holder in the sample chamber. They then get through a tube and hit an graphite analyser, which reflects the  $K_{\alpha_1}$ -line, using the Bragg equation again, onto an X-ray detector. The analyser-detector system as well as the sample holder are rotated to allow to scan through a range of scattering angles from  $15^{\circ}$  to  $85^{\circ}$ .

During the measurements the detector and sample holder get rotated and the intensity of the radiation is measured over a certain time, using computer control.

The sample was cooled by pumping cold nitrogen gas through the sample chamber. On the sample holder a heating device and a temperature sensor were fixed. These were connected to a temperature controller (Oxford ITC 503). The temperature control was achieved by controlling the heating power. This was carried out automatically by the temperature controller. Before each measurement was started a minimum time of 20 min. was allowed for reaching thermal equilibrium.

### 7.3.2 Indexing the diffraction patterns

The diffraction pattern recorded during an X-ray powder diffraction experiment shows intensity over scattering angle. As described before the recorded peaks belong each to a set of lattice planes ( $hkl$ ). To assign each peak to indices  $hkl$ , the Bragg equation in combination with equation 7.23 is used. The peaks are assigned correctly to a set of lattice planes, if the lattice parameters obtained for each reflection are identical.  $Fe_7Pd_3$  exhibits a f.c.c. structure at higher temperatures. As was shown above, for an f.c.c. lattice only those reflections will occur which have either all odd or all even miller indices. The first reflection which can be found will therefore be an (111) reflection.

If the lattice is of lower symmetry or an additional phase occurs the peaks in the pattern will split up and the indexing of the pattern becomes considerably more complicated. For an f.c.t. lattice the cubic peaks will split up into two peaks, apart from the peaks with for which  $h = k = l$ , such as (111) etc..

## 7.4 Results and Analysis

The following experiments have been carried out. First an X-ray pattern was recorded at room temperature (295K), afterwards the sample was cooled down to record a low temperature pattern at 260K. Then the sample was heated up again to 282K which is approximately the transition temperature of the prepared sample, according to the resistivity measurements which have been carried out (see chapter 4).

As described in section 3.3 the powder manufacture was very difficult due to the high ductility of the material. Because of the necessity to powder the alloy employing a file, only relatively large grains could be obtained. The powdering process destroyed the internal structure of the sample. The sample had to be heat treated again which resulted in the powder sintering together again due to

softening of the material during the heat treatment. Finally the powder grains were obtained by carefully scraping off powder grains from the heat treated bulk powder with a metal needle. During this procedure considerable stress had to be applied to separate the grains. For this reasons it was only possible to obtain a limited quantity of powder with a relatively large grain size. In addition the stress which had to be applied on the grains in order to separate them might have led to distortions of the structure within the grains. The effect of the large grain size on the intensity pattern can be seen by comparing the intensities of the different patterns as stated below. It can be seen, that the large grain size and possible other effects, such as stress induced distortions, strongly influence the intensity pattern obtained. Furthermore, the intensity pattern is likely to be influenced by absorption effects in the experimental arrangement. This effects will be different for each peak as each peak is recorded at a different scattering angle. Therefore the obtained peak patterns are strongly effected by influences which are not caused by the structure of the sample and the refinement was very difficult due to these influences. Unfortunately the difficulty in obtaining the powder made it not possible to gain better data. The difficulties in refinement due to the powder quality also account for the large differences in the lattice parameters obtained with the different samples. The refinement routine aims to subtract a shift in the pattern resulting from the experimental conditions, because of the strong external influences the shift determined for the two samples was different and that influenced the obtained lattice parameters. Nevertheless a peak splitting could be observed and the peaks could be indexed considering a disordered f.c.c. high temperature phase and a disordered f.c.t. low temperature phase.

The high temperature pattern was then indexed as described above. The peaks belonging to the sample correspond to (111), (200) and (220) reflections. Only peaks with either all odd or all even indices could be observed. A split of the (200) and (220) peaks for lower temperatures was observed. The three peaks in the patterns labelled 'Cu' correspond to reflections of the copper sample holder.

Table 7.1: Lattice parameter at different temperatures obtained from X-ray powder diffraction.

Temperature [K]	Lattice parameter [Å]		
	a	c	
295	3.763		cubic
260	3.781	3.753	tetragonal
282	3.812		cubic
282	3.853	3.850	tetragonal

To verify this a diffraction pattern of the empty sample holder was compared with the measurements. Additionally X-ray diffraction patterns were recorded at room temperature, using other sample holders made of Al and Brass. The comparison of all these patterns clearly identified the additional peaks as belonging to the sample holder. Finally, the refinement showed good agreement with the observed peaks, when a copper phase was assumed to represent the sample holder. As can be seen from the refined patterns fig. 7.1, fig. 7.2 and fig. 7.3, the copper peaks dominate the recorded pattern. The reflections caused by the sample are weak compared to the signal from the copper holder.

The pattern was refined using the Retvield method in the computer program 'Fullprof', an f.c.c. structure with space group  $Fm\bar{3}m$  for the high temperature phase and an f.c.t. structure using the the space group  $F4/mmm$  for the low temperature phase were used to refine the recorded data. It was assumed that the sample is disordered in both phases. Fig. 7.1 shows the refined pattern for the 295K measurement. Fig. 7.2 and fig. 7.3 show the refined patterns for the 260 K and the 282 K measurements respectively. The lattice parameter obtained by the refinement are shown in tab. 7.1. The .pcr files used for the refinements are shown in the appendix.

Only peaks with either all odd or all even indices could be observed in the high temperature phase. In addition, all observed peaks were single peaks. This shows

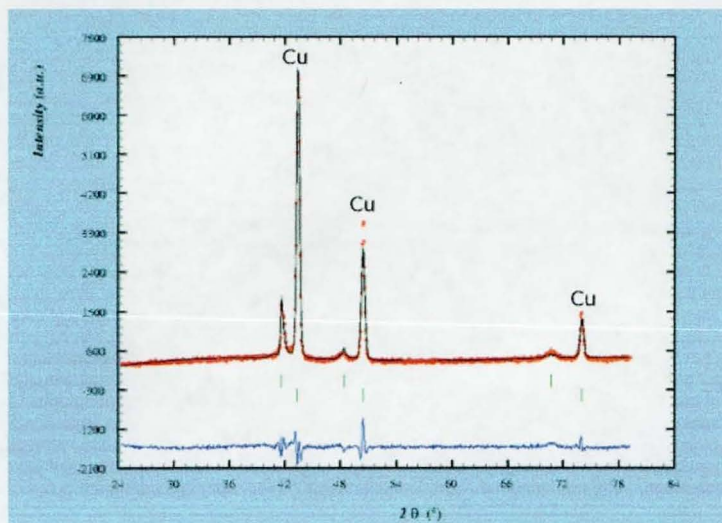


Figure 7.1: Refined X-ray diffraction pattern at 295 K. The peaks belonging to the second phase (peak no 2, 4 and 6) are caused by the copper sample holder. The peaks in the first phase correspond to the  $\text{Fe}_7\text{Pd}_3$  sample and belong to (111), (200) and (220) reflections.

that the investigated structure is a face centred cubic one. At low temperatures the peaks corresponding to (200) and (220) are found to be split into two peaks and the original peaks of the high temperature phase can not be observed any longer. Therefore the investigated structure is tetragonal. No peaks appeared or disappeared, just a splitting was observed. The low temperature pattern therefore shows a face centred tetragonal (f.c.t.) structure. However, the splitting observed was very small and the peaks of weak intensity. Examining the split peaks of the (200) and (220) reflections, it was found, that the first peak of the (200) reflections was of higher intensity than the second one. In contrast, in the (220) reflections the second peak had a larger intensity compared to the first one. This can be explained considering that the (200) and (020) planes give rise to reflections at the same scattering angle  $\theta$ , while the (002) reflection will scatter at a different angle in a tetragonal phase. Therefore twice the amount of plane sets scatter in one peak compared to the other. That the peak with higher intensity has a lower scattering angle shows, that the two identical axes in the unit cell ('a-axes') have a larger lattice parameter than the other axis ('c-axis'). The ratio  $c/a$  is therefore smaller than 1. The similar considerations apply for the (220) reflections.

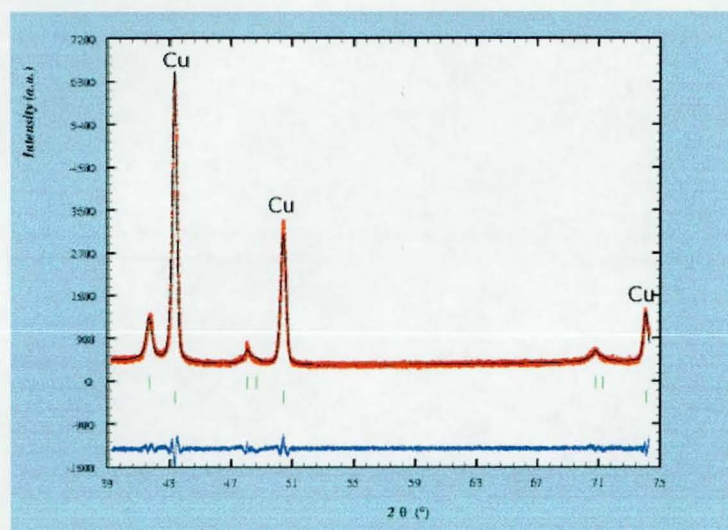


Figure 7.2: Refined X-ray diffraction pattern at 260 K. The peaks in the first phase belong to the (111), the (200) and the (220) reflections of the  $\text{Fe}_7\text{Pd}_3$  sample.

In the pattern recorded at 282 K the tetragonal phase could be observed as well, but in addition the high temperature cubic phase could be identified. Additionally two very small peaks appeared between  $45^\circ$  and  $46^\circ$  ( $2\theta$ ).

Moreover, the intermediate temperature pattern shows a different intensity distribution than the other two. Especially the tetragonal (200) reflections are of much higher intensity compared to the other patterns recorded. For the measurement at 282 K another sample had to be used, because the sample used for the 260 K and 295 K measurements was accidentally cooled down to low temperatures due to a power failure. The difference in intensity can be explained assuming that the lattice planes are not entirely evenly distributed. Thus more planes were oriented in a way that they could contribute in particular to the (200) reflections in the second sample. Considering that the grain size of the powder obtained was indeed very large, this explanation seems reasonable.

The diffraction measurements show a transformation from f.c.c. to f.c.t. structure as expected. The transition temperature from martensite to austenite lies around 282 K. The use of two powder samples also showed that the orientation of the grains influenced the intensities recorded. However, the difficulties in ob-

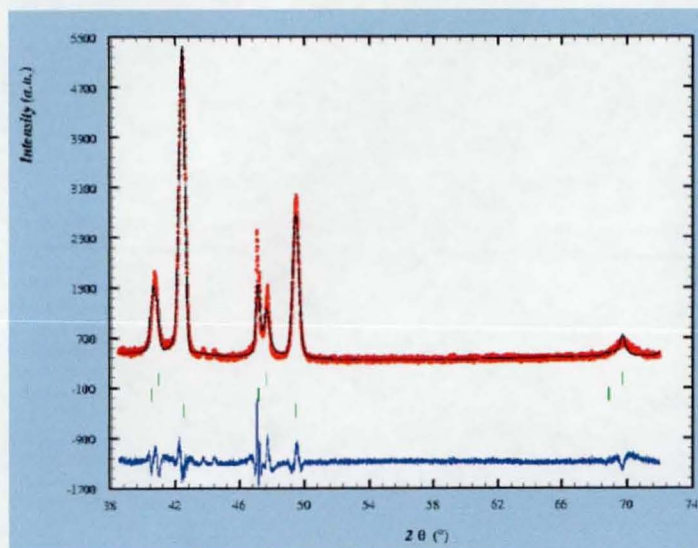


Figure 7.3: Refined X-ray diffraction pattern at 282 K. The first phase corresponds to the high temperature cubic phase. The second phase corresponds to the low temperature tetragonal phase. The third phase represents the copper sample holder. The peaks of the sample correspond to (111), (200) and (220) reflections respectively.

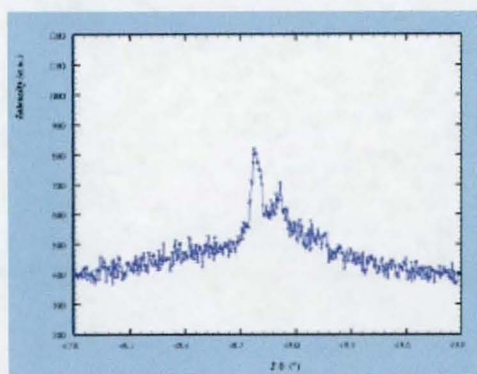


Figure 7.4: Magnified view of the peak corresponding to the (200) reflections at 260 K. It can be seen that the first peak is of higher intensity compared to the second one.

taining the powder and the fixed sample holder made it impossible to record a pattern with a more even distribution of lattice orientations.

# Chapter 8

## Discussion

A phase transition could clearly be observed in the resistivity experiments carried out. This transition was proven to be the expected f.c.c.  $\rightarrow$  f.c.t. martensitic transition by means of X-ray diffraction. The transition temperature was determined to be  $M_T = (283 \pm 1)K$ . Furthermore, proof of a second irreversible transition at lower temperatures was found in the resistivity measurements, which is in agreement with Oshima et al. [4] [6] and Foos et al. [11], who found that a irreversible phase transition from f.c.t. to b.c.t. takes place at lower temperatures for  $Fe_{1-x}Pd_x$  alloys with  $0.295 < x < 0.30$ .

The results obtained in the resistivity experiments contradict the observations made by Matsui et al. [12] and Oshima et al. [6], who state that no change in resistivity was found during the phase transition.

The resistivity measurements did not show a significant hysteresis between heating and cooling measurements. However, the magnetisation experiments did show a large hysteresis. This might be explained assuming that the resistivity and the magnetisation measurements are sensitive to different effects within the sample, which cause different hysteresis.

The resistivity measurements confirm further that heat treatment, rapid quenching from high temperatures, is necessary to observe the phase transformation.

This is the expected behaviour, because the austenite phase concerned is the high temperature ( $\gamma$ Fe,Pd) phase, which is only stable at high temperatures for the palladium concentration concerned. This result further agrees with all publications found, apart from Cui et al. [26] who found, that heat treatment is not necessary to induce a phase transition. X-ray diffraction confirmed the structure of the sample to be disordered f.c.c. above the transition and disordered f.c.t. below the transition temperature.

The magnetisation experiments carried out with the polycrystalline sample do not exhibit an obvious transition. The magnetisation seems to form a broad peak around 278 K (302 K) but the increase is only of the order of 2%. Moreover, cooling to low temperatures showed that this peak like behaviour continued down to temperatures of about 50 K. It is possible that the observed increase in magnetisation with rising temperature is due to the f.c.c.  $\rightarrow$  f.c.t. phase transition since the maximum magnetisation occurs in a temperature range close to the transition temperature observed in the X-ray and resistivity measurements. Matsui et al. [12] state that the alloy does not exhibit unusual magnetisation behaviour over the transition temperature. They investigated the magnetisation as a function of temperature at high fields. Their results agree with the observations made here. The increase in magnetisation with rising temperature was only observed at low fields. The magnetic moment determined using the SQUID magnetometer did not show an unusual behaviour with increasing temperature. It was shown, that the magnetic moment exhibits a similar temperature behaviour as the magnetic moment associated with the iron atoms in  $\text{Fe}_{65}\text{Ni}_{35}$ , if it is assumed that only the iron atoms contribute to the magnetic moment in  $\text{Fe}_7\text{Pd}_3$ .

In contrast to the polycrystalline samples, the single crystalline samples which were investigated did not exhibit a structural phase transition although repeated heat treatment was applied in the same manner as to the polycrystalline samples. Single crystal diffractometry proved, that the crystals exhibit the high temperature f.c.c. phase, with a lattice parameter close to the expected one. A possible

explanation for this behaviour would be, that the palladium concentration in the single crystalline samples was not in the required concentration range. As can be seen in the Fe-Pd phase diagram fig. 2.2, the f.c.c. high temperature phase is stable for the whole concentration range of palladium. So if palladium concentration is not in the range between 29.5% - 33% (atomic percent), the crystal would exhibit the f.c.c. phase after sufficient heat treatment, but would not transform to f.c.t.. For palladium concentrations little above 33% no phase transition has been observed so far. In a concentration range of 27% - 29.5% (Pd atomic concentration) the alloy would be at least partly transformed to b.c.t. at room temperature. At lower palladium concentrations the alloy transforms to b.c.c.. Oshima et al. [6] state that they found an alloy transformed to b.c.c. at room temperature with a palladium concentration around 25% atomic percent. (see section 2.0.1). A change in the structure of the sample was found at lower temperatures, but could not be assigned with any particular transition. It might therefore be possible that the palladium concentration of the single crystals is slightly higher than 33%, assuming that the peak broadening at lower temperatures is not a sign of a structural phase transition.

Nevertheless, the high temperature f.c.c. phase remains stable over a wide concentration range and its magnetic properties were studied by means of polarised neutron diffraction. The results show that the magnetic form factor is isotropic at the different lattice sites. The form factor for each lattice site is identical because of the disordered nature of the structure.

The total magnetic moment determined out of the polarised neutron experiments is larger by  $0.501 \mu_B / (\text{Fe-atoms in unit cell})$  for 260 K and coincides with the magnetic moment obtained in the bulk measurements at 320 K.

The magnetic moment versus temperature curves both decrease continuously with rising temperature. However, the magnetic moment at the [111] reflection obtained with polarised neutrons decreases more rapidly with rising temperature.

An explanation for the differing magnetic moments at low temperatures is,

that the two examined samples have different structures at these temperatures. The f.c.t. phase would possess a smaller magnetic moment than the f.c.c. phase at the same temperature. At 320 K, where both samples exhibit the same structure the magnetic moment obtained in the reflection measurements coincides with the one obtained in the magnetometer measurements. However, the curve of the moment at the (111) reciprocal lattice point seems to rise quicker already at temperatures where both samples still have the same structure, see fig. 6.11. Another possible explanation is that the magnetic moment is not only located at the iron atoms. Palladium can be polarised in a strong magnetic field, such as the strong molecular field given in an iron environment, and then give rise to a ferromagnetic contribution. The magnetic form factor of palladium drops very quickly with rising scattering angle. As the magnetic form factor is the Fourier transform of the magnetisation distribution, this gives rise to a magnetisation distribution, which is essentially flat. In the fits made a constant magnetisation contribution was not assumed, and the extrapolation made to obtain the total magnetic moment would give differing results to the SQUID measurements if a constant magnetisation is present. However, the variation of the constant magnetisation with temperature must be very large to account for the difference of  $0.501\mu_B$  within the investigated temperature range and comparison of the SQUID data for  $\text{Fe}_7\text{Pd}_3$  with the magnetic moment on iron in  $\text{Fe}_{65}\text{Ni}_{35}$  showed good agreement if it was assumed that the magnetic moment in  $\text{Fe}_7\text{Pd}_3$  is caused by the iron atoms only. It is not possible to ascribe the observed difference in the temperature dependence of the magnetic moment to a particular influence with the data obtained.

A measurement of the magnetisation over temperature with a small applied field (0.1 T) of a single crystalline sample showed also a significantly larger temperature dependence, than the polycrystalline sample showed under the same conditions.

The properties of  $\text{Fe}_7\text{Pd}_3$  are somewhat difficult to explore because of the disordered nature of the sample and the strong concentration dependence of the

phase transition. Nevertheless,  $\text{Fe}_7\text{Pd}_3$  is still subject of many studies.

It would be desirable to study the magnetic structure factor for the f.c.t. phase and repeat the measurements of the f.c.c. phase to check upon the differences observed in the results of the magnetic moment for the single crystalline and polycrystalline samples.

In addition it is of interest to carry out further investigations of the relationship between the Invar behaviour and the structural phase transition, since the Invar behaviour does not continue into the f.c.t. region.

Although many investigations concerning  $\text{Fe}_7\text{Pd}_3$  were carried out, the mechanism of the phase transition and its connection to its other properties such as Invar behaviour and shape memory effect are still not well understood. Further investigations will be needed which focus on this aspects.

To obtain accurate results, it will be essentially to prove the exact concentration of the samples used in further investigations.

# Bibliography

- [1] W.B. Pearson: A Handbook of Lattice Spacing and Structures of Metals and Alloys, Pergamon Press, **2**, (1967)
- [2] Binary Alloy Phase Diagrams: American Society of Metals; **1**, T. B. Massalski, J. L. Murray, L. H. Bennett, H. Baker (editors), (1986)
- [3] T. Sohmura, R. Oshima, F. Fujita: Thermoelastic FCC-FCT Martensitic Transformation in Fe-Pd Alloy, Scripta Metallurgica, **14**, (1980), 855-856
- [4] R. Oshima: Successive martensitic transformations in Fe-Pd alloys, Scripta Metallurgica, **15**, (1981), 829-833
- [5] R. Oshima, M. Sugiyama: Martensitic Transformations in Fe-Pd Alloys, Journal de Physique, **C4-12**, (1982), 383-388
- [6] M. Sugiyama, R. Oshima, F. Fujita: Martensitic Transformation in the Fe-Pd Alloy System, Transactions of the Japan Institute of Metals, **25-9**, (1984), 719-730
- [7] M. Sugiyama, S. Harada, R. Oshima: Change in Young's modulus of thermoelastic martensite Fe-Pd Alloys, Scripta Metallurgica, **19**, (1985), 315-317
- [8] M. Sugiyama, R. Oshima, F. Fujita: Mechanism of fcc-fct Thermoelastic Martensite Transformation in Fe-Pd Alloys; Transactions of the Japan Institute of Metals, **27-10**, (1986), 719-730

- [9] S. Muto, R. Oshima, F. E. Fujita: Relation of Magnetic Domain Structure to F.C.T. Martensite Variants in Fe-Pd Alloys, *Scripta Metallurgica*, **21**, (1987), 465-468
- [10] S. Muto, R. Oshima, F. E. Fujita: Elastic softening and elastic strain energy consideration in the f.c.c.-f.c.t. transformation of Fe-Pd alloys, *Acta metall. mater.*, **38-4**, (1990), 684-694
- [11] M. Foos, C. Frantz, M. Gantois: Structural changes in invar iron-palladium alloys before the f.c.c.- b.c.t. martensite transformation, *Journal de Physique*, **C4-12**, (1982), 389-394
- [12] M. Matsui, H. Yamada, K. Adachi: A New Low Temperature Phase (fct) of Fe-Pd Invar, *J. Phys. Soc. Japan*, **48-6**, (1980), 2161-2162
- [13] M. Matsui, T. Shimizu, H. Yamada, K. Adachi: Magnetic Properties and Thermal Expansion of Fe-Pd Invar Alloys, *Journal of Magnetism and Magnetic Materials*, **15-18**, (1980), 1201-1202
- [14] M. Matsui, K. Adachi: Magnetostriction of Fe-Pd Invar, *Journal of Magnetism and Magnetic Materials*, **31-34**, (1983), 115-116
- [15] M. Matsui, J. P. Kuang, T. Totani, K. Adachi: Magnetic Anisotropy of FePd Invar Alloys, *Journal of Magnetism and Magnetic Materials*, **54-57**, 911-912
- [16] A. Kussmann, K. Jessen: Invar-Behaviour and Magnetic Moments of the  $\gamma$ -Phase of Iron-Palladium Alloys, *Journal of the Physical Society of Japan*, **17/B-I**, (1962), 136-139
- [17] T. Nakayama, M. Kikuchi, K. Fukamichi: Linear Magnetostriction And Elastic Properties Of Fe-Pd Alloy Systems, *IEEE Transactions on Magnetics*, **MAG-15-5**, (1980), 1071-1073

- [18] T. Nakayama, M. Kikuchi, K. Fukamichi: Young's modulus and the  $\Delta E$  effect of Fe-Pd Invar alloys: *J. Phys. F: Metal Phys.*, **10**, (1980), 715-719
- [19] T. Kubota, T. Okazaki, Y. Furuya, T. Watanabe: Large magnetostriction in rapid-solidified ferromagnetic shape memory Fe-Pd alloy, *Journal of Magnetism and Magnetic Materials*, **239**, (2002), 551-553
- [20] M. Sato, B. H. Grier, S. M. Shapiro, H. Miyajima: Effect of magnetic ordering on the lattice dynamics of FCC  $\text{Fe}_{1-x}\text{Pd}_x$ , *J. Phys. F: Metal Phys.*, **12**, (1982), 2117-2129
- [21] D. Vokoun, C. T. Hu: Improvement of shape memory characteristics in Fe-Pd melt-spun shape memory ribbons, *Journal of Alloys and Compounds*, **346**, (2002), 147-153
- [22] D. Vokoun, C. T. Hu, V. Kafka: Magnetic properties of annealed Fe-29.9at%Pd ribbons, *Journal of Magnetism and Magnetic Materials*, **264**, (2003), 169-174
- [23] J. Cui, R. D. James: Study of  $\text{Fe}_3\text{Pd}$  and Related Alloys for Ferromagnetic Shape Memory, *IEEE Transactions on Magnetics*, **37-4**, (2001), 2675-2677
- [24] R. A. Stern, S. D. Willoughby, A. Ramirez, J. M. MacLaren, J. Cui, Q. Pan, R. D. James: Electronic and structural properties of  $\text{Fe}_3\text{Pd}$ -Pt ferromagnetic shape memory alloys, *Journal of Applied Physics*, **91-10**, (2002), 7818-7820
- [25] R. A. Stern, S. D. Willoughby, J. M. MacLaren, J. Cui, R. D. James:  $\text{Fe}_3\text{Pd}$  ferromagnetic shape memory alloys, *Journal of Applied Physics*, **93-10**, (2003), 8644-8646
- [26] J. Cui, T. W. Shield, R. D. James: Phase transformation and magnetic anisotropy of an iron-palladium ferromagnetic shape memory alloy, *Acta materialia*, **52**, (2004), 35-47

- [27] T. Sakamoto, T. Fukuda, T. Kakeshita, T. Takeuchi, K. Kishio: Influence of Magnetic Field Direction on Rearrangement of Martensite Variants in an Fe-Pd Alloy, *Materials Transactions*, **44-12**, (2003), 2495-2498
- [28] H. Kato, T. Wada, Y. Liang, T. Tagawa, M. Taya, T. Mori: Martensite structure in polycrystalline Fe-Pd, *Materials Science and Engineering*, **A332**, (2002), 134-139
- [29] S. Becker, P. J. Brown, B. Dennis, K. Fröhlich, T. Kanomata, M. Matsumoto, K.-U. Neumann, B. Ouladdiaf, J. Rasch, N.-J. Steinke, T. Stephens, O. Unverdi, K. R. A. Ziebeck: Ferromagnetic Shape Memory Compounds with a Heusler Structure, submitted for publication, INABIO feb. (2004)
- [30] G. T. Meaden: *Electrical Resistance Of Metals*, Heywood Books, (1966)
- [31] P. L. Rossiter: *The electrical resistivity of metals and alloys*, Cambridge University, (1987)
- [32] M. S. Rogalski, S. B. Palmer: *Solid state physics*, Gordon and Breach Science Publishers, (1987)
- [33] F. Brailsford: *Physical Principles of Magnetism*, D. Van Nostrand Company Ltd., (1966)
- [34] B. D. Cullity: *Introduction to Magnetic Materials*, Addison-Wesley Publishing Company, (1972)
- [35] D. Jiles: *Magnetism and Magnetic Materials*, Chapman and Hall, (1991)
- [36] K.-U. Neumann, K. R. A. Ziebeck : Heusler Alloys, Arrott plots; *Magnetic Properties of Metals*, Landault-Börnstein, **32/19-C** part 2, (H. P. J. Wijn, ed.), Springer Verlag, (2001), 95 - 113

- [37] P. J. Brown, T. Kanomata, M. Matsumoto, K-U. Neumann, K. R. A. Ziebeck: Moment instability in  $\text{Fe}_{65}\text{Ni}_{35}$  and  $\text{Fe}_3\text{Pt}$  invar alloys studied with polarised neutrons, *Journal of Magnetism and Magnetic Materials*, **242-245**, (2002), 781-787
- [38] P. J. Webster, K. R. A. Ziebeck: Ternary transition metals, *Neutron diffraction theory; Magnetic Properties of Metals*, Landault-Börnstein, **III/19-C**, (H. P. J. Wijn, edt.), Springer Verlag, (1988), 124-125
- [39] P. J. Brown, J. Deportes, K. R. A. Ziebeck: High temperature magnetisation distribution in nickel, *Journal of Physics I France*, **1**, (1991), 1529-1537
- [40] S. W. Lovesey: *Theory of Neutron Scattering from Condensed Matter Vol. 1*; Oxford Science Publications, (1987)
- [41] S. W. Lovesey: *Theory of Neutron Scattering from Condensed Matter Vol. 2*; Oxford Science Publications, (1987)
- [42] W. Marshall, S. W. Lovesey: *Theory of Thermal Neutron Scattering*; Oxford at the Clarendon Press, (1971)
- [43] M. Ladd, R. Palmer: *Structure determination by X-ray crystallography*, 4<sup>th</sup> edition, Kluwer Academic/Plenum Publishers, (2003)
- [44] N. F. M. Henry, H. Lipson, W. A. Wooster: *The interpretation of X-ray diffraction photographs*, Macmillan & Co LTD, (1960)
- [45] The Yellow Book of the ILL, section D9, <http://www.ill.fr/yellowbook/d9/>
- [46] The Yellow Book of the ILL, section D3, <http://www.ill.fr/yellowbook/d3/>
- [47] A. Rauch, W. Waschkowski: *Neutron Scattering Length*, Neutron Data Booklet, A.-J. Dianoux, Gerry Lander (Edt.), Institut Laue-Langevin, (2001)

- [48] B.E. Warren: X-ray diffraction, Addison-Wesley Publishing Company,  
(1969)

## Appendix – .pcr files

fe7pd3295K.pcr

COMM Fe7Pd3 heat treated 5d@1100C -- 295 K

! Current global chi2 (Bragg contrib.) = 3.397

! Files => DAT-file: fe7pd3r1, PCR-file: test

! Job Npr Nph Nba Nex Nsc Nor Dum Iwg Ilo Ias Res Ste Nre Cry Uni Cor Opt Aut  
 0 5 2 0 2 0 0 0 0 0 0 0 0 0 0 0 0 0 0 0

! Ipr Ppl Ioc Mat Pcr Ls1 Ls2 Ls3 NLI Prf Ins Rpa Sym Hkl Fou Sho Ana  
 0 0 1 0 1 0 0 0 0 1 0 0 0 1 2 0 0

! lambda1 Lambda2 Ratio Bkpos wdt Cthm muR AsyLim Rpolarz  
 ->Patt# 1  
 1.540562 1.540562 1.0000 40.000 30.0000 0.0000 0.5000 45.00 0.0000

! NCY Eps R\_at R\_an R\_pr R\_gl Thmin Step Thmax PSD  
 Sent0  
 7 0.01 0.08 0.08 0.08 0.08 15.0000 0.050000 85.0000 0.000  
 0.000

! Excluded regions (LowT HighT) for Pattern# 1  
 -10.00 25.00  
 80.00 180.00

20 !Number of refined parameters

! Zero Code SyCos Code SySin Code Lambda Code MORE ->Patt# 1  
 0.70008 11.00 0.00000 0.00 0.00000 0.00 0.000000 0.00 0  
 ! Background coefficients/codes for Pattern# 1  
 408.56 -89.236 -625.86 1748.9 -1018.4 0.0000  
 41.000 51.000 61.000 71.000 81.000 0.000

-----  
 ! Data for PHASE number: 1 ==> Current R\_Bragg for Pattern# 1: 7.63  
 -----

Fe7Pd3

! Nat Dis Ang Pr1 Pr2 Pr3 Jbt Irf Isy Str Furth ATZ Nvk Npr More  
 2 0 0 0.0 0.0 1.0 0 0 0 0 0 242.000 0 5 0

F m -3 m <--Space group symbol  
 ! Atom Typ X Y Z Biso Occ In Fin N\_t Spc /Codes  
 FE FE 0.00000 0.00000 0.00000 0.00000 0.70000 0 0 0 0  
 PD PD 0.50000 0.50000 0.00000 0.00000 0.30000 0 0 0 0  
 0.00 0.00 0.00 0.00 0.00

!-----> Profile Parameters for Pattern # 1  
 ! Scale Shape1 Bov Str1 Str2 Str3 Strain-Model  
 0.49161E-05 0.00986 0.95010 0.00000 0.00000 0.00000 0  
 21.00000 0.000 0.000 0.000 0.000 0.000  
 ! U V W X Y Gausiz Lorsiz  
 Size-Model  
 -0.291930 0.346379 0.101777 0.028172 0.000000 0.000000 0.000000  
 0 91.000 101.000 0.000 0.000 0.000 0.000 0.000  
 ! a b c alpha beta gamma  
 3.762833 3.762833 3.762833 90.000000 90.000000 90.000000  
 31.00000 31.00000 31.00000 0.00000 0.00000 0.00000  
 ! Pref1 Pref2 Asy1 Asy2 Asy3 Asy4  
 -0.44663 0.00000 -0.35365 -0.00839 0.00000 0.00000  
 131.00 0.00 141.00 151.00 0.00 0.00

-----  
 ! Data for PHASE number: 2 ==> Current R\_Bragg for Pattern# 1: 2.30  
 -----

Cu

```

!Nat Dis Ang Pr1 Pr2 Pr3 Jbt Irf Isy Str Furth      ATZ   Nvk Npr More
  1  0  0  0.0 0.0 1.0  0  0  0  0  0      242.000  0  5  0
!
F m -3 m
!Atom Typ      X      Y      Z      Biso      Occ      In Fin N_t Spc /Codes
CU  CU      0.00000  0.00000  0.00000  0.00000  1.00000  0  0  0  0
      0.00      0.00      0.00      0.00      0.00
!-----> Profile Parameters for Pattern # 1
!  Scale      Shape1      Bov      Str1      Str2      Str3      Strain-Model
0.23582E-04  0.27124  4.71804  0.00000  0.00000  0.00000  0
111.00000  201.000  191.000  0.000  0.000  0.000
!      U      V      W      X      Y      GausSiz  Lorsiz
Size-Model
-0.291930  0.346379  0.101498  0.000000  0.000000  0.000000  0.000000
0
  91.000  101.000  170.001  0.000  0.000  0.000  0.000
!  a      b      c      alpha      beta      gamma
3.617138  3.617138  3.617138  90.000000  90.000000  90.000000
121.00000  121.00000  121.00000  0.00000  0.00000  0.00000
!  Pref1      Pref2      Asy1      Asy2      Asy3      Asy4
0.03985  0.00000  -0.32881  -0.00793  0.00000  0.00000
161.00  0.00  171.00  181.00  0.00  0.00

```

fe7pd3282k.pcr

COMM Fe7Pd3 heat treated treated 5d@1100C -- 282 K  
 ! Current global chi2 (Bragg contrib.) = 8.445  
 ! Files => DAT-file: tra, PCR-file: tra\_keep1  
 ! Job Npr Nph Nba Nex Nsc Nor Dum Iwg Ilo Ias Res Ste Nre Cry Uni Cor Opt Aut  
 0 5 3 0 2 0 0 0 0 0 0 0 0 0 0 0 0 0 0 0

! Ipr Ppl Ioc Mat Pcr Ls1 Ls2 Ls3 NLI Prf Ins Rpa Sym Hkl Fou Sho Ana  
 0 0 1 0 1 0 0 0 0 1 0 0 0 1 2 0 0

! lambda1 Lambda2 Ratio Bkpos wdt Cthm muR AsyLim Rpolarz  
 -> Patt# 1  
 1.540562 1.540562 1.0000 40.000 5.0000 0.0000 0.0000 45.00 0.0000

! NCY Eps R\_at R\_an R\_pr R\_gl Thmin Step Thmax PSD  
 Sent0  
 8 0.01 0.80 0.80 0.80 0.80 40.0000 0.005000 80.0000 0.000  
 0.000

! Excluded regions (LowT HighT) for Pattern# 1  
 -10.00 15.00  
 73.50 180.00

24 !Number of refined parameters

! Zero Code SyCos Code SySin Code Lambda Code MORE -> Patt# 1  
 1.50212 11.00 0.00000 0.00 0.00000 0.00 0.000000 0.00 0  
 ! Background coefficients/codes for Pattern# 1  
 455.98 -83.440 -2107.6 5382.4 -3437.1 0.0000  
 0.000 0.000 0.000 0.000 0.000 0.000 0.000

-----  
 ! Data for PHASE number: 1 ==> Current R\_Bragg for Pattern# 1: 9.89  
 -----

Fe7Pd3

! Nat Dis Ang Pr1 Pr2 Pr3 Jbt Irf Isy Str Furth ATZ Nvk Npr More  
 2 0 0 0.0 0.0 1.0 0 0 0 0 0 242.000 0 5 0

F m -3 m <--Space group symbol  
 ! Atom Typ X Y Z Biso Occ In Fin N\_t Spc /Codes  
 FE FE 0.00000 0.00000 0.00000 0.00000 0.70000 0 0 0 0  
 0.00 0.00 0.00 0.00 0.00  
 PD PD 0.00000 0.00000 0.00000 0.00000 0.30000 0 0 0 0  
 0.00 0.00 0.00 0.00 0.00

!-----> Profile Parameters for Pattern # 1  
 ! Scale Shape1 Bov Str1 Str2 Str3 Strain-Model  
 0.83363E-06 0.88103 4.35206 0.00000 0.00000 0.00000 0  
 41.00000 161.000 141.000 0.000 0.000 0.000  
 ! U V W X Y GausSiz Lorsiz  
 Size-Model  
 -0.494593 0.427209 0.101777 0.003801 0.000000 0.000000 0.000000  
 0 111.000 121.000 0.000 0.000 0.000 0.000 0.000  
 ! a b c alpha beta gamma  
 3.812465 3.812465 3.812465 90.000000 90.000000 90.000000  
 51.00000 51.00000 51.00000 0.00000 0.00000 0.00000  
 ! Pref1 Pref2 Asy1 Asy2 Asy3 Asy4  
 0.48425 0.00000 0.34862 0.01464 0.00000 0.00000  
 221.00 0.00 231.00 0.00 0.00 0.00

-----  
 ! Data for PHASE number: 2 ==> Current R\_Bragg for Pattern# 1: 5.18  
 -----

Fe7Pd3

```

!Nat Dis Ang Pr1 Pr2 Pr3 Jbt Irf Isy Str Furth      ATZ      Nvk Npr More
  2  0  0 0.0 0.0 1.0  0  0  0  0  0      242.000  0  5  0
!
F 4/m m m      <--Space group symbol
!Atom Typ      X      Y      Z      Biso      Occ      In Fin N_t Spc /Codes
FE  FE      0.00000  0.00000  0.00000  0.00000  0.70000  0  0  0  0
      0.00      0.00      0.00      0.00      0.00
PD  PD      0.00000  0.00000  0.00000  0.00000  0.30000  0  0  0  0
      0.00      0.00      0.00      0.00      0.00
!-----> Profile Parameters for Pattern # 1
!  Scale      Shape1      Bov      Str1      Str2      Str3      Strain-Model
0.92267E-06  -4.90848  9.42637  0.00000  0.00000  0.00000  0
      21.00000  81.000  71.000  0.000  0.000  0.000
!      U      V      W      X      Y      GauSiz  Lorsiz
Size-Model
-0.494593  0.427209  0.101777  0.106778  0.000000  -0.091777  0.000000
0
      111.000  121.000  0.000  241.000  0.000  171.000  0.000
!      a      b      c      alpha      beta      gamma
      3.852890  3.852890  3.850000  90.000000  90.000000  90.000000
      0.000000  0.000000  0.000000  0.000000  0.000000  0.000000
!  Pref1      Pref2      Asy1      Asy2      Asy3      Asy4
1.55691  0.00000  -1.77717  -0.60860  0.00000  0.00000
      101.00  0.00  91.00  181.00  0.00  0.00
!-----
!  Data for PHASE number: 3 ==> Current R_Bragg for Pattern# 1: 1.39
!-----

```

Cu

!

```

!Nat Dis Ang Pr1 Pr2 Pr3 Jbt Irf Isy Str Furth      ATZ      Nvk Npr More
  1  0  0 0.0 0.0 1.0  0  0  0  0  0      242.000  0  5  0
!
F m -3 m      <--Space group symbol
!Atom Typ      X      Y      Z      Biso      Occ      In Fin N_t Spc /Codes
CU  CU      0.00000  0.00000  0.00000  0.00000  1.00000  0  0  0  0
      0.00      0.00      0.00      0.00      0.00
!-----> Profile Parameters for Pattern # 1
!  Scale      Shape1      Bov      Str1      Str2      Str3      Strain-Model
0.38612E-05  0.11691  -1.94414  0.00000  0.00000  0.00000  0
      31.00000  151.000  131.000  0.000  0.000  0.000
!      U      V      W      X      Y      GauSiz  Lorsiz
Size-Model
-0.494593  0.427209  0.101777  0.003801  0.000000  0.000000  0.000000
0
      111.000  121.000  0.000  0.000  0.000  0.000  0.000
!      a      b      c      alpha      beta      gamma
      3.679979  3.679979  3.679979  90.000000  90.000000  90.000000
      61.00000  61.00000  61.00000  0.00000  0.00000  0.00000
!  Pref1      Pref2      Asy1      Asy2      Asy3      Asy4
-0.02877  0.00000  0.38982  0.05617  0.00000  0.00000
      191.00  0.00  201.00  211.00  0.00  0.00

```

fe7pd3260K.pcr

COMM Fe7Pd3 heat treated 5d@1100C -- 260 K

! Current global Chi2 (Bragg contrib.) = 2.279

! Files => DAT-file: low, PCR-file: low

! Job Npr Nph Nba Nex Nsc Nor Dum Iwg Ilo Ias Res Ste Nre Cry Uni Cor Opt Aut  
 0 5 2 0 2 0 0 0 0 0 0 0 0 0 0 0 0 0 0 0

! Ipr Ppl Ioc Mat Pcr Ls1 Ls2 Ls3 NLI Prf Ins Rpa Sym Hkl Fou Sho Ana  
 0 0 1 0 1 0 0 0 0 1 0 0 0 0 1 2 0 0

! lambda1 Lambda2 Ratio Bkpos wdt Cthm muR AsyLim Rpolarz  
 ->Patt# 1  
 1.540562 1.540562 1.0000 40.000 30.0000 0.0000 0.5000 45.00 0.0000

! NCY Eps R\_at R\_an R\_pr R\_gl Thmin Step Thmax PSD  
 Sent0  
 7 0.01 0.80 0.80 0.80 0.80 40.0000 0.005000 75.0000 0.000  
 0.000

! Excluded regions (LowT HighT) for Pattern# 1  
 -10.00 25.00  
 80.00 180.00

20 !Number of refined parameters

! Zero Code SyCos Code Sysin Code Lambda Code MORE ->Patt# 1  
 0.72821 11.00 0.00000 0.00 0.00000 0.00 0.000000 0.00 0  
 ! Background coefficients/codes for Pattern# 1  
 455.54 -737.53 1534.4 -1209.9 444.57 0.0000  
 141.000 151.000 161.000 171.000 181.000 0.000

-----  
 ! Data for PHASE number: 1 ==> Current R\_Bragg for Pattern# 1: 5.30  
 -----

Fe7Pd3

! Nat Dis Ang Pr1 Pr2 Pr3 Jbt Irf Isy Str Furth ATZ Nvk Npr More  
 2 0 0 0.0 0.0 1.0 0 0 0 0 0 242.000 0 5 0

F 4/m m m <--Space group symbol  
 ! Atom Typ X Y Z Basis Occ In Fin N\_t Spc /Codes  
 FE FE 0.00000 0.00000 0.00000 0.00000 0.70000 0 0 0 0  
 PD PD 0.00000 0.00000 0.00000 0.00000 0.30000 0 0 0 0  
 0.00 0.00 0.00 0.00 0.00

!-----> Profile Parameters for Pattern # 1  
 ! Scale Shape1 Bov Str1 Str2 Str3 Strain-Model  
 0.30855E-04 0.00986 0.95010 0.00000 0.00000 0.00000 0  
 21.00000 0.000 0.000 0.000 0.000 0.000  
 ! U V W X Y Gausiz Lorsiz  
 Size-Model  
 -0.368119 0.298221 0.101777 0.028172 0.000000 0.000000 0.000000  
 0 71.000 81.000 0.000 0.000 0.000 0.000 0.000  
 ! a b c alpha beta gamma  
 3.780860 3.780860 3.752991 90.000000 90.000000 90.000000  
 31.00000 31.00000 41.00000 0.00000 0.00000 0.00000  
 ! Pref1 Pref2 Asy1 Asy2 Asy3 Asy4  
 -0.44663 0.00000 -0.35365 -0.00839 0.00000 0.00000  
 0.00 0.00 0.00 0.00 0.00 0.00

-----  
 ! Data for PHASE number: 2 ==> Current R\_Bragg for Pattern# 1: 0.48  
 -----

Cu

```

!Nat Dis Ang Pr1 Pr2 Pr3 Jbt Irf Isy Str Furth      ATZ   Nvk Npr More
  1  0  0  0.0 0.0 1.0  0  0  0  0  0      242.000  0  5  0
!
F m -3 m
!Atom Typ      X      Y      Z      Biso      Occ      In Fin N_t Spc /Codes
CU  CU      0.00000  0.00000  0.00000  0.00000  1.00000  0  0  0  0
      0.00      0.00      0.00      0.00      0.00
!-----> Profile Parameters for Pattern # 1
!  Scale      Shape1      Bov      Str1      Str2      Str3      Strain-Model
  0.21544E-04  0.31495  5.35314  0.00000  0.00000  0.00000  0
      51.00000  101.000  91.000  0.000  0.000  0.000
!      U      V      W      X      Y      GausSiz  Lorsiz
Size-Model
-0.368119  0.298221  0.101498  0.000000  0.000000  0.000000  0.000000
0
  71.000  81.000  0.000  191.000  0.000  201.000
0.000
!      a      b      c      alpha      beta      gamma
  3.617871  3.617871  3.617871  90.000000  90.000000  90.000000
  61.00000  61.00000  61.00000  0.00000  0.00000  0.00000
! Pref1 Pref2 Asy1 Asy2 Asy3 Asy4
  0.10452  0.00000 -0.14759  0.02155  0.00000  0.00000
  111.00  0.00  121.00  131.00  0.00  0.00

```

